Dissertation submitted to the
Combined Faculties for the Natural Sciences and for Mathematics
of the Ruperto-Carola University of Heidelberg, Germany
for the degree of
Doctor of Natural Sciences

presented by

Diplom-Physiker Volker Schulz
born in: Blieskastel
Oral examination: 9. July 2003

Description and reconstruction of microscopic random heterogenous media in order to estimate macroscopic hydraulic functions

Referees: Prof. Dr. Kurt Roth
Prof. Dr. Fred Hamprecht

Zusammenfassung

Die vorliegende Arbeit beschäftigt sich mit Ein- und Mehrphasenströmungen in porösen Medien. Im Rahmen eines upscaling Konzeptes wurden Simulationen auf einer Mikroskala mit Messungen auf einer größeren, einer sogenannten Kontinuumsskala verglichen. Das untersuchte Medium war ein gesintertes Borsilikatglass, dessen Porengeometrie mittels Röntgentomografie bestimmt wurde. Für diese Geometrie wurde mit Hilfe eines lattice-Boltzmann Verfahrens die Navier-Stokes Gleichung gelöst und die hydraulische Leitfähigkeit berechnet. Zusätzlich wurde ein morphologisches Modell verwendet, um die Druck-Sättigungsbeziehung zu erhalten. Die beiden hydraulischen Parameter wurden dann mit Messungen verglichen. Die Übereinstimmung zwischen Simulation und Experiment war nicht in allen Punkten zufriedenstellend und die Abweichungen wurden sorgfältig diskutiert. Möglicherweise wurden Oberflächeneigenschaften des Materials zu Unrecht vernachlässigt.

Für die weitere Arbeit war es nötig, die Porengeometrie zu rekonstruieren. Daher wurden verschiedene Rekonstruktionsalgorithmen implementiert und verschiedene Strukturen auf der Basis eines Boolschen Modells erzeugt. Zusätzlich konnten ähnliche Strukturen mit Hilfe eines simulated-annealing-Algorithmus generiert werden wobei die Minkowki Funktionale und die Porenlängenverteilung (interception length) als Zielfunktion verwendet wurden. Die Ähnlichkeit bezieht sich hierbei auf vergleichbare hydraulische Eigenschaften.

Abstract

This thesis is a contribution to studies in the field of single and two phase flow processes in porous media. It is to be regarded in the context of an upscaling of physical properties: the simulations were performed on a microscopic scale and were compared to measurements on a larger, a so-called continuum scale. The investigated material was a sintered boron silicate glass. Based on the measured pore geometry (with x-ray tomography), a lattice-Boltzmann Navier-Stokes equation solver was used to calculate the velocity field and the hydraulic conductivity. Additionally, the pressure-saturation relation of a primary drainage process was derived from a pore-morphology-based model. For both hydraulic properties, a REV could be defined and the effective values were compared to measured results. The agreement between the simulation and the measurement is not entirely satisfying and the deviations were thoroughly discussed. Surface properties which were not taken into account could be regarded as a major source of error.

Further studies required the reconstruction of the measured pore geometry. Different reconstruction algorithms were therefore applied. Similar structures were generated by using a Boolean model and a simulated annealing algorithm using both the Minkowski functionals and the interception length density distribution. The similarity refers to comparable simulated hydraulic properties.

Contents

1 Introduction 1
1.1 Objectives of this study 2
1.2 Outline 3

2 Integral geometry 5
2.1 Minkowski functionals 5
2.1.1 Definition of MF 5
2.1.2 MF and physical parameters 6
2.2 Measuring the MF of voxelized images 7
2.2.1 The Crofton formula 7
2.2.2 Definition of a binary image 7
2.2.3 Marching cube method 8
2.2.4 Determination of the MF from the N-cube configurations 9
2.3 MF for simple geometric object and discretization errors 13
2.3.1 MF of digital spheres 14
2.3.2 MF of digital cubes and rotations on a cubic lattice 14
2.4 Minkowski functions 16
2.4.1 Parallel bodies 16
2.4.2 Interpretation of Mfs for complicated structures 16

3 Morphological image analysis 19
3.1 Morphological operators 19
3.1.1 Erosion 19
3.1.2 Dilation 20
3.1.3 Opening and closing 20
3.2 Granulometry 21
3.2.1 Speeding up the erosion with spheres 24
3.2.2 Interception length density function 26

4 Model for the determination of capillary pressure-saturation curves 27
4.1 Pore-morphology-based simulation (PMB) 27
4.1.1 Background 27

4.1.2 Simulation steps . . . 28
4.1.3 PMB model and non-spherical interfaces . . . 29
4.1.4 Limitations of the PMB model at small saturations . . . 30
4.2 PMB model with modified spheres as SE . . . 30

5 Lattice Boltzmann model 33
5.1 The lattice-Boltzmann model . . . 33
5.1.1 The Boltzmann equation . . . 33
5.1.2 BGK collision operator . . . 34
5.1.3 Discretization of the Boltzmann equation . . . 34
5.1.4 Chapman-Enskog expansion . . . 34
5.1.5 Underlying lattice and equilibrium distribution functions . . . 36
5.1.6 Parameters of the Q19D3 lattice . . . 37
5.2 Fluid-solid interactions . . . 38
5.2.1 Pressure boundary conditions and volume forces . . . 38
5.3 Simulations of flow in a circular pipe . . . 39
5.3.1 Conversion between lattice and physical units . . . 40
5.4 Permeability and hydraulic conductivity . . . 41
5.4.1 Hydraulic conductivity of a circular pipe . . . 42
5.5 Hydraulic conductivity with different BC . . . 42

6 Analysis of the investigated structures 45
6.1 Investigated material . . . 45
6.2 Micro tomography and 3D representation of the pore space . . . 46
6.2.1 Segmentation of the tomographic image . . . 46
6.3 Pore size distributions . . . 48
6.3.1 P250 . . . 48
6.3.2 P100 . . . 48
6.4 Influence of the image resolution on the pore size distribution . . . 50
6.5 Physical parameters at the microscopic and the macroscopic scale . . . 52
6.5.1 Characteristic function . . . 52
6.5.2 Averaging . . . 52
6.5.3 Definition of effective properties and the representative elementary volume . . . 53
6.5.4 Materials with discrete hierarchy . . . 53
6.6 REV with respect to hydraulic conductivity . . . 55
6.7 Simulated hydraulic conductivity compared to measurements . . . 56
6.7.1 Falling head method . . . 56
6.7.2 Simulated and measured hydraulic conductivity of P250 . . . 57
6.7.3 Simulated and measured hydraulic conductivity of P100 . . . 59
6.7.4 Comparison to related studies . . . 59

6.8 Pressure saturation relations 61
6.8.1 REV with respect to the pressure saturation curve 61
6.8.2 Differences at low saturations for both media 62
6.8.3 Simulated and measured pressure-saturation relations 65
6.8.4 Measurement of the P^c-S^w curve 66
6.8.5 Discussion of the simulated and the measured P^c-S^w curves . 67

7 Concept for the reconstruction of porous media 71
7.1 REV and geometry information 71
7.2 Characterization of the geometry of a structure 71
7.2.1 Two-point correlation functions 72
7.2.2 Minkowski functionals 73
7.2.3 Variations of the integral mean curvature 75
7.2.4 Residual water content 75
7.3 Conclusion 75

8 Reconstruction of the porous media 77
8.1 Reconstruction based on Minkowski functionals 77
8.1.1 Dimensionality of the MF compared to a binary structure . . 77
8.1.2 Reconstruction results 78
8.2 Boolean model of spheres 80
8.2.1 Reconstruction of P100 with a Boolean model 80
8.2.2 Hydraulic conductivity of the Boolean reconstruction 81
8.2.3 P^c-S^w curve of the Boolean reconstruction 82
8.2.4 Extensions of the Boolean model 84
8.3 Reconstruction on the basis of the Minkowski functions 85
8.3.1 Simulated annealing 85
8.3.2 Objective function 85
8.3.3 Simulation results 86
8.4 MF and interception length 88
8.4.1 Simulation results 89

9 Summary and outlook 91
9.1 Structure analysis and hydraulic functions 91
9.2 Reconstruction algorithms 92
9.3 Outlook 93

References 94

List of Figures

1.1 Hierarchy of scales in a soil. At the meter scale (A), two different horizons can be distinguished. The centimeter scale (B) shows aggregates with different densities and finally at the scale of micrometers (C) the structure can be described by a binary geometry of void and solid phase. Modified after Roth et al. (1999). 2

2.1 (a) Binary structure in 3D represented on a isotropic cubic lattice. The different phases are assigned with full disks (binary value 0) and empty disks (binary value 1), respectively. (b) Unit cell of the lattice where each position within the cube is labeled with a binary word to indicate the different neighborhood configurations (N-cube). 8

2.2 Definition of the curvature of a surface element as the section boundary with a plane. 10

2.3 Illustration of the 13 planes in a unit cell of a cubic lattice. All 13 planes have different normal vectors. 11

2.4 On a cubic lattice in 2D either the black or the white phase can be interpreted as connected to the diagonal neighbor. Therefore, one has to define one phase as 8 connected (8 neighbor nodes) and the other will be automatically 4 connected (Arns 2002). 13

2.5 Measured values of the MF for voxelized spheres (left) and cubes (right) on a cubic lattice. The values are normalized to the theoretic values. 14

2.6 The measurement of the circumference depends on the definition of rotations on the lattice. Shown is a single pixel together with 4 (a) and 2 (b) test lines. In case (a) we measure the length of a polygon, in case (b) the length of a square. For further explanations see text. 15

2.7 Two simple geometric objects (black areas) in two dimensions and their parallel bodies (gray and black area.). 16

2.8 Two parallel bodies for a complicated structure (black phase treated as the object). The calculation was done in 3D while only cross sections are plotted. 17

2.9 Minkowski functions for the structure shown in figure 2.8. ϵ given in lattice units. 18

3.1 Erosion $\mathcal{E}$ of a set X by a disk B. The small element vanishes by the erosion since B never fits it (modified after Soille (1999)). 19
3.2 Dilation $\mathcal{D}$ of a set X by a disk B. In that example the two objects melt together by the dilation. 20
3.3 Representation of disks on a cubic lattice (digital disks) with increasing diameter. 22
3.4 Results of morphological opening with squares (upper row) and discrete disks as SE. At each opening step, the diameter of the disk and the vertex length of the square are identical. The original image is a distribution of digital disks with different diameters. 23
3.5 The size distribution of the disks from figure 3.4 determined by a granulometry with disks and with squares. The figure on the left hand side is the cumulative fraction of the objects and its derivative on the right hand side. 23
3.6 Modified digital spheres which are the result of alternating dilation of a single voxel with a cross and a cube (3×3×3 voxel). 24
3.7 Cumulative pore fraction as a result of morphological openings with digital spheres and modified spheres as explained in the text. 25
3.8 Illustration of the interception length between the structure elements (gray) and an infinite long line. Modified after Torquato (2002). . . 26

4.1 Capillary pressure-saturation curve of a single elliptic capillary tube as determined by the PMB model. The pressure is normalized to a theoretical value which was set to be 1. The deviations between the digital spheres and the modified spheres are explained in section 4.2. 29
4.2 Differences between the pressure-saturation curve from the PMB model working either with digital spheres or modified digital spheres. Details about the simulated pressure-saturation relations will be described in chapter 6. 31

5.1 Lattice velocity vectors for the Q19D3 model. 36
5.2 Illustration of fluid and solid nodes together with the imaginary boundary in the middle. 38
5.3 Velocity field for the simulated flow in a circular pipe with a diameter of 11 lattice nodes. The figure on the left hand side shows the relative deviation of the simulated velocity from the theoretic value (v_o) for a cross section. 40

5.4 Hydraulic conductivity k of a circular pipe versus the pipe diameter. The values are normalized to the theoretic values given in equation 5.33. The dashed line shows the deviation of the cross section area from the theoretic value of $\pi(d/2)^2$ (discretization effect – compare figure 2.5). 42
5.5 LB simulated velocity fields of flow in a complicated geometry. Shown are the absolute values of the velocity field for two cross section in flow direction. The red color indicates a velocity of zero with higher values toward blue. In figure (a), the flow is driven by pressure gradient and the velocities at the inlet and at the outlet are zero. In figure (b), the flow was driven by a volume force. 43

6.1 Application of a median filter and the following segmentation. Shown is a 2D slice (175×175 pixel) for the scan of P100. 47
6.2 3D visualization of the reconstructed pore geometry. On the left hand side P250 and on the right hand side P100. Both images show volumes of 120^3 voxel. Thus, the sample on the left hand side represents a volume of about $47\,\mathrm{mm}^3$ and the other a volume of about $23\,\mathrm{mm}^3$. . 47
6.3 Pore size distribution of P250 as determined by morphological opening with digital spheres as SE. The plot on the left hand side is the cumulative pore spectrum. On right hand side, the pore fraction is plotted together with the interception length distribution (dashed line). The arrows indicate the values given by the manufacturer (see table 6.1). 49
6.4 Pore size distribution of the medium P100. For details see caption of figure 6.3. 49
6.5 Simple grid refinement by a factor 2. The object on the left hand side has the shape of a digital disk with a diameter of 5 lattice nodes. The maximum digital disk (with odd diameter) that fits the same object on the finer lattice (right hand side) has a diameter of only 7 lattice nodes (gray area). The disk with a diameter of 9 lattice nodes (light gray) is too big 50
6.6 Cross section through the pore geometry of the medium P100. The image on the right hand side is a refinement due to a Shepard interpolation. 51
6.7 Cumulative pore fraction of the original image (bold line) and the refined image. The figure shows that we get only minor differences between the morphological operations with digital spheres and modified spheres. The computation with modified spheres however is much faster as explained in chapter 3. 51
6.8 Illustration of a medium with discrete hierarchy. 54

6.9 The hydraulic conductivity K versus the image size for the medium P250. The error bars are due to the range of K in the three different flow directions. 55

6.10 Hydraulic conductivity k versus the image size for the medium P100. The error bars are due to the range of k over the three different flow directions. 56

6.11 Overview for the falling head permeameter. The height of the water level can be measured by a pressure sensor above the sample. 57

6.12 Model for the porosity distribution of the column sample of medium P250. 58

6.13 2D slices of the binary image with different thresholds for the segmentation. This leads to porosities between 0.30 and 0.48. 58

6.14 Measured and simulated hydraulic conductivities of the two investigated media. 59

6.15 Simulated drainage of P100. Shown are only iso surfaces of the air distribution. The water drains through the plane on the bottom while the air enters the sample through the upper plane. All other sides can be seen as closed. 62

6.16 Pressure-saturation curves of the sample P250 with different image sizes as determined by the PMB model. The determined saturation are a mean values over the 6 simulated directions. 63

6.17 Pressure-saturation curves of the sample P100 with different image sizes as determined by the PMB model. The determined saturation are a mean values over the 6 simulated directions. The subplot shows in detail the decline of the boundary effects - details see text. . . . 63

6.18 Pressure-saturation curve of P250 as determined by the PMB model with different porosities compared to a model of a capillary bundle and measured data. 65

6.19 Pressure-saturation curve of P100 as determined by the PMB model compared to a model of a capillary bundle and measured data. . . . 66

7.1 Sketch of hierarchically ordered REVs in a complicated structure. The REV for physical properties like the dispersivity may require image sizes larger than measurable. This is illustrated by the dashed box. 72

7.2 Two-point correlation function for different image sizes of medium P100. 73

7.3 Minkowski functionals for medium P250 with increasing image size. The MF were normalized since we are only interested in their variations versus the sampled volume. 74

7.4 Minkowski functionals for medium P100 with increasing image size. As in figure 7.3, the values are normalized. Here, the integral mean curvature shows a significantly larger variation and is therefore plotted on the right hand axis. 74

8.1 Four different structures in 2D (300^3 pixel) which have exactly the same Minkowski functionals. Periodic boundaries where used for the calculation of the MF. 78
8.2 Two realizations of a Boolean model with spheres of constant radius. With increasing point density, the spheres will more and more overlap. 80
8.3 Mean MF for realizations of the Boolean model. The image size was 80^3 voxel and the lattice spacing 0.015 mm (isotropic). 81
8.4 Cumulative grain size distribution of P100 as determined by the morphological granulometry. 82
8.5 3D visualizations of the original pore geometry (P100, on the left) and the reconstruction with a Boolean model. Beside the structure, the figure shows the absolute value of the velocity field in two cross sections. 83
8.6 Pressure-saturation curve for the medium P100 (120^3 voxel) and its Boolean reconstruction. 83
8.7 On an entirely "black" image, a single voxel is switched into "white" phase. This has an impact on the the eroded images (b) and (c). Image (b) and (c) are erosions of the black phase with a squares of 3 and 5 lattice nodes edge length. 86
8.8 Original image and reconstruction based on the Mfs (porosity, boundary length, and Euler number over 2 erosion/dilation steps with squares). The images have a size of 40^2 pixel and a resolution of 1/40=0.025 mm. Therefore, the boundary l is given in 1/mm and the Euler number as $1/\text{mm}^2$. 87
8.9 Illustration of the impact of a single pixel flip to the interception length in 2D. Since we are only interested in the interception length of lines parallel to the main axis, the swapped pixel in the middle of the image (in gray), changes the interception length from 5 pixel to two times 2 pixel in the horizontal line. This can be calculated in a very efficient way. 88
8.10 Original image (P100, a) and one example of its reconstruction (b) where both images have the same MF and approximately the same ILDF. The image size is 150^3 voxel with a resolution of 7.5 μm. . . . 89
8.11 ILDF for the original image and one example of its reconstruction. . 89
8.12 Pressure-saturation relations of the original image and one example of its reconstruction. 90

List of Tables

2.1 Geometric parameters and the according MF in two and three dimensions. 6

2.2 MF of spheres and cubes. 13

5.1 Conversion from lattice units to the SI system. Normally, the lattice spacing together with the density, and the viscosity of the fluid are fixed and the other parameters are converted as indicated. 40

6.1 Notation and pore size of the investigated borosilicate glass. The porosity was measured gravimetrically and the error is mainly caused by the volume measurement. 46

6.2 Van Genuchten parameters of the two investigated samples according to MSO experiments. 67

8.1 MF and hydraulic conductivity of the original image (P100) and the Boolean reconstruction. The interval gives the maximum and minimum values that have been found from 16 different realizations. . . . 81

8.2 Hydraulic conductivity of the original image (P100, 80^3 voxel) and the reconstructions. The interval gives the maximum and minimum values from 24 different realizations. 89

List of abbreviations

		section	page
BC	Boundary condition	5.2	38
BGK	Bhatnagar, Grass, and Krook	5.1.2	34
ILDF	Interception length density function	3.2.2	26
LB	Lattice-Boltzmann	5	33
MF	Minkowski functionals	2	5
Mfs	Minkowski functions	2.4	16
MSO	Multi-step outflow	6.8.4	66
NWP	Non-wetting phase	4.1.1	27
PMB	Pore-morphology-based	4	27
REV	Representative elementary volume	6.5.3	53
SE	Structuring element	3.1	19
WP	Wetting phase	4.1.1	27

1 Introduction

Single and multiphase flow processes in porous media have a wide range of applications which range from soil physics through water uptake by napkins to blood flow in arteries. All these processes have in common that they depend on the geometry of the porous medium at a microscopic (or pore) scale[1] while the physical properties of interest are observed at a larger scale which we call continuum scale.

A good example is the flow and transport in soils where the microscale has a typical length of some millimeters or even less (Vogel and Roth 2003), whereas the scale of interest for practical applications is the typical distance between soil surface and groundwater which lies in the range of some meters. At this continuum scale, the physical processes are described by macroscopic material properties, e. g. the hydraulic conductivity or the water retention characteristic.

In this context, simulations at the pore scale have two major objectives. First, they improve the understanding of the physical processes at a microscopic level. Secondly, pore scale models provide a way to determine macroscopic material properties. This can be seen as an upscaling of material properties from a smaller to a larger scale. Upscaling is not trivial and a major challenge in heterogenous porous media. In general, soils show heterogeneity at different scales. In a series of papers, K. Roth and H.-J. Vogel (Roth et al. 1999, Vogel et al. 2002, Vogel and Roth 2003) developed a concept for the upscaling of soil properties in the understanding of soil as a hierarchical heterogenous medium. This concept which is called the scaleway can be explained most easily for a medium of discrete hierarchy but can be applied also to continuous hierarchy or even fractals. The discrete hierarchy, as defined by Cushman (1990), implies that each scale is associated with a representative elementary volume (REV)[2] which defines local material properties. This is illustrated in figure 1.1 where the structure at the smaller scale is not representative for the entire sample volume at the larger scale but only for certain regions.

At the macroscopic scale, where the microscopic details are averaged out, only the macroscopic structure and local material properties are relevant. This is at least true for dissipative processes.

---

[1] Here, the word “microscopic” implies a binary geometry of solid and void phases.

[2] The concept of a REV will be explained in detail in chapter 6.

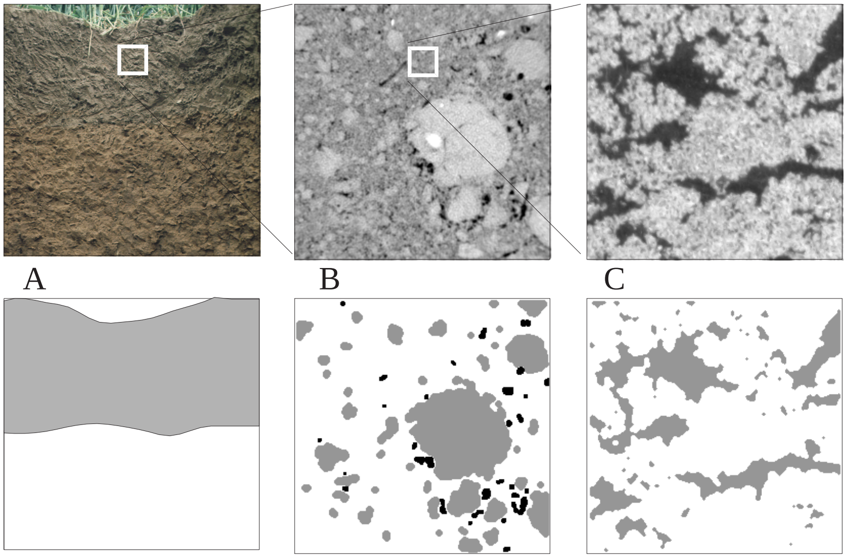

Figure 1.1: *Hierarchy of scales in a soil. At the meter scale (A), two different horizons can be distinguished. The centimeter scale (B) shows aggregates with different densities and finally at the scale of micrometers (C) the structure can be described by a binary geometry of void and solid phase. Modified after Roth et al. (1999).*

1.1 Objectives of this study

In the context of the scaleway this work addresses two problems. The first one is related to the determination of macroscopic or effective hydraulic parameters for the transition from the pore scale to the continuum scale. At the pore scale, the flow can be described by the Navier-Stokes equation and it was an objective of this work to implement a Navier-Stokes equation solver in order to determine the flow field and the associated hydraulic conductivity even for complicated (binary) structures (figure 1.1 C). Also, at the pore scale, we applied a tool for the determination of the capillary pressure-saturation relation. This was done based on the measured pore structure using simplifying assumptions about the multiphase flow processes.

In a second step, we applied methods from image analysis and stereology. Investigations of the 3D pore geometry (e. g. measurements of the Minkowski functionals) were used to deduce useful informations about the macroscopic parameters.

This led us to the second focus of this thesis: the reconstruction of complicated geometries. In practice, the determination of the pore geometry as shown in figure 1.1 (C) leads to 3D representations which are smaller than the size of a REV. This limitation is due to image forming techniques on the one hand and due to a restriction imposed by the material on the other hand. A scan over a larger volume would average over different structure elements (at the larger scale) and contradict

the concept of the scaleway.
Therefore, we reconstructed the measured structures with reconstruction algorithms based on geometric parameters. The requirement for these parameters in the context of the scaleway is that they are robust even for small sample sizes.

1.2 Outline

This thesis is structured as follows. The chapters 2 – 5 give an overview of the theoretical background of the methods used in this work.
First, we outline some background of integral geometry with the focus on the Minkowski functionals. These functionals which have a wide range of applications in statistical physics will be used in the further work in order to obtain integrated geometric parameters of the investigated structures.
Then we give an overview about morphological tools from digital image processing. These morphology operators will be used for granulometric investigations but also in a morphological model for the determination of the capillary pressure-saturation relation (chapter 4).
In chapter 5 we explain the lattice-Boltzmann method for solving the Navier-Stokes equation on complicated geometries since we use these flow simulations for the determination of the hydraulic conductivity of a porous medium.
In chapter 6, we apply the developed methods to a porous medium which is a sintered boron silicate glass. On the basis of the pore geometry which has been derived from x-ray tomography, we determined the hydraulic parameters such as the hydraulic conductivity and the pressure-saturation relation. The simulated values are compared to the measured results. In the following discussion of the deviations between model and measurement, we detect the limitations on both sides and give some insight into the importance of physical parameters which are often neglected.
Chapter 7 can be seen as the link between the investigations on measured structures and their reconstruction in chapter 8. With the help of the Minkowski functionals, we determine very useful informations about the investigated samples. One example is the existence of a REV with respect to the hydraulic conductivity. Additionally, we motivate the reconstruction of porous media which is necessary because of the limitations of image forming techniques but also because of the heterogeneity of the material.
Finally, we present the result from different reconstruction algorithms (chapter 8). Our requirements for a "useful" reconstruction method are: the reconstructed image is visually similar to the original and the physical parameters of interest are similar. In this context, we will present negative results for reconstructions which are based on the Minkowski functionals and the Minkowski functions. Better results can be found using a Boolean model and a model using both the Minkowski functionals and the interception length distribution function.

2 Integral geometry

In this chapter we give a short introduction into integral geometry and Minkowski functionals (MF).
After the definition of the MF, we present its implementation on pixelized or voxelized[1] images together with a discussion of fast algorithms for its computation. A description of Minkowski functions which are an extension of the MF stands at the end this chapter.

2.1 Minkowski functionals

The motivation behind the application of Minkowski functionals in the framework of this work is as follow. One of the problems that arise in the investigation of disordered material is its complicated spatial structure. Here, Minkowski functionals can be seen as integrated quantities and can be used for the characterization of a structure. The following is only a short introduction to MF where more detailed descriptions can be found in textbooks like Ohser and Mücklich (2000).

2.1.1 Definition of MF

We are dealing with the d-dimensional Euclidean space and the group of transformations G containing as subgroups rotations and translations. Embedded in this space is the the set of convex bodies[2] and, as an extention, the so-called convex ring $\mathcal{C}$ of all finite unions of convex bodies. The idea behind the MF is to characterize an object $X \in \mathcal{C}$ with functionals $\phi(x)$ having the following properties:

a) The functional ϕ is motion invariant or isometric (with respect to Euclidian motion):

$$\phi(gX) = \phi(X), \quad g \in G \tag{2.1}$$

Thus, motion invariance includes both translation and rotation.

---

[1] The term pixel stands for "picture element" of two-dimensional images. The equivalent in 3 dimension is a "volume element", abbreviated as voxel.

[2] We use "body" and "object" as synonyms.

b) The functional ϕ is additive

$$\phi(X_1 \cup X_2) = \phi(X_1) + \phi(X_2) - \phi(X_1 \cap X_2), \quad X_1, X_2 \in \mathcal{C} \tag{2.2}$$

c) ϕ is continuous:

$$\phi(K_i) \to \phi(K), \quad \text{as} \quad K_i \to K \tag{2.3}$$

The convergence for bodies with respect to the Hausdorff metric (Mecke 2000).

There is a number of functionals which fulfill the conditions (a) to (c) but it was shown by Hadwiger (1957) that the functionals build a vector space and a basis for this vector space is given by the Minkowski functionals V_n with $n = 0, \ldots, d+1$. The dimension of the vector space is therefore $d+1$ and we get the remarkable result that all functionals with the characteristics (a) to (c) can be expressed as a linear combination of $d+1$ numbers only.

The MF have a close relation to fundamental geometric characteristics like the volume or the surface of an object as shown in table 2.1 for two and three dimensions. In the literature there are slight differences in the definition of the MF by normalizing to the volume of a d-dimensional unit sphere for example. In the framework of our studies, this normalization is not important and in the following, we will often use the term MF as a synonym for the three (or four, in 3D) basic geometric parameters given in table 2.1.

2D	
Volume	$V_0 = V$
Boundary length L	$V_1 = L/6$
Euler number χ	$V_2 = \chi$
3D	
Volume	$V_0 = V$
Surface area S	$V_1 = S/6$
Integral of mean curvature H	$V_2 = \frac{1}{2 \cdot 3\pi} \int (\frac{1}{R_1} + \frac{1}{R_2}) d\mathcal{S} = H/3\pi$
Euler number χ	$V_3 = \frac{1}{4\pi} \int \frac{1}{R_1 R_2} d\mathcal{S} = \chi$

Table 2.1: Geometric parameters and the according MF in two and three dimensions.

2.1.2 MF and physical parameters

All physical parameters which fullfil the conditions (a) to (c) can be expressed by the MF. This is a direct consequence of the Hadwiger theorem. Examples are all capacitive properties such as the heat capacity. A more complex example is the curvature energy of membranes (Mecke 2000).

2.2 Measuring the MF of voxelized images

2.2.1 The Crofton formula

For voxelized images, there are very efficient algorithms for the calculation of the MF. This is due to its additivity and the so-called Crofton formula

$$V_\nu(A) = \int_G dE^\nu \chi(A \cap E^\nu) \tag{2.4}$$

where E^ν is a ν-plane. Therefore, in three dimensions E^ν is either a point, a line, a plane, or the whole space. The integral over G is defined over all rigid motions on the underlying vector space (in our case the Euclidian vector space). χ is an index function which counts

$$\chi(K) = \begin{cases} 0 & \text{if} \quad K = \emptyset \\ 1 & \text{if} \quad K \quad \text{convex} \end{cases} \tag{2.5}$$

The simple interpretation of the Crofton formula is, that e. g. for the calculation of the surface, we only have to count how often a line intersects with the object A while the line fulfills all possible translations and rotations.

In the given form, equation 2.4 applies only to convex bodies but can easily be extended to sets of convex bodies which are unifications of convex bodies. A more complete description of the Crofton formula and other central topics of integral geometry can be found in textbooks. For a compact overview from a mathematical point of view we refer to Hug and Schneider (2002).

2.2.2 Definition of a binary image

Before we show the application of equation 2.4 on voxelized images, we have to state that these images are a subset of the three-dimensional Euclidean space. Additionally, we use only cubic lattices which are the most common discretization of 3D spatial microstructures. Therefore, we define the image by a matrix $B = (b_{xyz})$, where

$$b_{xyz} := \begin{cases} 0 & : \text{voxel at } x, y, z \text{ belongs to phase } \Xi \\ 1 & : \text{voxel at } x, y, z \text{ belongs to the complement } \Xi^c \end{cases} \tag{2.6}$$

as illustrated in figure 2.1 (a). The possible values for x, y, and z are given by the image size X, Y, and Z which are the total numbers of voxel in each direction:

$$x = 0, 1, 2, \ldots, X \qquad y = 0, 1, 2, \ldots, Y \qquad z = 0, 1, 2, \ldots, Z \tag{2.7}$$

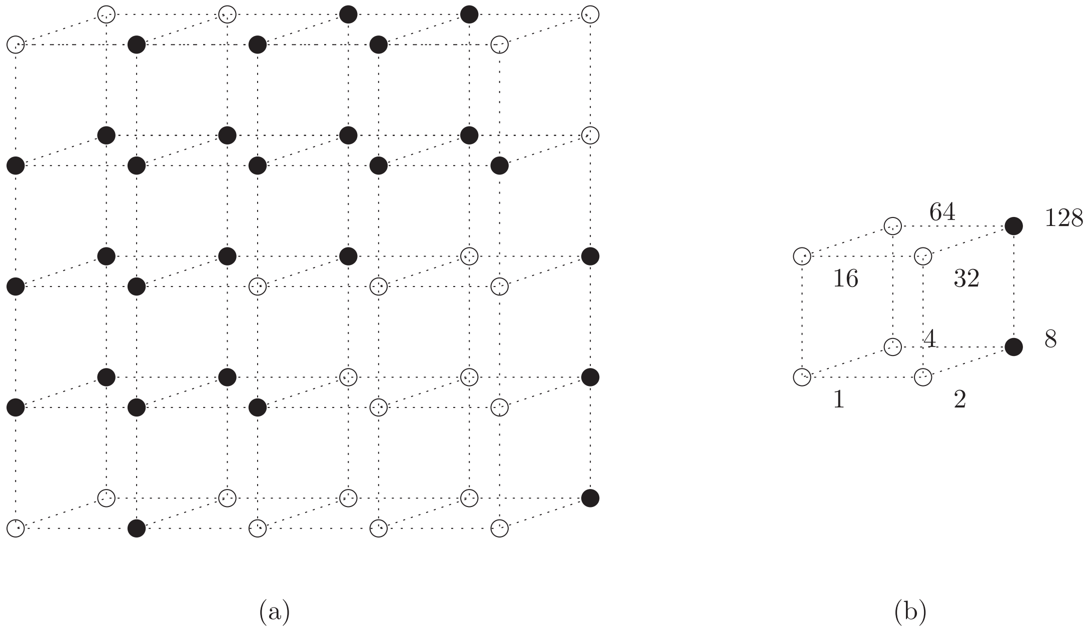

(a) (b)

Figure 2.1: (a) Binary structure in 3D represented on a isotropic cubic lattice. The different phases are assigned with full disks (binary value 0) and empty disks (binary value 1), respectively. (b) Unit cell of the lattice where each position within the cube is labeled with a binary word to indicate the different neighborhood configurations (N-cube).

2.2.3 Marching cube method

Now, for the determination of the MF we investigate all possible $2 \times 2 \times 2$ voxel configurations (N-cubes) in the image and assign it with a number l:

$$l = \sum_x \sum_y \sum_z \Big(b_{xyz} + 2b_{(x+1)yz} + 4b_{x(y+1)z} + 8b_{(x+1)(y+1)z} + \\ + 16b_{xy(z+1)} + 32b_{(x+1)y(z+1)} + 64b_{x(y+1)(z+1)} + 128b_{x(y+1)(z+1)} \Big) \tag{2.8}$$

In literature, this method is sometimes called “marching cube” since we move a 2^3 “test cube” through the image.

In the example of figure 2.1 (b), the configuration leads to an entry at $h(120)$ since $1 + 2 + 4 + 16 + 32 + 64 = 120$. In three dimensions, the length of the vector h is $2^{16} = 256$ according to the number of different configurations. In 2D it is $2^4 = 16$, analogously.

The frequency of l is stored in a so-called frequency vector $h(l)$. For our purpose, the vector $h(l)$ can be seen as a condensed form of the binary image since it contains all information to calculate the MF (Nagel et al. 2000) as shown in the following.

2.2.4 Determination of the MF from the N-cube configurations

2.2.4.1 Volume density

The zero-order MF which is the volume density[3] V_0 can be calculated by applying equation 2.4 to the $2 \times 2 \times 2$ sub images where E^0 is a point on the lattice. Therefore, we get the simple equation

$$V_0 = \frac{\sum_l [h(l)\theta(l)]}{\sum_l h(l)} \tag{2.9}$$

where

$$\theta(l) = \begin{cases} 1 & : l = \text{odd} \\ 0 & : l = \text{even} \end{cases} \tag{2.10}$$

In other words, equation 2.9 counts all configurations where the bit at position 1 is set.

2.2.4.2 Surface density

For the determination of the volume density, the application of equation 2.4 to voxelized data was obvious. It is more difficult for the calculation of the surface density. In this case E^1 is a line and we count the intersections of all possible test lines in the N-cube. Since we are working on a discrete lattice, there are only $g = 13$ different directions for the test lines given by the vectors

$$\begin{aligned} \mathcal{G} = \{&(1,2),(1,4),(1,16),(1,8),(2,4),(1,32),(2,16),(1,64),(4,16), \\ &(1,128),(2,64),(4,32),(8,16)\} \end{aligned} \tag{2.11}$$

with the notation from figure 2.1 (b).

The transformation from the continuous case to the discrete lattice makes it necessary to introduce a weighting function $\omega(g)$ for the 13 spatial directions of the test lines. Such a weighting is required to mimic the isotropy of the test lines which then leads to

$$6V_1 = S = 2\frac{\sum_l \sum_g [h(l)\theta(l,g)\omega(g)]}{\sum_l \sum_g [h(l)\Delta(g)\omega(g)]} \tag{2.12}$$

where

$$\theta(l,g) = \begin{cases} 1 & : \text{interception with test line in direction } g \\ 0 & : \text{else} \end{cases} \tag{2.13}$$

The values of the weights $\omega(g)$ can be found by a tessellation of the unit sphere into Voronoi cells with respect to the direction of the test lines. The weights are then given by the relative area of the corresponding Voronoi cell (Vogel et al. 2002, Ohser and Mücklich 2000).

---

[3] Instead of directly using the MF as listed in table 2.1 we normalize the values by the volume of the image. The normalization of the MF to image size has only practical reasons. Thereby, it is easier to compare the MF of images which differ in its size and/or resolution.

Equation 2.12 is an expression for the surface *density* (given in [length]$^{-1}$) and contains therefore the term $\Delta(g)$ which is the lattice distance in g-direction in the unit cell. Vogel et al. (2002) use the lattice distance in order to calculate the total length for the normalization. Alternatively, one can use the lattice resolution for the test lines and normalize by the image volume Ohser and Mücklich (2000). In practice, both approaches are equivalent and differ by rounding errors only.

The choice of 13 test lines is due to the fact that we allow rotations of 45^o in all lattice directions. Alternatively, one could limit the rotations to such as 90^o only (Arns 2002). We will discuss that point later when calculating the MF for simple geometric objects.

2.2.4.3 Integral mean curvature

In contrast to the volume and the surface of objects, the definition of its curvature needs a longer explanation. On a (smooth) surface, we are interested on the curvature of a intersection line between the surface and a plane containing the normal vector of the z (figure 2.2). As the plane rotates, we obtain the curvature function $k(\phi) = 1/\rho$. ρ is the radius of a circle which approximates the line segment. The largest and the smallest values for $k(\phi)$, k_1 and k_2 are called the principal curvatures and ρ_1 and ρ_2 the principal radii of curvature, respectively (Weibel 1980). The principal radii of curvature can both either be positive of negative which leads to a distinction between convex, concave, and saddle surfaces. The integral mean

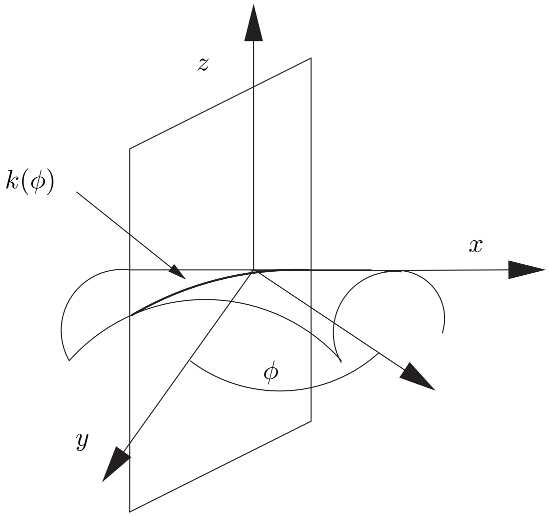

Figure 2.2: Definition of the curvature of a surface element as the section boundary with a plane.

curvature is then given by integration the local curvature over the surface of the object:

$$H = \frac{1}{2}\int_{\partial S} \frac{1}{\rho_1} + \frac{1}{\rho_2} dS \tag{2.14}$$

For example, for a sphere of a radius R, we find $\rho_1 = \rho_2 = R$ and $H = 4\pi R$.
In accordance to the first two MF, we calculate the integral mean curvature, by counting the intersection between a test plane and the object in the N-cube. If we allow rotations of the plane by 45^o, there are 13 different planes associated with different normal directions (figure 2.3).

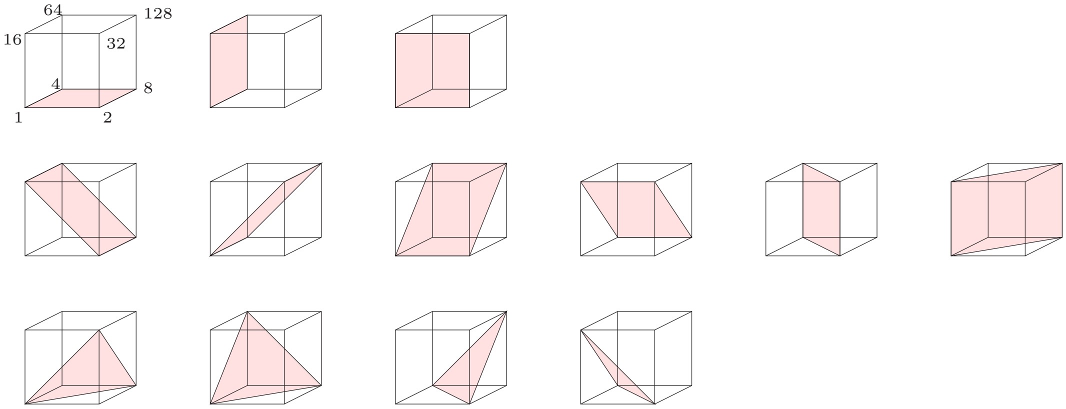

Figure 2.3: Illustration of the 13 planes in a unit cell of a cubic lattice. All 13 planes have different normal vectors.

Again, we numerate the different planes as $g = 1, \ldots, 13$ defined by three in-plane points of the N-cube:

$$\begin{aligned}\mathcal{G} = \{&(1,2,4),(1,4,16),(1,2,16),(2,8,16),(1,4,32),(1,2,64),\\ &(4,8,16),(2,4,32),(1,8,16),(1,8,32),(1,8,64),(2,4,128),(2,4,16)\}\end{aligned} \tag{2.15}$$

Then, the integral mean curvature H can be calculated from

$$3\pi V_2 = H = 4\pi \frac{\sum_l \sum_g [h(l)\theta(l,g)\omega(g)]}{\sum_l \sum_g [h(l)\Delta(g)\omega(g)]} \tag{2.16}$$

where

$$\theta(l,g) = \begin{cases} 1 & : \text{interception with test plane } g \\ 0 & : \text{else} \end{cases} \tag{2.17}$$

We get the same weights ω as for the surface density as long as the lattice is isotropic (Ohser and Mücklich 2000). H is a curvature per volume and has therefore a unit of $[\text{length}]^{-2}$. Thus, $\Delta(g)$ in equation 2.15 denotes the area of the plane g.

2.2.4.4 Euler number

The Euler number, which is also known as the Euler-Poincaré characteristic, is an important measure in topology. In three dimensions it is defined as

$$\chi = \#\ \text{isolated objects} + \#\ \text{holes} - \#\ \text{redundant connection} \tag{2.18}$$

where # stands for 'number of'. Therefore, a single connected object (like a sphere) has the Euler number 1. For a torus, $\chi = 0$, a double torus has $\chi = -1$ and so on. The Euler number is very useful in order to estimate the connectivity of objects but we have to point out that, like all other MF, the Euler number is an integrated value and the same Euler number can be attained by different object configurations. Thus, the interpretation "large negative Euler number = highly connected" is not always correct and we will come back to that point in chapter 8.

Interestingly, the Euler number can also be calculated from the local curvature of a surface. Given the two mean radii of curvature, we define the integral of Gaussian (or total) curvature as

$$4\pi\chi = \int_{\partial S} \frac{1}{\rho_1} \cdot \frac{1}{\rho_2} dS \tag{2.19}$$

As one can show, the integral on the right hand side gives a value of 4π (the surface of a sphere) for any simple closed surface and the definitions 2.18 and 2.19 are equivalent (Weibel 1980).

As demonstrated by Nagel et al. (2000), the Euler number χ can also be calculated from the vector $h(l)$ by

$$V_3 = \chi = \frac{\sum_l [h(l)\theta(l)]}{\sum_l h(l)\Delta} \tag{2.20}$$

where $\theta(l) \in [-2, 1, 0, 1]$ contains the information how the 256 different N-cube configurations contribute to the Euler number (Vogel 1997). A table with the coefficients of θ can be found in Ohser and Mücklich (2000), page 122. Δ in equation 2.20 is the volume of a voxel given by $\Delta = r_x \cdot r_y \cdot r_z$ where r_x, r_y, and r_z are the lattice resolutions. The unit of the Euler number, or more precisely the Euler number density, is therefore $[\text{length}]^{-3}$.

2.2.4.5 Euler number for different neighborhoods

A general problem in the determination of the Euler number on a discrete lattice is related to the definition of neighboring points. As shown in figure 2.4 for the example of a cubic lattice in two dimensions, it can be interpreted differently if two diagonal neighboring points are connected or not. In 2D we could overcome that problem by working with a hexagonal (6-connected) lattice with a unique definition of lattice neighborhood. Unfortunately, there is no such lattice in 3D which is due

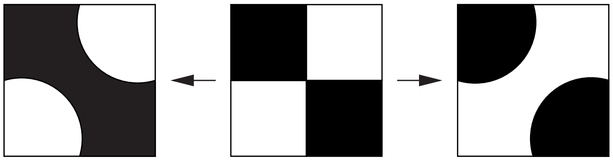

Figure 2.4: *On a cubic lattice in 2D either the black or the white phase can be interpreted as connected to the diagonal neighbor. Therefore, one has to define one phase as 8 connected (8 neighbor nodes) and the other will be automatically 4 connected (Arns 2002).*

to the fact that from the Platonic solids only cubes can fill the whole space without gaps (Wolf-Gladrow 2000).
As a consequence, the Euler number for voxelized data depends on the definition of neighboring lattice nodes. The most common choice in 3D is the assumption of 26 direct neighbors for one phase and 6 neighbors for the other phase, respectively. This can be seen as an extention of figure 2.4 up to three dimensions. But there are other definitions of neighborhood on a 3D cubic lattice possible like a 14- or a 18-connection (Gagvani and Silver 1999). In the context of this work, we used only the 6- and 26-connections which lead to two different Euler numbers indicated as χ_6 and χ_{26}.

2.3 MF for simple geometric object and discretization errors

As a test for the algorithms described above we calculated the MF of cubes and digital representation of spheres. For the generation of digital spheres we used the definition

$$S(D) = \left\{ \vec{r} \in N^3 : (\vec{r} - \vec{c})^2 \leq D^2/4 \right\} \tag{2.21}$$

where the center point is given by $c = D/2 + 1/2$ and D stands for the diameter. The theoretic values for the MF of spheres and cubes are given in table 2.2.

	Sphere (radius r)	Cube (edge length l)
Volume	$\frac{4}{3}\pi r^3$	l^3
Surface area	$4\pi r^2$	$6l^2$
Integral of mean curvature	$4\pi r$	$3\pi l$
Euler number	1	1

Table 2.2: MF of spheres and cubes.

We normalized our measured MF of the digitized objects with these theoretic values (figure 2.5). The determined Euler number was always the correct value of 1 and is not shown in the graph.

2.3.1 MF of digital spheres

The measured MF for the digital spheres show relatively large deviations from the theoretic value at small sphere diameters. This is due to the fact that the digital sphere is badly represented on the lattice. Additionally, with increasing sphere diameters we find both over- and underestimations of the theoretic value.

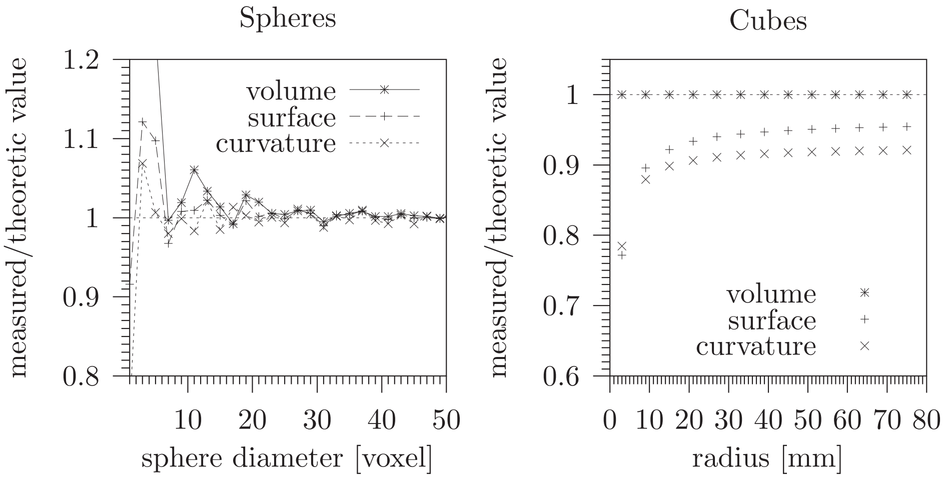

Figure 2.5: Measured values of the MF for voxelized spheres (left) and cubes (right) on a cubic lattice. The values are normalized to the theoretic values.

2.3.2 MF of digital cubes and rotations on a cubic lattice

The situation for the digital cubes is different. Obviously, the determination of the volume is correct since we just count the voxel of the objects. But the algorithms for the determination of the surface and the integral mean curvature lead to an underestimation of the theoretic values. That underestimation can be understood by looking at the 2D example in figure 2.6 which shows a sketch for the estimation of the circumference of a single pixel. As described above, we measure the surface of an object by test lines on the lattice where we accept rotations of 45^o. In 2D there are 4 different directions as shown in figure 2.6 (a). Therefore, the measured circumference is that of a polygon with 8 vertices and causes the underestimation of the theoretic values. As mentioned above, we could limit the rotations on the lattice

to such as 90^o only as shown in figure 2.6 (b). In that case, the theoretical and the measured value for the surface of cubes will be identical. But the estimation of the surface of curved objects (like spheres) will then be biased (Arns 2002).
The deviations for the integral mean curvature can be explained with the same reason.

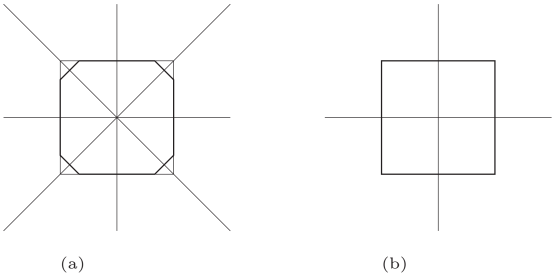

Figure 2.6: The measurement of the circumference depends on the definition of rotations on the lattice. Shown is a single pixel together with 4 (a) and 2 (b) test lines. In case (a) we measure the length of a polygon, in case (b) the length of a square. For further explanations see text.

As a consequence from the determination of the MF for spheres and cubes, in the following we use the algorithm where we accept rotations on the lattice of 45^o. The reason for this is that the structures we are interested in will be better approximated by curved surfaces than by sharp edges and vertices like cubes. The difference between the estimated MF and the 'real' MF of the investigated material will then be dominated by the scanning resolution.

2.4 Minkowski functions

The MF which were presented in the previous sections contain only integrated information about the geometry of a structure. In order to increase the degree of information, we extent the MF to the Minkowski **functions** (Mfs) following a concept developed by K. Mecke in a series of papers (Stoyan 2002). The Minkowski (or morphological) functions are based on the concept of parallel bodies.

2.4.1 Parallel bodies

After Mecke (2000), we define the parallel body X_ϵ of a structure X as the set of all points with distances less than ϵ to X. This is illustrated in figure 2.7 in 2D.

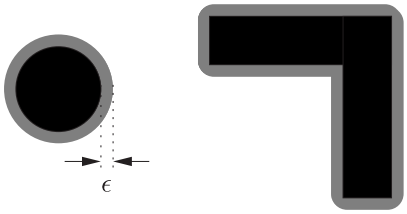

Figure 2.7: Two simple geometric objects (black areas) in two dimensions and their parallel bodies (gray and black area.).

The concept of parallel bodies is analogous to the morphological erosion and we will explain it in more detail in chapter 3.

2.4.2 Interpretation of Mfs for complicated structures

Measuring the MF over the parallel bodies, we get a function of the MF with ϵ as a dependent variable:

$$M_\nu(\epsilon) = V_\nu(A_\epsilon) \tag{2.22}$$

The figures 2.8 and 2.9 show the parallel bodies and the Minkowski functions for a complicated structure.

Since the structure is represented on a lattice, we get only few parallel bodies and therefore only discrete points of the Minkowski functions. Nevertheless, this example illustrates the general shape of the four Minkowski functions. Obviously, the volume density decreases monotonously with increasing ϵ as the fraction of the white phase is getting smaller. In this example, the surface density is also a monotone function over ϵ. But other configurations are possible where the surface density first increases and then decreases toward zero. The integral mean curvature of the original structure is close to zero which indicates that both convex and concave parts are equally distributed over the image. The parallel bodies provide an augmentation of the

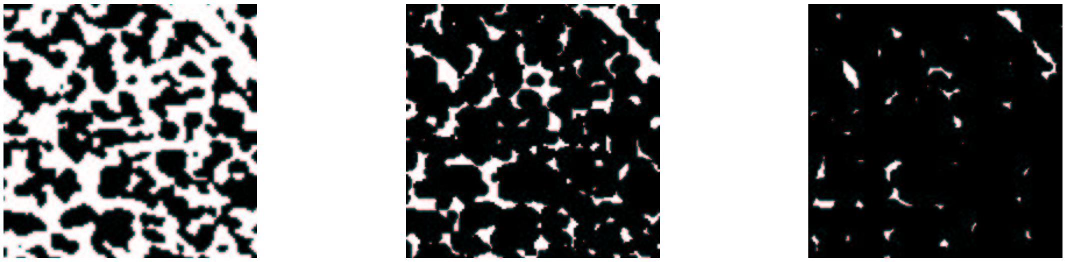

Figure 2.8: Two parallel bodies for a complicated structure (black phase treated as the object). The calculation was done in 3D while only cross sections are plotted.

convex part (which are counted negative) and the curvature reaches a minimum until it converges to zero for large ϵ. Finally, the large negative Euler number of the initial structure is due to a high connectivity of the structure. In the given structure, there are no completely surrounded objects and the Euler number is given by the number of objects minus the number of redundant loops. (Plotted in figure 2.9 is the Euler number per volume.) Concerning the 26-connectivity, the Euler number decreases even more for a small ϵ since the parallel body leads to more diagonal connections. But with increasing ϵ, the number of redundant connections decreases dramatically and the number of isolated (white) objects increases. The Euler number reaches a maximum when the number of isolated white regions within the black objects is maximal. As for the mean curvature, the Euler number has to converge to zero for large ϵ because the object fills the whole available space.

As pointed out before, we will use the concept of parallel bodies for morphological image analysis in chapter 3. The Minkowski functionals will be investigated in detail for the reconstruction of given complicated structures (chapter 8).

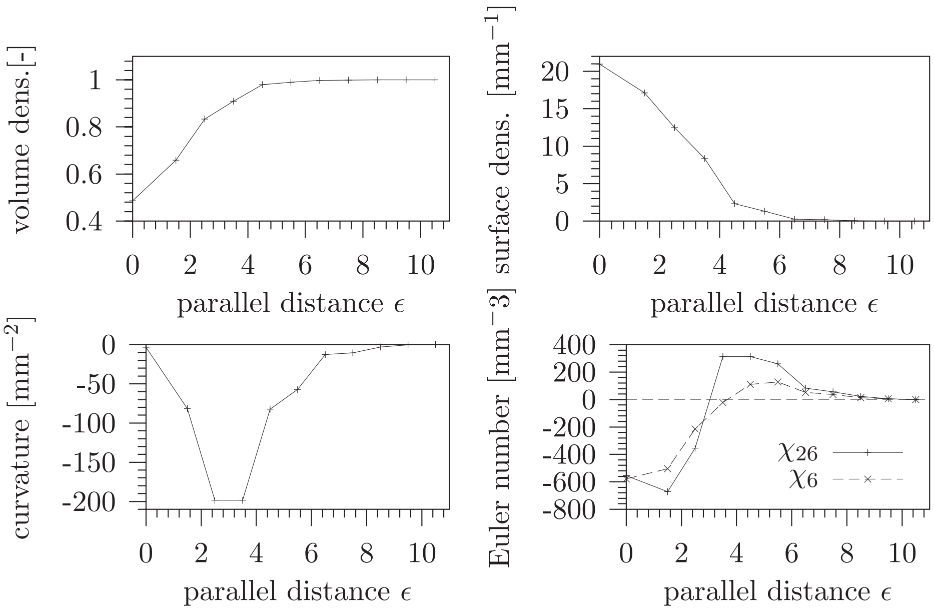

Figure 2.9: Minkowski functions for the structure shown in figure 2.8. ϵ given in lattice units.

3 Morphological image analysis

Soille (1999) defines *morphology* as a theory for the analysis of spatial structures. Thus, it is both a theory and powerful image analysis technique. In this chapter we will give an introduction to morphology with the focus on the so-called image processing operators. These will be widely used in the later chapters of this thesis.

3.1 Morphological operators

Morphological operators, like erosion and dilation, can be seen as tools to extract relevant structures of an image. The basic idea behind that approach is to probe the image by an object with known shape called *structuring element* (SE). Here, we limit the analysis to SE with the same dimension as the investigated image, which are sometimes called flat SEs (Soille 1999). Common (flat) SE in 2D are in disks, squares, and line segments and in 3D spheres, cubes, and line segments.

3.1.1 Erosion

The morphological erosion determines the part of the image where the structuring element fits the set. In other words: The eroded set are all points for which the SE completely lies within the set. This is illustrated in figure 3.1

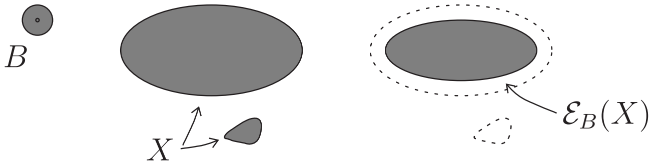

Figure 3.1: Erosion $\mathcal{E}$ of a set X by a disk B. The small element vanishes by the erosion since B never fits it (modified after Soille (1999)).

Mathematically, we define the erosion as

$$\mathcal{E}_B(X) = \{x | B_x \subseteq X\} \tag{3.1}$$

where B_x is the SE.

We can rewrite equation 3.1 using the Minkowski subtraction $\ominus$ as

$$\mathcal{E}_B(X) = X \ominus \breve{B} \tag{3.2}$$

where $\breve{B}$ is the reflected set of B with respect to the origin (Ohser and Mücklich 2000). When working with symmetric SE like disks or spheres, we don't have to distinguish between B and $\breve{B}$. Then, the Minkowski subtraction and the Minkowski addition (which will be introduced in the next section) provide concise morphological expressions.

3.1.2 Dilation

The dual operator to the erosion is called dilation. The dilation determines all points in the image which are covered by the SE when the locus lies insert X. Therefore, it is defined as

$$\mathcal{D}_B(X) = \{x | B_x \cap X \neq 0\} \tag{3.3}$$

This is illustrated in figure 3.2.

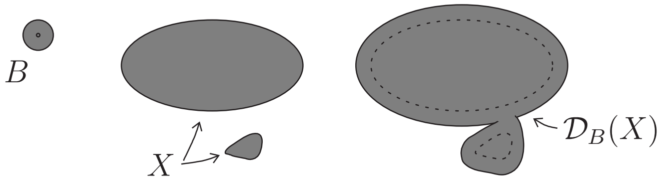

Figure 3.2: Dilation $\mathcal{D}$ of a set X by a disk B. In that example the two objects melt together by the dilation.

Rewriting equation 3.3 with the Minkowski addition $\oplus$ yields to

$$\mathcal{D}_B(X) = X \oplus \breve{B} \tag{3.4}$$

As a consequence, the concept of parallel bodies from section 2.4 can be seen as the Minkowski addition (subtraction) with disks (or spheres in 3D) as SE.

3.1.3 Opening and closing

Combining the erosion and the dilation of an image, leads to the morphological operators called opening and closing. The morphological opening of the set X is defined by

$$\mathcal{O}_B(X) = (X \ominus \breve{B}) \oplus B \tag{3.5}$$

i. e. the dilation is applied after the erosion step. Looking at the figures 3.1 and 3.2, one can see that the opening removes all components which are smaller than

the SE. Successive openings are therfore used to determine a size distribution of the components of an image as it will be explained in the next section.
To make the list complete, we give also the definition of the morphological closing which consists of a dilation followed by an erosion of X

$$\mathcal{C}_B(X) = (X \oplus \check{B}) \ominus B \tag{3.6}$$

In the context of this work, it is not necessary to distinguish between opening and closing rigorously. As long as we are working with binary images and symmetric SE, the opening and the closing are dual processes applied to the white phase or the black phase, respectively.

3.2 Granulometry

The granulometry, or the size distribution, is a concept which is comparable to a sifting process. For a given image, we are interested in the components that are sifted for a certain mesh opening. That process is closely related to the morphological opening with special SE since the granulometry has to fulfill the following axioms (Soille 1999):

- Anti-extensivity: the components that remain in the sieve are a subset of the initial image.
- Increasingness: when sifting only a subset of the image, the components in the sieve are a subset of those remaining in the sieve after sifting the whole set.
- Absorption: Sifting with a mesh opening s_1 followed by sifting with s_2 will give the same result as sifting first with s_2 and then with s_1. Additionally, the remaining depend only on the size of the largest sieve.

The morphological opening $\mathcal{O}$ satisfies the two first axioms automatically. But for the absorption, one has to be careful in the choice of the SE which have to fulfill the relation

$$\lambda' \leq \lambda \Rightarrow \mathcal{O}_{\lambda\mathcal{B}} \subset \mathcal{O}_{\lambda'\mathcal{B}} \tag{3.7}$$

In other words, smaller SEs has to be a subset of larger SEs. Therefore, squares in 2D and cubes in 3D where λ is the edge length are a common choice. Working with squares or cubes provides that all the properties for the granulometry are fulfilled even on cubic lattices. Then, we get the cumulative morphological size distribution by

$$f(\lambda) = \frac{\mathrm{Vol}[\mathcal{O}_{\lambda\mathcal{B}}]}{\mathrm{Vol}[X]} \tag{3.8}$$

where Vol stands for the volume of its argument. If X is the pore space, $f(\lambda)$ represents the pore-size distribution and if X is the void space, it represents the grain-size distribution, respectively.
For discrete disks (or spheres in 3D) on a lattice which are given by

$$S(D) = \left\{ \vec{r} \in N^3 : (\vec{r} - \vec{c})^2 \leq D^2/4 \right\} \tag{3.9}$$

the requirement of the absorption axiom is violated as one can see from figure 3.3. This problem can be solved in two different ways: the first one is using only disks or spheres where the diameter is given by $D = 2 \cdot N + 1,\ N \in \mathcal{N}$. Another way, described by Hilpert and Miller (2001), is to use structure elements S' which are defined through

$$S'(1) = S(1) \qquad \text{and} \qquad S'(n) = S(n) \cup S(n-1) \tag{3.10}$$

For the purpose of this work, we followed the first approach, using only disks or spheres with odd diameters since S' is no longer symmetric and still don't prevent the violation of the "absorption"-axiom.

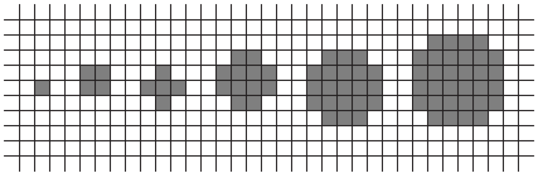

Figure 3.3: Representation of disks on a cubic lattice (digital disks) with increasing diameter.

Nevertheless, even if all three axioms are fulfilled, the choice of the SE has a strong influence on the result of the granulometry which can be shown with very simple examples. Figure 3.4 represents a distribution of digital disks with different diameters and the result of two opening steps where the SE are either disks and or squares. This can be interpreted as a sifting of the objects by sieves where the mesh consist of either quadratic or circular shaped holes.
Depending on the SE, we get different size distributions as pointed out in figure 3.5. In that example, only the granulometry with disk as SE gives the expected values of objects with dimensions between 8 and 14 lattice nodes where the largest fractions can be found in the range of 10 and 14 lattice nodes. In contrast, the granulometry with squares leads only to one maximum in the size distribution at 10 lattice nodes. That example illustrate the error that lies in the granulometry determined by morphological operations.

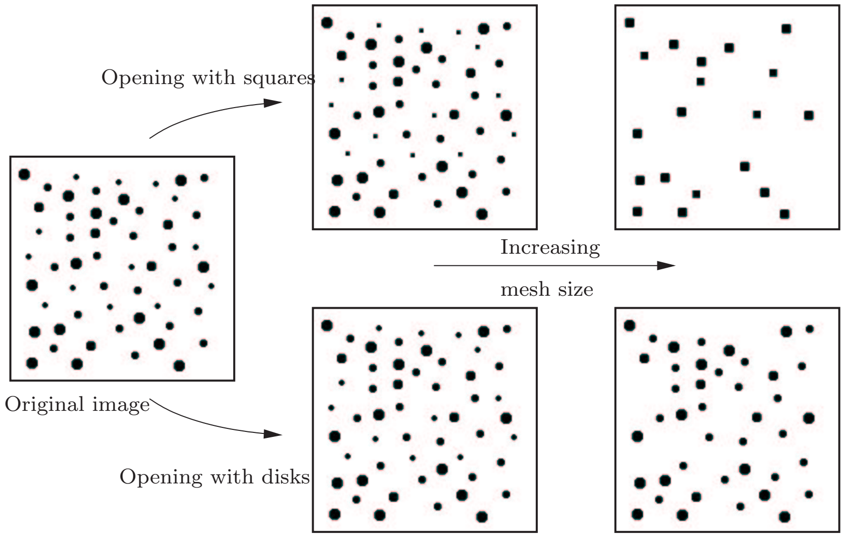
Opening with squares
Original image
Opening with disks
Increasing
mesh size

Figure 3.4: Results of morphological opening with squares (upper row) and discrete disks as SE. At each opening step, the diameter of the disk and the vertex length of the square are identical. The original image is a distribution of digital disks with different diameters.

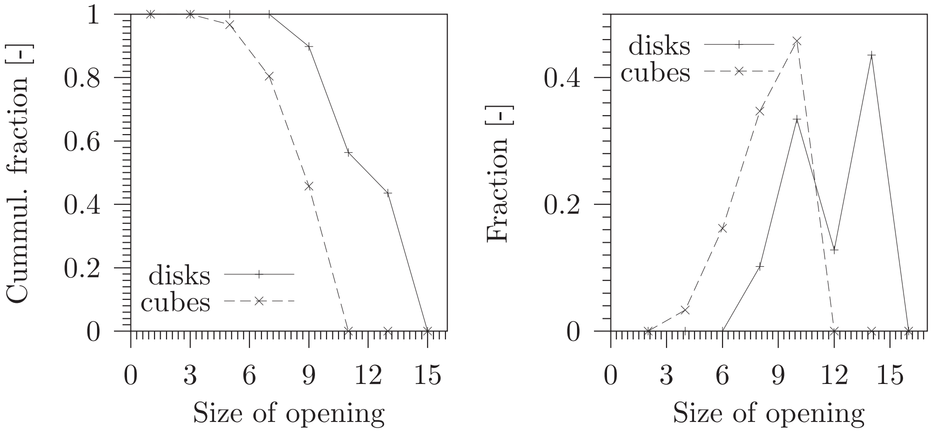

Figure 3.5: The size distribution of the disks from figure 3.4 determined by a granulometry with disks and with squares. The figure on the left hand side is the cumulative fraction of the objects and its derivative on the right hand side.

3.2.1 Speeding up the erosion with spheres

The morphological erosion and dilation with spheres have a wide range of application. Beside the granulometry, they can also be used for the determination of pressure-saturation curves as we will point out in a later chapter. From a computation point of view, the erosion and dilation with spheres are very time consuming since the cost of its calculation is proportional to D^3 where D is the sphere diameter. This is due to the fact that at each voxel of the image, D^3 neighboring voxel have to be marked.[1]

We have seen from the example in figure 3.5 that the morphology-based granulometry of a complex structure can only be seen as an approximation as long as the objects are not identical to the SE. Therefore, instead of the digital spheres as SE, we propose so-called modified spheres which reduce the computational time significantly. The modified spheres are based on a single voxel which is dilated by a a cross (3×3×3 voxel) and a cube (3×3×3 voxel), in alternating steps. The result of the first 6 modified spheres is shown in figure 3.6. The cost of calculating the erosion with a modified spheres with a diameter D can be estimated by $N \cdot 3^3(D-1)/2$ since the erosion can be decomposed into $(D-1)/2$ erosions. Each of these erosion step is performed only with a cross or a cube, both consisting of 3^3 voxel.

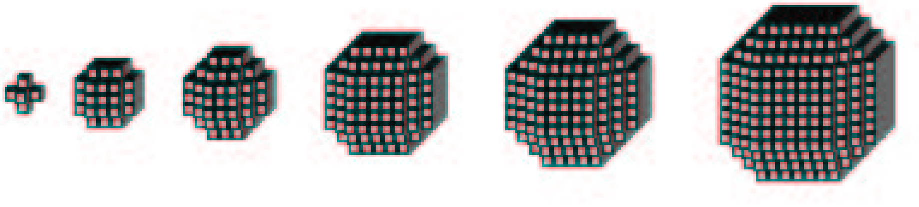

Figure 3.6: Modified digital spheres which are the result of alternating dilation of a single voxel with a cross and a cube (3×3×3 voxel).

For the purpose of illustrating the differences between the digital spheres and the modified spheres, we show in figure 3.7 the cumulative pore fraction of a complex structure as a result of morphological openings with both SE. This is an anticipation of results presented in chapter 6. As one can see from figure 3.7, we get almost the same cumulative pore size distribution while the computational time is dramatically reduced.

---

[1] The number D^3 is only correct for the erosion with cubes and a little smaller for spheres which is not of importance for the estimation.

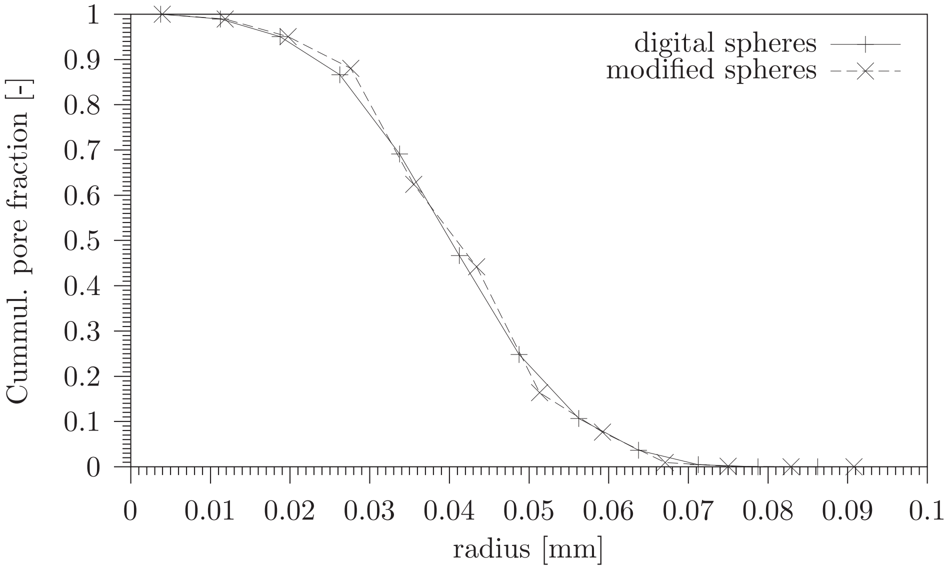

Figure 3.7: Cumulative pore fraction as a result of morphological openings with digital spheres and modified spheres as explained in the text.

3.2.2 Interception length density function

As we have seen before, the morphological granulometry leads to differences in the pore size or grain size distribution depending on the choice of the SE. Therefore, it is useful to compare the results to another parameter, the interception length density function (ILDF). The interception length (or chord length) density function $P^i(z)$ is defined as the probability of finding a interception of length between z and $z + dz$ in phase i (Torquato 2002) and normalized to unity. The definition is illustrated in figure 3.8.

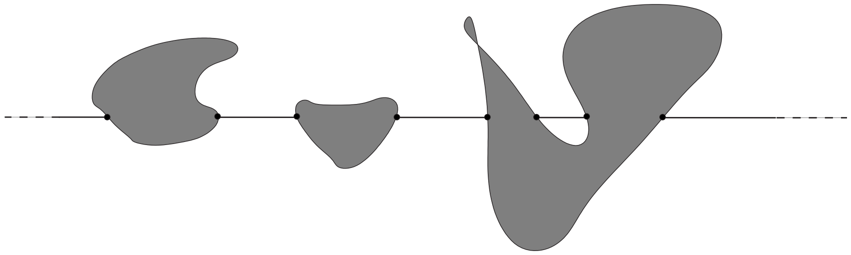

Figure 3.8: Illustration of the interception length between the structure elements (gray) and an infinite long line. Modified after Torquato (2002).

Depending on the investigated phase, we determine either the length of the pores or the length of the void space in the direction of the test line. Obviously, the test line can undergo all rotations and translations and the different differences of the ILDF versus the direction denotes anisotropies in the structure. Since we are only interested in the overall interception length distribution on a cubic lattice, we restrict the orientations of the test lines to three directions parallel to the main axes. Beside the later use of the ILDF in comparison to the results from the granulometry, the ILDF will serve an input parameter for the reconstruction of the investigated structures.

4 Model for the determination of capillary pressure-saturation curves

In this chapter, we describe a model which can be used for the determination of the capillary pressure-saturation relation ($P^c - S^w$ curve). This method has been proposed by Hilpert and Miller (2001) known as pore-morphology-based (PMB) simulation.

4.1 Pore-morphology-based simulation (PMB)

4.1.1 Background

The following model description is based on the work of Hazlett (1995) and Hilpert and Miller (2001).

The basic idea is to calculate the quasi-static states for the distribution of the wetting phase (WP) and the non-wetting phase (NWP) in a 3D geometry. Starting with totally saturation, the capillary pressure is reduced stepwise while a part of the pore space will be filled with non-wetting phase if

- it is "large" enough
- it has a connection to the NWP reservoir.

In order to determine the pore space that will be accessible for the NWP at each pressure step, we decompose the image with the pore radius as ordering parameter. This can be done by the morphological opening which has been described in chapter 3 (equation 3.5). As before stated: The morphological opening determines the part of a set X where the structuring element (SE) B fits the set.

The choice of B determines the form of the interphase between WP and NWP. A common choice are spheres with different diameters which leads to spherical interphase between the two phases.

For continuous data, one can directly use the opening with spheres as SEs to get a size distribution since if fulfills the relation

$$\mathcal{O}_{B'} \subset \mathcal{O}_B \qquad \forall \quad B' > B \tag{4.1}$$

which is the concept of a granulometry (see chapter 3).

As pointed out before, one has to be careful by the choice of the SE for digitized data. In order to respect equation 4.1, we use the straight forward definition of digital spheres given by

$$S(D) = \left\{ \vec{r} \in N^3 : (\vec{r} - \vec{c})^2 \leq D^2/4 \right\} \tag{4.2}$$

where the center point of the sphere is $c_i = \frac{D}{2} + \frac{1}{2}$ and we accept only odd diameters given by $D = 2i + 1$, $i \in N$.

4.1.2 Simulation steps

Then, the steps of the algorithm to determine the quasi-static primary drainage curve are as follows:

1. At the beginning, all of the pore space is water filled and the capillary pressure P^c is zero. The medium is connected with one side to a water phase reservoir while the opposite side has a connection to the air-phase. All other sides are closed.

2. The pore space P is eroded by spheres with decreasing diameter D. We start with the maximum diameter D_m due to an erosion of the entire pore space:

   $$P \ominus \breve{S}(D) \equiv 0 \qquad \forall D \geq D_m \tag{4.3}$$

   We identify the diameter D with the corresponding pressure (Laplace equation)

   $$P^c = \frac{4\gamma}{D} = \frac{2\gamma}{R} \tag{4.4}$$

   where γ is the surface tension.

3. The eroded pore space from step 2 can only be filled with NW, if they are connected to the NWP reservoir. Therefore, we remove all isolated regions and dilate the remaining pores pace with the same sphere as in step 2.

4. Compute the NWP saturation S^n and proceeds with step 2 while decreasing the diameter of the SE.

This approach neglects effects like WP film flow or trapped water. For our simulations, we assumed a vanishing contact angle, $\theta = 0°$ but small non-zero contact angles should only lead to a modification of equation 4.4 to

$$P^c = \frac{4\gamma \cos\theta}{D} \tag{4.5}$$

the so-called Young-Laplace equation.

4.1.3 PMB model and non-spherical interfaces

The complete procedure of the PMB method as described above is based on the assumption that (for quasi-static states) the interface between the WP and the NWP is spherical. Obviously, this is a limitation and leads to an overestimation of the pressure which is necessary to drain the associated pore region. As an illustration, we simulated the drainage of a capillary tube with elliptical cross section. Theoretically, the elliptic capillary tube drains (at once) if

$$P^c > \gamma(\frac{1}{R_1} + \frac{1}{R_2}) \tag{4.6}$$

For example, if the radii of the ellipse are given by $R_2 = 2 \cdot R_1$, the PMB model determines the first desaturation step at a pressure of $P^c = 2\gamma/R_1$. This is about 30% higher than the theoretical value of $P^c = \gamma(1/R_1 + 1/2R_2) = 3/4 \cdot 2\gamma/R_1$. Additionally, the $P^c - S^w$ curve determined by the PMB model gives the impression, that it takes several pressure steps to drain the elliptic capillary tube (figure 4.1) which is an artefact that will always occur if the SE does not exactly fit the pore space or the shape of the interface to be more precisely.[1] As a consequence, we expect that the PMB method always overestimates the relevant capillary pressure.

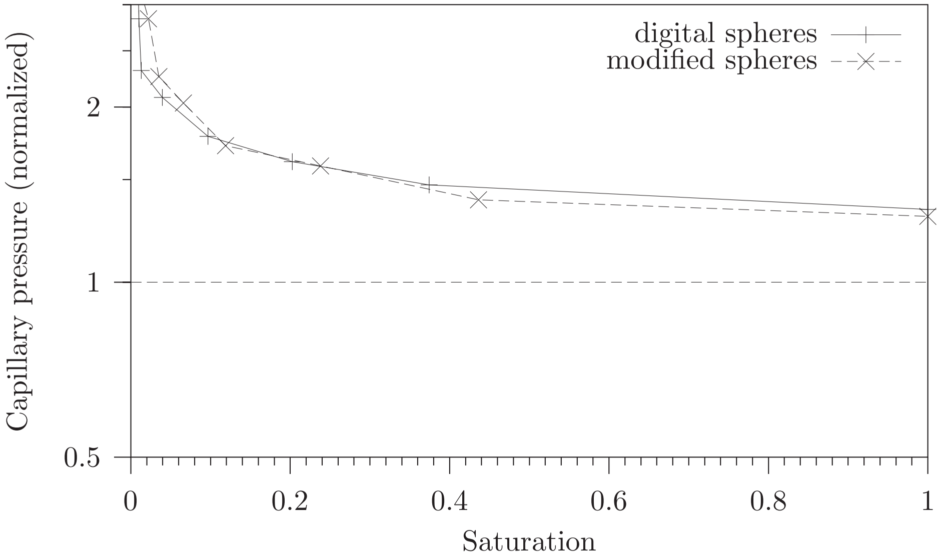

Figure 4.1: Capillary pressure-saturation curve of a single elliptic capillary tube as determined by the PMB model. The pressure is normalized to a theoretical value which was set to be 1. The deviations between the digital spheres and the modified spheres are explained in section 4.2.

---

[1] The same effect has been already discussed in the example of "sifting" with different SE (figure 3.7).

4.1.4 Limitations of the PMB model at small saturations

Another bias of the PMB model has already been described by Hilpert and Miller (2001). At small saturations, the interfaces between WP and NWP transform into pendular rings and again, the capillary pressure cannot be determined from equation 4.4 since there are two different radii of curvature.

4.2 PMB model with modified spheres as SE

As pointed out before in chapter 4.2, the use of modified spheres instead of digital spheres reduces the computing time significantly. In the special case of the PMB model, we need successive erosions with increasing diameter. In this case, the erosion with modified spheres is even more efficient, since each erosion step needs only a constant number of operations.

While using the modified spheres as SE, the application of the Laplace equation (4.4) can still be used. But the radius of curvature differs from the radius of the digital sphere. We therefore propose a correction by measuring the integral mean curvature of the modified spheres. As explained in chapter 2, the curvature of a sphere is given by $H = 4\pi r$. Then the according capillary pressure is given by the Laplace equation

$$P^c = \frac{8\pi\gamma}{H} \tag{4.7}$$

and we only have to measure the integral mean curvature of the SE which can be done by the algorithm which have been explained in chapter 2.

Typical pressure-saturation curves for a complicated structure are plotted in figure 4.2.

The two relations were determined using the PMB model with digital spheres as well as with modified spheres. Obviously, there are differences between the curves, especially near saturation. This is due to the fact that the volume of the modified spheres is smaller compared to the digital sphere. In the simulation the pores drain at a smaller capillary pressure and a larger portion of the WP remains in the "corner" of the pores. For a complete understanding of this effect it is worth study the elliptic capillary tube again. In this case, the largest modified sphere that fits the elliptic cross section has a smaller volume than the digital sphere. Additionally, the modified sphere has a higher mean curvature according to a smaller capillary pressure as shown in figure 4.1.

Nevertheless, the systematic errors of the PMB model are still large compared to the effects caused by the different SEs. As long as the interfaces between the NWP and the WP are spherical the PMB simulations lead to reliable capillary pressure-saturation relations. In all other cases, there will be a systematic overestimation of the required capillary pressure.

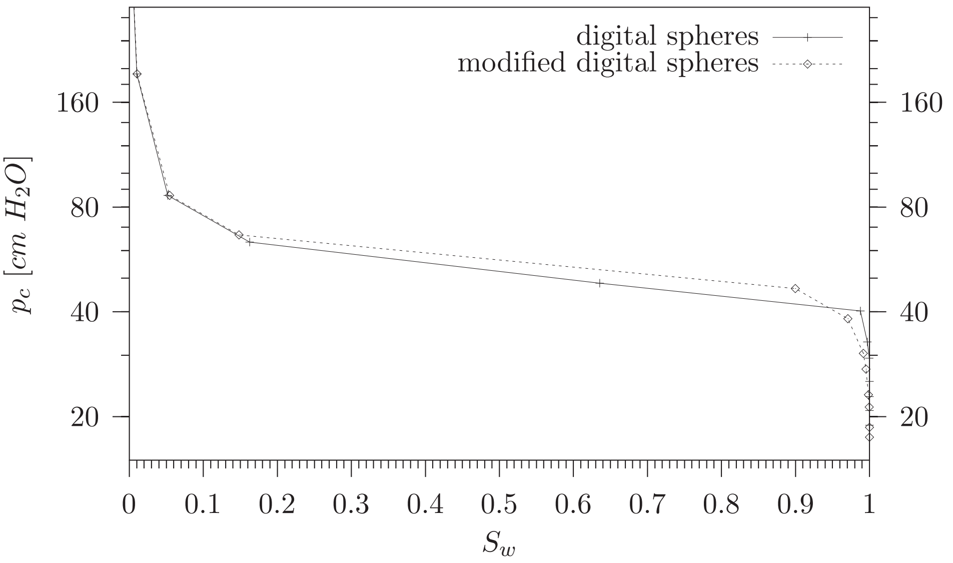

Figure 4.2: Differences between the pressure-saturation curve from the PMB model working either with digital spheres or modified digital spheres. Details about the simulated pressure-saturation relations will be described in chapter 6.

5 Lattice Boltzmann model

In the framework of this work we use Lattice-Boltzmann (LB) simulations for solving the Navier-Stokes equation in complicated geometries.

5.1 The lattice-Boltzmann model

5.1.1 The Boltzmann equation

Proposed in 1986 (Frisch et al. 1986), the Lattice Boltzmann method has been developed to a very efficient tool of computational fluid dynamics (Wolf-Gladrow 2000). The LB simulation can be seen as an alternative to conventional numerical approaches such as finite element and difference methods in order to solve the Navier-Stokes equation:

$$\frac{D\vec{u}}{Dt} = -\frac{1}{\rho}\vec{\nabla}p + \nu\vec{\nabla}^2\vec{u} \tag{5.1}$$

where $\vec{u}$ is the fluid velocity and ν the fluid viscosity. The Navier-Stokes equation describes the motion of a fluid under external forces, e. g. the pressure gradient $\vec{\nabla}p$. In contrast, the LB method starts with a description of the fluid on a *microscopic* level by the Boltzmann equation

$$\frac{\partial f}{\partial t} + v_i\frac{\partial f}{\partial x_i} + F\frac{\partial f}{\partial v_i} = \Omega(f), \qquad i = 1, 2, 3 \tag{5.2}$$

where f is a particle distribution with a microscopic velocity v and F is an external force. Therefore, the expression $f(\vec{x}, \vec{v}, t)d^3xd^3v$ is the probability to find a particle in the volume d^3x around $\vec{x}$ and with the velocity between $\vec{v}$ and $\vec{v} + d\vec{v}$.

Equation 5.2 has been derived first by Boltzmann in the 19th century in order to describe the behavior of a gas on a molecular level. Its derivation needs the following assumptions (Wolf-Gladrow 2000):

i) the collision between the particles can be described by a two particle interaction

ii) the collisions are not correlated to each other ('molecular chaos')

iii) external forces do not modify the particle interaction

The left hand side of equation 5.2 is due to an advective transport of the particles where the right hand side is a so-called collision operator. The exact form of Ω is difficult and can be found analytically for simple systems only. Fortunately, the macroscopic dynamic of a fluid is often not very sensitive to the underlying details in the microscopic physics. As a consequence, the physics on the microscopic scale can be described in a much simpler way.

5.1.2 BGK collision operator

One possible simplification is attributed to Bhatnagar, Gross, and Krook (often referred as BGK) and replaces the collision operator in equation 5.2 by the expression

$$\Omega = -\frac{1}{\tau}(f - f^{eq}) \tag{5.3}$$

where f^{eq} is the distribution function in the equilibrium and τ the relaxation time needed to reach f^{eq}. In this sense, the fluid is described on a mesoscopic level since we are only interested in the average behavior of the fluid ensembles[1]. In the BGK model, it is assumed that tendency of the fluid toward an equilibrium state can be described by only one relaxation time τ. Intuitively and as we will see later, τ may be related to the viscosity of the fluid since that parameter describes how fast disturbances will be damped out.

5.1.3 Discretization of the Boltzmann equation

The next step toward the LB method is a discretization of the Boltzmann equation in time and space:

$$f_i(\vec{x} + \vec{e}_i, t+1) = f_i(\vec{x}, t) - \frac{1}{\tau}[f_i(\vec{x}, t) - f_i^{(eq)}(\vec{x}, t)] \qquad \text{where} \quad i = 0, \ldots \tag{5.4}$$

where the index i and the lattice velocity vectors $\vec{e}_i$ depend on the underlying lattice as we will see later in this section.

5.1.4 Chapman-Enskog expansion

With a so-called Chapman-Enskog expansion, one can show that equation 5.4 is an approximation of the Navier-Stokes equation (5.1). While the complete derivation is beyond the context of this work and can be found in different publications (Wolf-Gladrow 2000, Tölke 2001, Buick 1997), the basic ideas of the Chapman-Enskog expansion are as follows:

---

[1] The fluid ensemble can be seen as an extension of particle distributions. The particle distribution is represented by the number of discrete particles per volume while the ensemble is described by a real number such as the fluid mass per volume.

Starting with the equation 5.4, we assume that this equation is valid for arbitrary lattice spacing and time steps:

$$f_i(\vec{x}+\delta\vec{e}_i, t+\delta) = f_i(\vec{x},t) - \frac{1}{\tau}[f_i(\vec{x},t) - f_i^{(eq)}(\vec{x},t)] \tag{5.5}$$

The parameter δ can be seen as an order parameter, where $\delta = 1$ recovers equation 5.4.

We now apply a Taylor expansion to equation 5.5 and obtain

$$\sum_{n=1}^{\infty} \frac{\delta^n}{n!}\left[\vec{e}_i \cdot \vec{\nabla} + \frac{\partial}{\partial t}\right]^n f_i(\vec{x},t) = -\frac{1}{\tau}[f_i(\vec{x},t) - f_i^{(eq)}(\vec{x},t)] \tag{5.6}$$

and expand the distribution functions around the equilibrium ($f^{(eq)} \equiv f^{(0)}$)

$$f_i = \sum_{n=1}^{\infty} \delta^n f_i^{(}n) = f_i^{(0)} + \delta f_i^{(1)} + \delta^2 f_i^{(2)} + \dots \tag{5.7}$$

where the mass conservation is guaranteed by $\rho = \sum_i f_i^{(0)}$ and $\rho = \sum_i f_i^{(n)} = 0$ for $n > 0$. Momentum conservation is guaranteed by $\rho\vec{u} = \sum_i \vec{e}_i f_i^{(0)}$ and $\sum_i \vec{e}_i f_i^{(n)} = 0$ for $n > 0$.

Substituting equations 5.6 and 5.7 into 5.5 and successively evaluation with increasing order n leads to the first

$$\left[\vec{e}_i \cdot \vec{\nabla} + \frac{\partial_0}{\partial t}\right] f_i^{(0)} = -\frac{1}{\tau} f_i^{(1)} \tag{5.8}$$

and the second order term

$$\left[\vec{e}_i \cdot \vec{\nabla} + \frac{\partial_0}{\partial t}\right] f_i^{(1)} + \frac{1}{2}\left[\vec{e}_i \cdot \vec{\nabla} + \frac{\partial_0}{\partial t}\right]^2 f_i^{(0)} + \frac{\partial_1}{\partial t} f_i^{(0)} = -\frac{1}{\tau} f_i^{(2)} \tag{5.9}$$

where the time derivative ∂_n is defined through

$$\frac{\partial}{\partial t} = \sum_{n=0}^{\infty} \delta^n \frac{\partial}{\partial t} = \frac{\partial_0}{\partial t} + \delta\frac{\partial_1}{\partial t} + \delta^2 \frac{\partial}{\partial t} + \dots \tag{5.10}$$

From the equations 5.8 and 5.9, we directly obtain the mass balance equation up to second order accuracy in δ:

$$\frac{\partial \rho}{\partial t} + \vec{\nabla}(\rho\vec{u}) + O(\delta^2) = 0 \tag{5.11}$$

Additionally, the multiplication of the equations 5.8 and 5.9 with $\vec{e}_i$ and the summation over i yields to the momentum conservation to second order where the momentum flux tensor depend on the lattice vectors $\vec{e}_i$.

5.1.5 Underlying lattice and equilibrium distribution functions

Up to this point, the results of the Chapman-Enskog expansion were independent of the underlying lattice used for the discretization in equation 5.5. The further evaluation, i. e. the determination of the equilibrium distribution functions, depend on the lattice structure. In three dimensions, the cubic lattice is a common choice and the number of lattice velocity vectors depend on the definition of neighbored points.

Therefore, different configurations like 15-, 19-, and 27-velocities models are possible. As illustrated in figure 5.1 for the 19-velocities case, the model uses 19 discrete lattice velocities including the velocity vector $\vec{0}$. In other words, one node on the lattice has 18 direct neighbors.

In the context of this work, we used the 19-velocities (Q19D3) model since it provides a good balance between computational reliability and efficiency Mei et al. (2000).

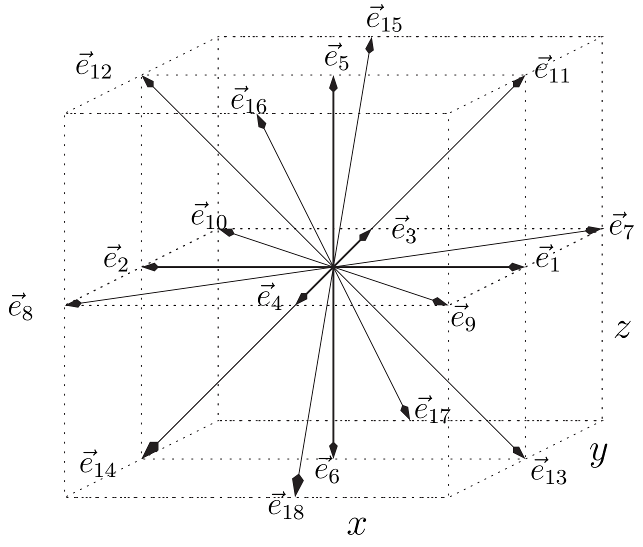

Figure 5.1: Lattice velocity vectors for the Q19D3 model.

In the further steps of the Chapman-Enskog derivation, the lattice velocity vectors $\vec{e_i}$ (as shown in figure 5.1) are introduced in the equations 5.8 and 5.9. Additionally, it is assumed that the equilibrium distribution depend only on the macroscopic velocity $\vec{u}$ and the corresponding velocity vector $\vec{e_i}$:

$$f_i^{(eq)} = A_i + B_i \vec{e}_i \cdot \vec{u} + C_i (\vec{e}_i \cdot \vec{u})^2 + D_i \tag{5.12}$$

while the rotational invariance requires that only scalar products among $\vec{u}$ and $\vec{e_i}$ appear. That assumption is due to results from kinetic gas theory where the equilibrium depends only on the temperature and the spatially averaged velocity.

The further derivation shows that the choice of the unknown parameters A_i, B_i, C_i, and D_i is not unique and they are chosen such that the derived momentum flux tensors (of first and second order) represent best the ones in the Navier-Stokes equation.

5.1.6 Parameters of the Q19D3 lattice

One realization for the equilibrium distributions on a Q19D3 lattice is as follows (Mei et al. 2000):

$$f_0^{(eq)} = \frac{1}{3}\rho\left(1 - \frac{1}{2}v^2\right), \qquad \text{(type 0)} \tag{5.13}$$

$$f_i^{(eq)} = \frac{1}{18}\rho\left[1 + \vec{e}_i \cdot \vec{v} + \frac{1}{2}(\vec{e}_i \cdot \vec{v})^2 - \frac{1}{2}v^2\right], \qquad i = 1, ..., 6 \tag{5.14}$$

$$f_i^{(eq)} = \frac{1}{36}\rho\left[1 + \vec{e}_i \cdot \vec{v} + \frac{1}{2}(\vec{e}_i \cdot \vec{v})^2 - \frac{1}{2}v^2\right], \qquad i = 7, ..., 18 \tag{5.15}$$

Then, the fluid density is given by

$$\rho(\vec{x}, t) = \sum_i f_i(\vec{x}, t) \tag{5.16}$$

and the fluid velocity is defined through

$$\rho\vec{v} = \sum_i \vec{e}_i f_i(\vec{x}, t) \tag{5.17}$$

In the Chapman-Enskog expansion, it is assumed that the that the equation of state is that of an ideal gas with $p = \rho c_s^2$ where $c_s = 1/\sqrt{3}$ is the speed of sound in the system. Then, the (kinematic) viscosity ν in the Navier-Stokes equation is given by

$$\nu = \frac{2\tau - 1}{6} \tag{5.18}$$

Equation 5.18 requires $\tau > 1/2$ in order to keep the viscosity positive.

5.1.6.1 Collision and streaming step

For the transformation of equation 5.4 into programming code it is useful to decompose it into two steps:

$$\text{collision step:} \quad \tilde{f}_i(\vec{x}, t) = f_i(\vec{x}, t) - \tfrac{1}{\tau}[f_i(\vec{x}, t) - f_i^{(eq)}(\vec{x}, t)] \tag{5.19}$$

$$\text{streaming step:} \quad f_i(\vec{x} + \vec{e}_i, t + 1) = \tilde{f}_i(\vec{x}, t) \tag{5.20}$$

Then, the collision can be calculated for each lattice node separately. In the streaming step, the distributions travel along the lattice velocity vectors to its neighboring nodes.

5.2 Fluid-solid interactions

Since we are interested in the flow simulations in complicated geometries, the simulation between the fluid an solid walls is of great importance.
We call this interaction boundary condition (BC) but it has to be distinguished from the pressure boundary conditions which will be explained in the next section. In the LB model, different types of BC like no-slip or slip BC can be used. For our simulations, we used no-slip BC which are easy to implement by so-called bounce-back rules: the fluid colliding with a stationary wall reverses its momentum. Therefore, instead of a collision step the distributions on solid nodes were rearranged by

$$\tilde{f}_i(\vec{x},t) = f_{i+1}(\vec{x},t) \qquad i = 1,3,5,\dots \tag{5.21}$$

$$\tilde{f}_i(\vec{x},t) = f_{i-1}(\vec{x},t) \qquad i = 2,4,6,\dots \tag{5.22}$$

As shown by Zou and He (1997), the bounce-back scheme attains second-order accuracy if we assume that the boundary is placed halfway between the fluid and the solid nodes. This is illustrated in figure 5.2.

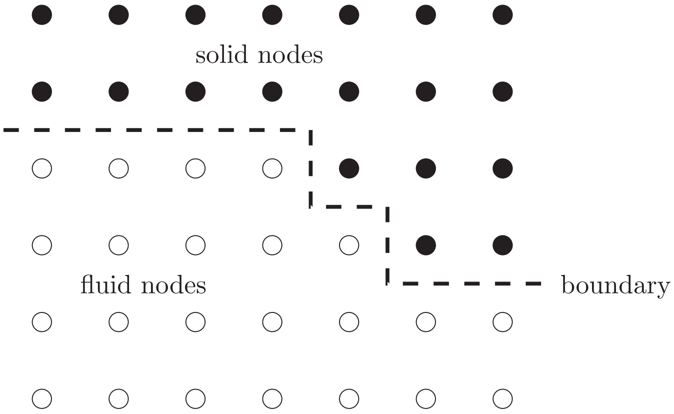

Figure 5.2: Illustration of fluid and solid nodes together with the imaginary boundary in the middle.

5.2.1 Pressure boundary conditions and volume forces

In the common form of the Navier-Stokes equation

$$\frac{D\vec{u}}{Dt} = -\frac{1}{\rho}\vec{\nabla}p + \nu\vec{\nabla}^2\vec{u} \tag{5.23}$$

the driving force is given by a pressure gradient ∇p. Without loss of generality, the pressure gradient can be converted in an external force K (Batchelor 1999). This so-called body or volume force has the advantage that the density of the fluid in the simulation stays (almost) constant.[2] Pressure boundary conditions lead automatically to different fluid densities since there is a linear relationship between p and ρ.

In the Q19D3 model, the body forces are included as a modification of the distributions at the fluid nodes for each time step in the form

$$\tilde{f}_i(\vec{x},t) = f_i(\vec{x},t) + \frac{1}{18c_s^2}\rho(\vec{x},t)\vec{g}\cdot\vec{e}_i \qquad i = 1,\ldots,6 \tag{5.24}$$

$$\tilde{f}_i(\vec{x},t) = f_i(\vec{x},t) + \frac{1}{36c_s^2}\rho(\vec{x},t)\vec{g}\cdot\vec{e}_i \qquad i = 7,\ldots,18 \tag{5.25}$$

where $\vec{g}$ it the acceleration vector. The factor $1/c_2^2$ is needed since the body force should lead to a momentum change of ρK (Buick 1997).

5.3 Simulations of flow in a circular pipe

As a test system for the LB simulations, we calculated the steady-state velocity field for flow in circular pipes with different diameters. The flow was driven by a body force of $g_x = 10^{-5}$. The largest simulated diameter of $d = 29$ lattice nodes was therefore due to a Reynolds number

$$Re = \frac{v \cdot d}{\nu} \tag{5.26}$$

to about 0.12 ($\nu = \frac{2\tau-1}{6} = 1/6$, $v < 0.0007$).

One simulated parabolic velocity field is illustrated in figure 5.3 together with the deviation from the theoretic velocity. Theoretically, the solution of the flow in a circular pipe leads to a parabolic velocity field in the form (Maier et al. 1996)

$$v_o(y,z) = \frac{K_x}{4\rho\nu}(r-R)^2 \tag{5.27}$$

where K_x is the driving force in x-direction.

As one can see from the residuals in the velocity, we get a very good agreement between the theoretical values and the simulation. Nevertheless, there are deviations which are caused by the underlying lattice resolution and the interaction between fluid and solid phase in the LB model (Maier et al. 1996, Mei et al. 2000). For small diameters, the main source of error is given by the approximation of curved objects on the cubic lattice as shown below in figure 5.4.

---

[2] In the simulation, the fluid is assumed to be incompressible ($\vec{\nabla}\cdot\vec{v} = 0$).

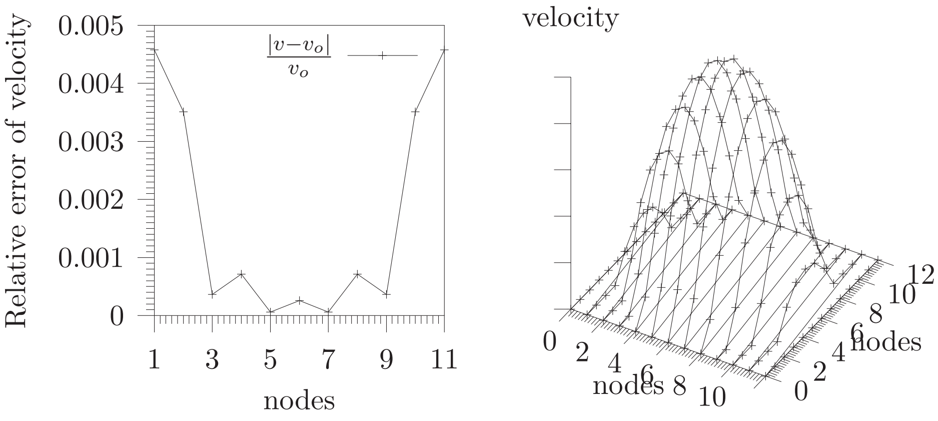

Figure 5.3: Velocity field for the simulated flow in a circular pipe with a diameter of 11 lattice nodes. The figure on the left hand side shows the relative deviation of the simulated velocity from the theoretic value (v_o) for a cross section.

5.3.1 Conversion between lattice and physical units

The simulation of the flow in a circular pipe could entirely be described with dimensionless or lattice units. We only made sure that the (dimensionless) Reynolds was small enough in order to provide a laminar flow regime. For the comparison to measured data, the lattice units have to be converted to SI units. This can be done by using the lattice spacing l_o, the conversion factor ρ_o of the density, and the conversion factor of the velocity v_o. Then, the "real" values can be determined from the lattice units as shown in table 5.1.

Parameter (SI system)	
Length l	$l = l_o \cdot l'$
Velocity v	$v = v_o \cdot v'$
Density ρ	$\rho = \rho_o \cdot \rho'$
Time t	$t = l_o / v_o \cdot t'$
Viscosity ν	$\nu = v_o \cdot l_o \cdot \nu'$
Pressure p	$p = \rho_o \cdot v_o^2 \cdot l_o \cdot p'$

Table 5.1: Conversion from lattice units to the SI system. Normally, the lattice spacing together with the density, and the viscosity of the fluid are fixed and the other parameters are converted as indicated.

5.4 Permeability and hydraulic conductivity

From the velocity field that is derived by the LB method, we determine the permeability of a given structure. The permeability, i. d. the intrinsic permeability of a porous medium is a tensor k^* which is defined through

$$\vec{v} = -\frac{\bar{\bar{k}}^*}{\mu}\vec{\nabla}p \tag{5.28}$$

where $\vec{v}$ is the average fluid velocity, μ the fluid viscosity, and $\vec{\nabla}p$ an applied pressure gradient. Equation 5.28 is called Darcy's law and is well established for the description of slow flow of incompressible fluids in heterogenous media (Torquato 2002).

From a physical point of view, the permeability is a macroscopic material parameter and its definition is strongly related to the concept of a REV which will be explained later in chapter 6.

If the permeability is well defined, we can transform the permeability tensor with respect to the principal axes. Then, we calculate the diagonal entries k^*_{ii} of the tensor by simulating a pressure gradient along the appropriate axis. For example, the permeability in x-direction is given by

$$\vec{v} = -\frac{k^*}{\mu}\frac{\partial p}{\partial x} \tag{5.29}$$

where the average velocity is defined by

$$\bar{v} = \frac{\int_A \vec{v}d\vec{n}_x}{|A|} \tag{5.30}$$

and A is a plane perpendicular to the direction of the pressure gradient and $\vec{n}_x$ the corresponding normal vector.

The permeability k^* has the dimension of m^2 and is sometimes interpreted as the effective pore channel area (Torquato 2002). k^* does not depend on the investigated fluid. Sometimes the fluid parameters are included in the definition and we get a so-called fluid conductivity

$$k' = \frac{k^*}{\mu} \tag{5.31}$$

with the dimension $\frac{m^3 \cdot s}{kg}$. Additionally, it is common to use the hydraulic head $h = p/\rho g$ instead of the pressure which leads to the conductivity

$$k = \frac{\rho g}{\mu}k^* \tag{5.32}$$

where ρ is the fluid density and g the acceleration due to gravity. If the considered fluid is water, k is called the hydraulic conductivity of the medium. In the following, we will work only with the hydraulic conductivity k with the dimension of m/s since this is the parameter that was measured experimentally.

5.4.1 Hydraulic conductivity of a circular pipe

In the case of a circular pipe, given a constant pressure gradient the hydraulic conductivity depends only on the diameter d of the pipe. One finds the proportional relation

$$k = \frac{\rho g}{32\mu} d^2 \tag{5.33}$$

Figure 5.4 shows the result of LB simulations for pipes with diameters between 1 and 29 lattice nodes.

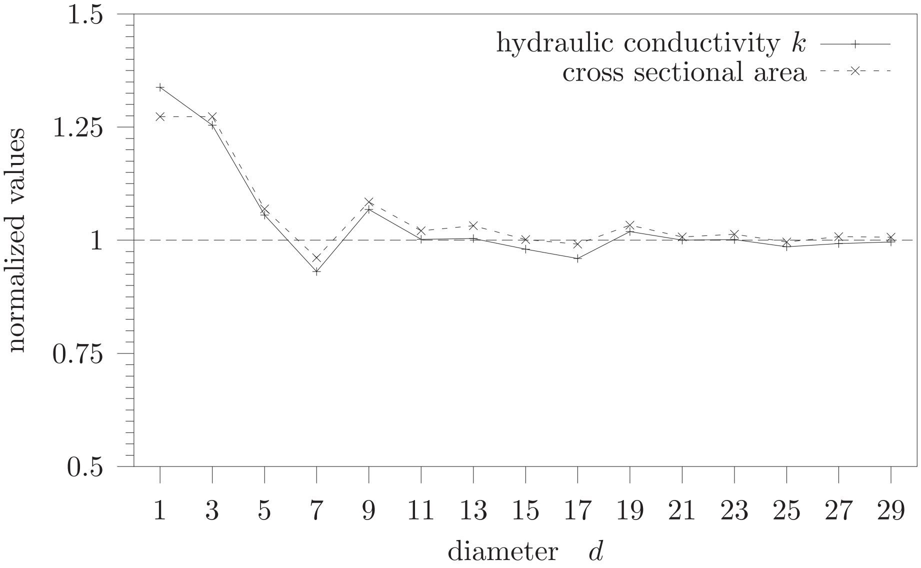

Figure 5.4: Hydraulic conductivity k of a circular pipe versus the pipe diameter. The values are normalized to the theoretic values given in equation 5.33. The dashed line shows the deviation of the cross section area from the theoretic value of $\pi(d/2)^2$ (discretization effect – compare figure 2.5).

As one can see from figure 5.4 that the determined hydraulic conductivity depends on the resolution of the lattice. For small pipe diameters, there is a large deviation between the theoretic cross sectional area of the pipe and its realization on the lattice. In general, the hydraulic conductivity follows that trend and in the worst case of a channel consisting of only one lattice node, the overestimation of the hydraulic permeability is about 35%.

5.5 Hydraulic conductivity with different BC

Bernsdorf et al. (2000) and Pan et al. (2001) showed the high accuracy of the LB method in the flow simulation with low Reynolds number. Since they where interested in the pressure field, they were working with pressure boundary conditions. But the pressure boundary conditions require the simulation of additional nodes at the inlet and the outlet of the sample. The density and therefore the pressure ($p = \rho c_s^2$) at an inlet node can be fixed to ρ_{in} by setting the distribution functions to

$$f_0 = \frac{1}{3}\rho_{in} \tag{5.34}$$

$$f_i = \frac{1}{18}\rho_{in}, \qquad i = 1, ..., 6 \tag{5.35}$$

$$f_i = \frac{1}{36}\rho_{in}, \qquad i = 7, ..., 18 \tag{5.36}$$

which leads to a velocity of zero at these pressure nodes ($\rho\vec{v} = \sum_i \vec{e}_i f_i(\vec{x}, t) = 0$). Obviously, the flow field close to the inlet and outlet will be dominated by the "zero velocity" artefacts. For the sake of completeness, we want to refer to the implementation of pressure boundary conditions in order to reduce these effects (Zou and He 1997).

In contrast to pressure BC, we used the alternative approach of a volume force as described above. We found only small deviations between the two approaches as shown in figure 5.5. In the case of a volume force, the velocity field is smoother even toward the inlet and the outlet. Nevertheless, the hydraulic conductivity which is determined by averaging over the velocity through a plane apart from the boundaries is comparable for both methods and we conclude that the error in our LB simulations is dominated by the discretization effects as shown in figure 5.4.

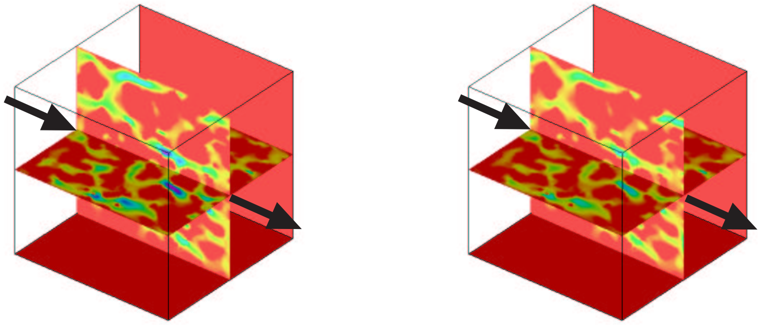

a) Pressure BC

b) Volume force

Figure 5.5: LB simulated velocity fields of flow in a complicated geometry. Shown are the absolute values of the velocity field for two cross section in flow direction. The red color indicates a velocity of zero with higher values toward blue. In figure (a), the flow is driven by pressure gradient and the velocities at the inlet and at the outlet are zero. In figure (b), the flow was driven by a volume force.

6 Analysis of the investigated structures

In this chapter, we start with a description of the investigated material and the x-ray micro tomography which gives a 3D representation of the pore geometry. Then we apply the methods described in the first part of this work in order to characterize the geometry of the structure. Finally, we calculate the saturated hydraulic conductivity and the capillary pressure-saturation curves with the models described above and compare the results to measured data.

6.1 Investigated material

In the framework of this study, we investigated a sintered borosilicate glass produced by *ROBU Glasfilter-Geräte GmbH.* Borosilicate glass consists mainly of silicon dioxide ($\sim 81\%$) and boron oxide ($\sim 13\%$) which leads to a density of about $2.2 \cdot 10^3 kg/m^3$.[1] The choice of the material was made due to its rigid structure which is due to a well defined pore space. This is also an advantage from an experimental point of view since experiments are reproducible. Additionally, x-ray tomography, our method of choice for the determination of a 3D representation of the pore space, is excellently suitable to be applied. This is due to the large difference between the absorption coefficient of air and silicon dioxide.

The sintering process provides a way of manufacturing porous glass media with different pore size distributions. For our investigations, we used two different media which will be named P250 and P100 according to the manufacturer and the ISO notation (ISO 4793) based on the nominal pore size. An overview of the the pore sizes and the porosity of the media can be found in table 6.1. The two samples used had the shape of columns with a height of about 11 cm and a diameter of 5.5 cm. For these columns, we determined the porosity by gravimetric methods.

---

[1] A further description of the physical properties of the sintered glass can be found in Graf et al. (n.d.).

	Notation	Nominal pore size (pore diameter) as indicated by the manufacturer	Porosity Φ
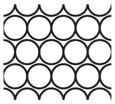	P250	160-250 μm	0.43±0.04
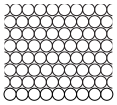	P100	40-100 μm	0.46±0.02

Table 6.1: Notation and pore size of the investigated borosilicate glass. The porosity was measured gravimetrically and the error is mainly caused by the volume measurement.

6.2 Micro tomography and 3D representation of the pore space

A high resolution x-ray scan could not be done for the entire column. This is due to the fixed relation between sample size and resolution of the scanning apparatus. As a rule of thumb, a maximum for that relation is about 1000. Therefore, we sawn off a slice of each column and prepared subsamples with volumes of $1\,\mathrm{cm}^3$ for P250 and $0.26\,\mathrm{cm}^3$ for P100.[2] The shape of the subsamples was cubic for P250 and cylindric for P100. The cylindric shape is more suitable for tomography and improves the quality of the reconstructed image.

For our investigations and simulations at the pore scale, a reliable 3D representation of the pore geometry was mandatory. Because of that demand, we ordered a tomographic scan with a cone beam together with a fully 3D reconstruction at the *Fraunhofer-Institute for Nondestructive Testing (IZFP)* at Saarbrücken. The scan resolution for P250 was $30\,\mu$m and for P100 $15\,\mu$m.

We received the 3D information from the tomographic scans as 8-bit data where a high value indicates a high x-ray absorption and vice versa.

6.2.1 Segmentation of the tomographic image

First we applied a median filter to the reconstructed tomographic data in order to eliminate scanning and reconstructing artefacts. The reconstruction artefacts are basically concentric circles around the axes of rotation and the median filter removes those extreme values without a smearing out of the image. After that, we fixed a

---

[2] A determination of the pore geometry for P16 since the pore size was in the range of the resolution of the available x-ray tomograph.

gray level threshold in order to perform a segmentation into space and solid space. The segmentation could be improved by a double threshold procedure (Vogel and Kretzschmar 1996)[3]

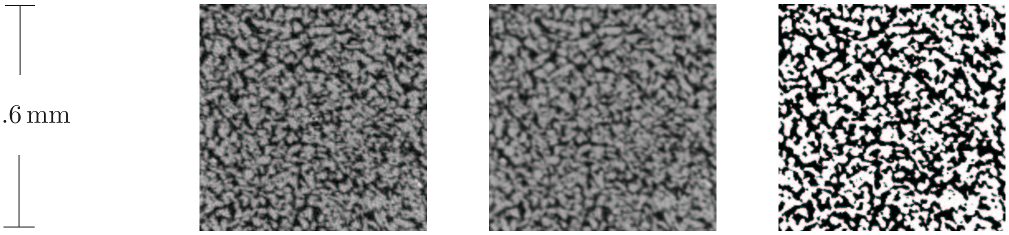

Figure 6.1: Application of a median filter and the following segmentation. Shown is a 2D slice (175×175 pixel) for the scan of P100.

The choice of the segmentation threshold was not unique. As a solution, we took the porosity as controlling parameters and forced a match between the porosity of the sample and the binarized image. Here, a problem occurred for the medium P250, since the porosity of the entire sample of 0.43 (see table 6.1) was significantly higher than that of the scanned subsample. For the subsample, we used the gravimetric and the pycnometric method to measure the porosity and determined a value of only 0.3±0.025.[4] Consequently, the structure P250 was transformed into a binary image with a porosity of 0.3 keeping in mind that there is a porosity gradient over the investigated column on a macroscopic level.

Figure 6.2: 3D visualization of the reconstructed pore geometry. On the left hand side P250 and on the right hand side P100. Both images show volumes of 120^3 voxel. Thus, the sample on the left hand side represents a volume of about 47 mm^3 and the other a volume of about 23 mm^3.

The problem of differences in the porosity for the entire sample and the scanned subsample did not occur for P100 where we measured for both samples a value of about Φ=0.46.

---

[3] For the investigated images, the bi-level approach removed only some artefacts without major changes.

[4] The deviation might be explained by the sintering process which causes a compaction of the medium on the upper and the lower end of the column where a pressure is applied in order to sinter the particles.

A visualization of the pore structure is given in figure 6.1.

6.3 Pore size distributions

The methods described in chapter 3, in order to determine the pore size distribution for the two investigated media were applied. The results are shown in figures 6.3 and 6.4.

6.3.1 P250

The values of the interception length which are shown in figures 6.3 and 6.4 were divided by 2 in order to be comparable to an equivalent pore radius. For the medium P250, we get differences between the granulometry and the interception length of the pores. Both methods give a larger pore spectrum than indicated by the manufacturer while the interception length is shifted towards smaller pore sizes. This effect can be explained as follows. The granulometry servers as a sieve which orders the pores by certain diameters. In contrast to this, the ILDF counts all chords in the pore which are smaller or equal to the diameter if the pore is spherical. A shift toward larger interception compared to the granulometry will be found if the pores deviates from a spherical shape.

6.3.2 P100

In the case of the medium P100, the agreement in the pore size distribution from the granulometry and the interception lengths is very satisfying. With the same arguments as for the medium P250, we can explain the small shift of the interception length towards smaller pore sizes.

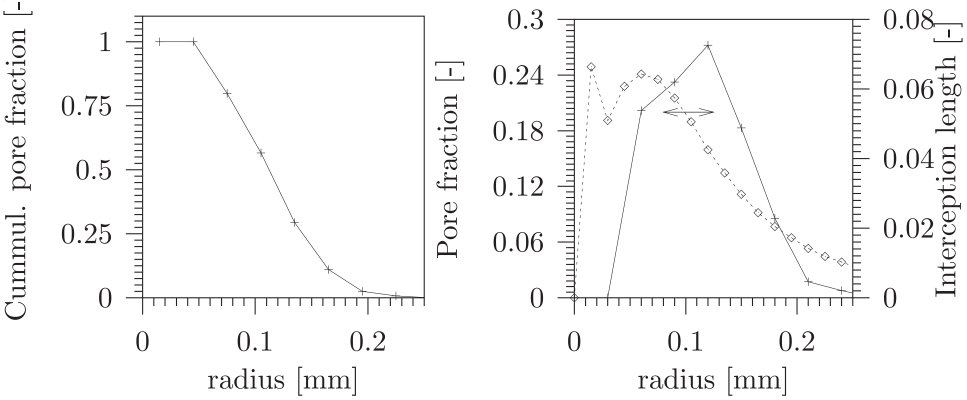

Figure 6.3: Pore size distribution of P250 as determined by morphological opening with digital spheres as SE. The plot on the left hand side is the cumulative pore spectrum. On right hand side, the pore fraction is plotted together with the interception length distribution (dashed line). The arrows indicate the values given by the manufacturer (see table 6.1).

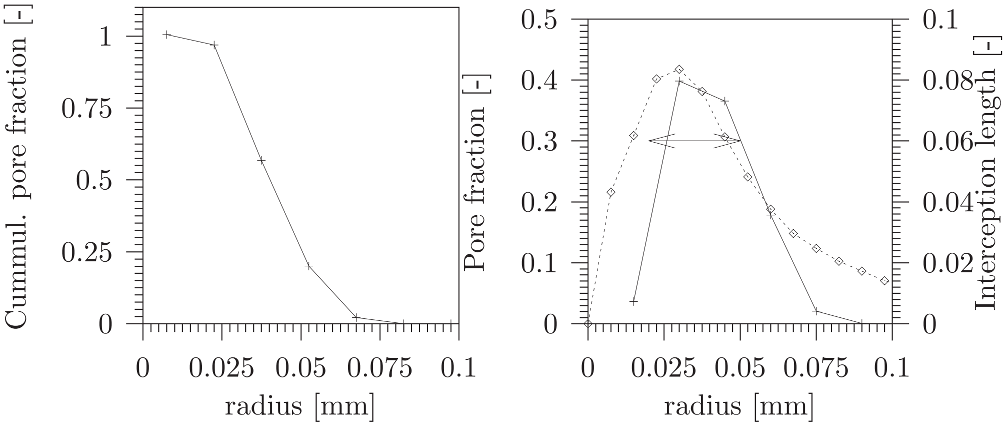

Figure 6.4: Pore size distribution of the medium P100. For details see caption of figure 6.3.

6.4 Influence of the image resolution on the pore size distribution

Since the pore size distributions are determined on a discrete lattice, we get only a few discrete classes due to the size of SE. In order to increase the number of classes, one may think to increase the image resolution by methods of digital image processing. The simplest way to increase the image resolution by a factor 2 is to double each lattice node in one of the lattice direction. In that way, the volume density of the image does not change but the steps on the surface of the objects are getting steeper. But as a consequence, the morphological processes like erosion or dilation lead to artefacts as can be seen in figure 6.5.

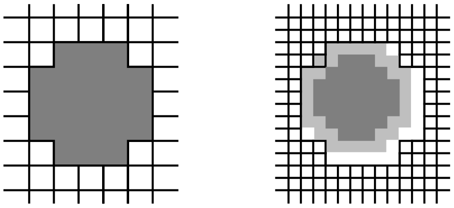

Figure 6.5: Simple grid refinement by a factor 2. The object on the left hand side has the shape of a digital disk with a diameter of 5 lattice nodes. The maximum digital disk (with odd diameter) that fits the same object on the finer lattice (right hand side) has a diameter of only 7 lattice nodes (gray area). The disk with a diameter of 9 lattice nodes (light gray) is too big

A better way to enhance the image resolution is an interpolation of the gray value image. One possibility is a so-called Shepard's interpolation. The general Shepard's interpolation calculates the unknown values f from the given values F around its neighborhood (Pang and Furman 1994) through

$$f = \begin{cases} F & \text{at data points} \\ \frac{\sum_{j=1}^{N} F_j \cdot d_j^{-\mu}}{\sum_{j=1}^{N} d_j^{-\mu}} & \text{otherwise} \end{cases} \tag{6.1}$$

where $j = 1, 2, \ldots, N$ indicate the points in the neighborhood with the distance d_j to the interpolation node. Different values of the exponent μ change the weighting of data points with the distance.

We achieved visually good results by choosing $\mu = 2$ while the interpolation was performed only over the 26 neighboring voxel. Figure 6.6 shows a cross section through the pore geometry of medium P100 with the original resolution and after a Shepard interpolation of a factor 2. Since the Shepard interpolation was done on the gray scale image, we trimmed the threshold for the segmentation in order to get

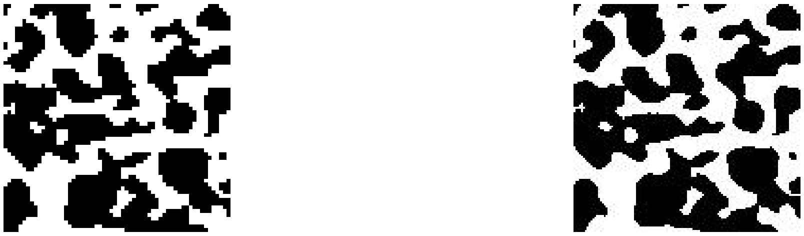

Figure 6.6: Cross section through the pore geometry of the medium P100. The image on the right hand side is a refinement due to a Shepard interpolation.

similar porosities for both the original and the refined image. In the example shown in figure 6.6, the porosity differs only about 0.5%.

Due to the refinement, we get a better resolution of the pore size distribution. As one can see from figure 6.7, the Shepard interpolation only leads to a smoothing of the curve while the overall properties remain constant. For the refined image, the largest sphere that fits the image has a diameter of 10 voxel and – for computational efficiency – it is useful to work with the modified spheres as SE as explained in chapter 3. As stated earlier, we obtain only small differences between the results of digital spheres and modified spheres (figure 6.7).

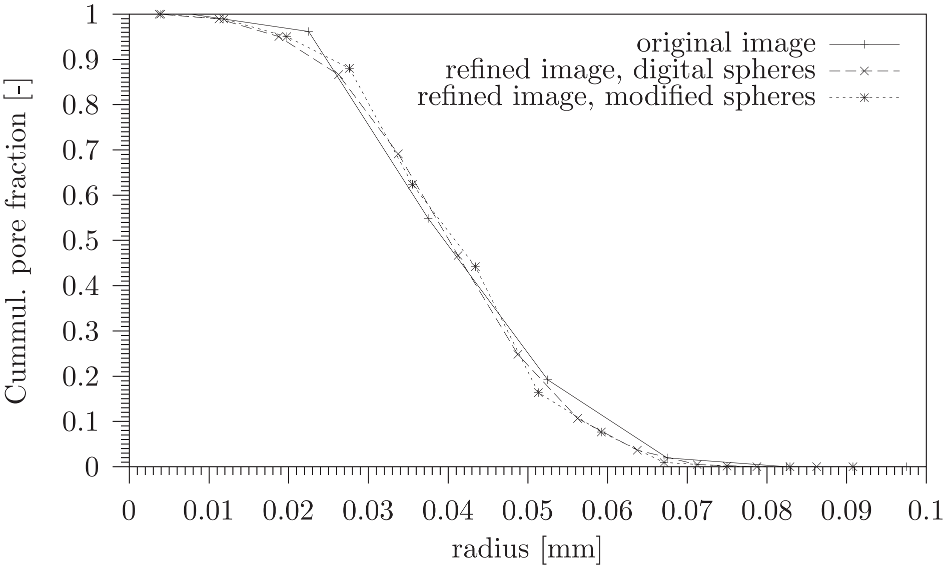

Figure 6.7: Cumulative pore fraction of the original image (bold line) and the refined image. The figure shows that we get only minor differences between the morphological operations with digital spheres and modified spheres. The computation with modified spheres however is much faster as explained in chapter 3.

6.5 Physical parameters at the microscopic and the macroscopic scale

In this section, we are interested in the determination of the hydraulic conductivity of the investigated samples as an *effective* material property. This step is not trivial, since it includes a scale transition or upscaling from the microscale to a macroscopic or continuum scale[5]. As noted already in the introduction to this thesis, the scale transition is fundamental for the scope of this work and will be outlined in the following.

6.5.1 Characteristic function

Up to now, the sintered glass samples were investigated only on a microscopic scale. On that scale, we worked with a binary representation of the pore geometry and we can formally use a characteristic function χ_Ω of the form

$$\chi_\Omega(\vec{x}) = \begin{cases} 0; & \vec{x} \in \Omega \\ 1; & \vec{x} \notin \Omega \end{cases} \tag{6.2}$$

similar to the definition of a binary image in equation 2.6. Up to now, the characteristic function was only defined for the solid phase of the material but implicitly we assumed that the pore space was air filled. In this sense, the characteristic functions for the solid phase χ_s and the air phase χ_a are complementary to each other. This formalism can be expanded to situations where the pore space is filled with different fluids. Thus, we still use the characteristic function in order to describe the distribution of each phase.

6.5.2 Averaging

With increasing sample size, the description based on characteristic functions is no longer feasible. This is due to the limits in the determination of the pore geometry by x-ray tomography or other measurements. Not to mention the capacity that is needed to store the data. Therefore, it is required to work with macroscopic properties which are the result of an averaging over a certain volume. In the following, we take the porosity as an example in order to explain the averaging procedure. The porosity of a sample in a cube with side length l and the volume $V = l^3$ is defined as:

$$\phi = \frac{1}{l^3} \int_V \chi_a dV \tag{6.3}$$

---

[5] The term "continuum scale" is used due to a description where each point x of the material is assigned to a continuous parameter like the volume density.

where we used the characteristic function of the air phase. In the limit $l \rightarrow 0$, we recover the microscopic porosity

$$\phi_{micro}(\vec{x}) = \chi_a(\vec{x}) \tag{6.4}$$

Thus, $\phi_{micro}(\vec{x})$ is a discontinuous function which strongly depends on the position $\vec{x}$.

With increasing sample size, the property ϕ is an average over solid and pore space and has a value between 0 and 1. For many structures with practical applications, the variations of ϕ decrease rapidly with increasing volume (Torquato 2002). If this is the case, we can use a ϵ criterion in order to define the bulk or effective porosity.

6.5.3 Definition of effective properties and the representative elementary volume

Let $\phi(l)$ be a physical property as a result of an averaging over the volume l^3. We call ϕ the effective property of the material if for any given ϵ we can find l_o so that

$$|\phi(l) - \phi| < \epsilon \qquad \forall \quad l \geq l_o(\epsilon) \tag{6.5}$$

$V_o(\epsilon) = l_o^3(\epsilon)$ then defines the corresponding representative elementary volume (REV). Thus, the REV can be seen as a minimum volume that is necessary so that the macroscopic variable no longer depends on the averaging volume (Bear 1972).

The definition of the effective property was shown using the example of the porosity, but also holds true for other physical parameters. Two details are of importance in this context. First, the averaging which was given by the arithmetic mean (equation 6.3) can be much more complicated for other properties like the hydraulic conductivity. Secondly, we have to point out that different properties are connected to different REVs, an issue we will come back to in chapter 7.

Additionally, it should be stated that averaging can always be used for the calculation of a macroscopic property. We only call it an effective material property, however, if a REV exists and the averaging volume is large enough. The entire process is then called homogenization (Torquato 2002).

6.5.4 Materials with discrete hierarchy

The definition of the effective property (equation 6.5) implies that the structure is homogenous with respect to a length scale larger than l_o. In reality, one often finds that there is an upper limit for a homogeneous volume. The situation is illustrated in figure 6.8.

In the simplest case, the physical property can be defined separately in all regions (e. g. Ω_1, Ω_2, and Ω_3) with a modified ϵ criterion:

$$|\phi(l) - \phi| < \epsilon \qquad \forall \quad l \geq l_o(\epsilon) \quad \text{and} \quad V(l) \subset \Omega \tag{6.6}$$

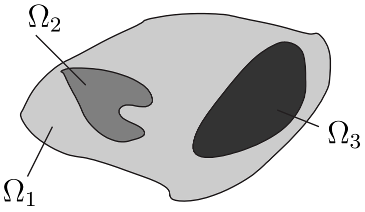

Figure 6.8: Illustration of a medium with discrete hierarchy.

I. e. the averaging volume $V(l)$ lies entirely in the region Ω. Materials where effective properties differ from one region to another are called discrete hierarchic. Later in this chapter, we use the concept of discrete hierarchy in order to model the effective hydraulic conductivity of the investigated medium P250.

Obviously, the determination of the effective property of the region Ω is difficult if the volume $V(\Omega)$ is smaller than the volume V_o of the REV. We will come back to that problem later in chapter 7.

6.6 REV with respect to hydraulic conductivity

In the search of a REV with regard to the hydraulic conductivity, we calculated k for binary pore geometry at different image sizes. For the flow simulations, we used the lattice-Boltzmann model as described in chapter 5. The results are shown in figures 6.9 and 6.10

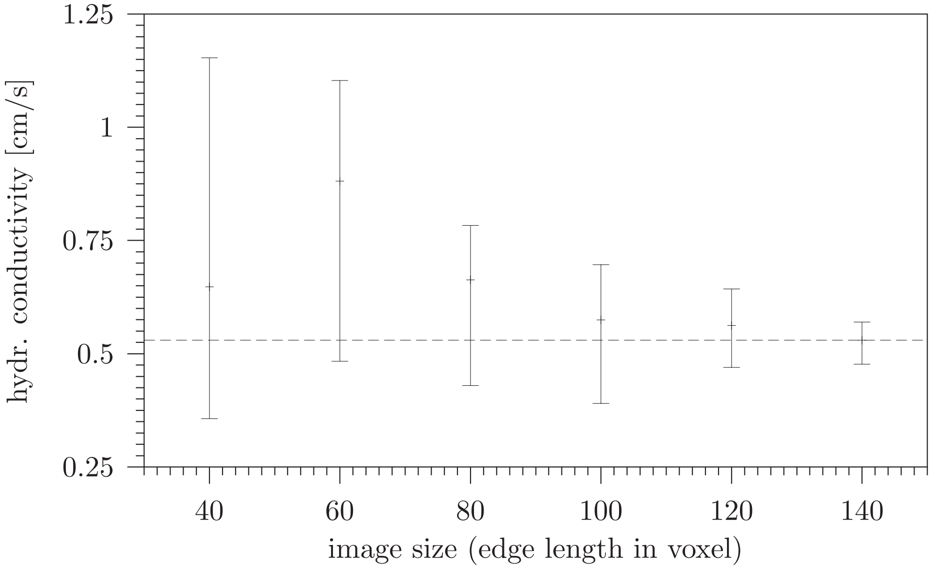

Figure 6.9: The hydraulic conductivity K versus the image size for the medium P250. The error bars are due to the range of K in the three different flow directions.

In general, the hydraulic conductivity is a tensor and we calculated three components k_x, k_y, and k_z where the driving force acts along the x-, y-, and z-axis, respectively. For the method of homogenization, the results of figure 6.9 are very promising. First of all, the hydraulic conductivity has a clear trend to a value around 0.6 cm/s with increasing image size. Additionally, the differences between the three calculated flow directions are getting smaller with larger sample sizes. This can be interpreted as a strong evidence that the hydraulic conductivity is isotropic and we can write the conductivity tensor in the simple form of $\bar{\bar{k}} = \bar{\bar{1}}k$ where $\bar{\bar{1}}$ is the unity tensor. By calculating k only for three (perpendicular) directions, we did not obtain an information about the off-diagonal terms of the conductivity tensor. But we assume that due to the isotropy of the material, these terms are small enough to be neglected. For the medium P100 where the pore sizes are smaller by a factor 3 to 4 compared to P250, we get very similar results for the hydraulic permeability with respect to the sample size.

Figure 6.10 shows that the permeability converges towards a defined value and the deviations over the three flow directions are getting smaller with greater image size. Therefore, we conclude that we can also define a REV with respect to the hydraulic

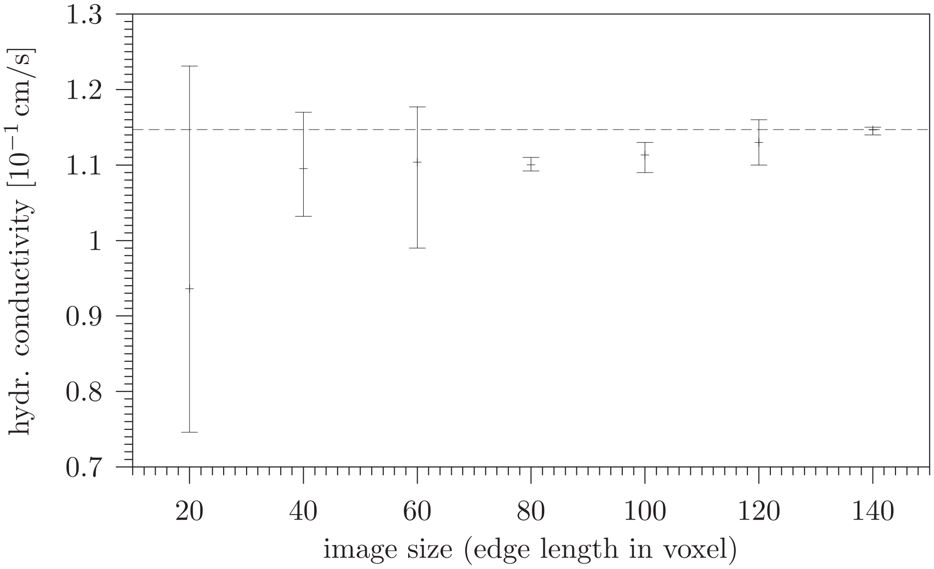

Figure 6.10: Hydraulic conductivity k versus the image size for the medium P100. The error bars are due to the range of k over the three different flow directions.

conductivity for the medium P100.

6.7 Simulated hydraulic conductivity compared to measurements

Since we have a strong evidence that we can use the concept of homogenization for the hydraulic conductivity from the micro scale to the continuum scale, we compare the simulation to measured data. The measurement was done using the falling head method.

6.7.1 Falling head method

For the measurement using the falling head method, the column sample was placed in a plastic tube in a way to avoid a by-pass of the sample. The sample was ponded with water which was allowed to drain freely due to gravity. One can show that the height of the water level $h(t)$ decreases exponentially with time until it reaches the surface of the sample (Klute and Dirksen 1986):

$$h(t) = h_o e^{-\frac{Kt}{L}} \tag{6.7}$$

where h_o is the initial height of the water level and L the height of the sample as shown in figure 6.11. The hydraulic conductivity can be deduced as the slope by plotting $\log(h(t)/h_o)$ versus time. In order to get a good time resolution, we used a pressure sensor to automatize the measurement of $h(t)$ (figure 6.11).

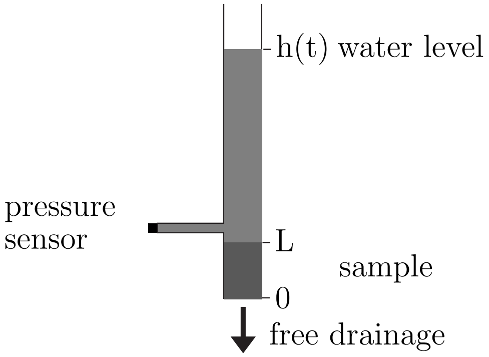

Figure 6.11: Overview for the falling head permeameter. The height of the water level can be measured by a pressure sensor above the sample.

There are two main sources of error which influence the results of the falling head measurements. The method is sensitive to gaps between the tube and the sample, so that water which by-passes the sample leads to an apparently higher hydraulic conductivity. On the other hand, the measured hydraulic conductivity will be smaller if the pore space of the sample is not entirely filled with water. We reduced the influence of the first effect by placing the sample closely in the tube. Additionally, before the measurement, the sample was saturated over several hours under a pressure of about 200 cm H_2O.

With the falling head permeameter, we could measure the hydraulic conductivity for both sintered glass columns with an error of about one order of magnitude. The results are plotted in figure 6.14.

6.7.2 Simulated and measured hydraulic conductivity of P250

As mentioned above, the scanned subsample and the entire column of the medium P250 differed significantly in the porosity. Since the subsample was sawn off at one end of the column, that difference can only explained by assuming a gradient in porosity over the column. Therefore we used a x-ray tomograph to get an estimation of the porosity over the height of the sample. From tomographic information, we derived a porosity distribution over the sample as shown in figure 6.12.

A problem with the model with different porosities is that there was only information available about the pore geometry in the region with $\phi = 0.30$. In order to overcome that lack of information, we used different thresholds in the segmentation procedure and mimicked samples of different porosities. The result is shown for a 2D slice in figure 6.13. For each porosity we determined the hydraulic conductivity by LB simulations.

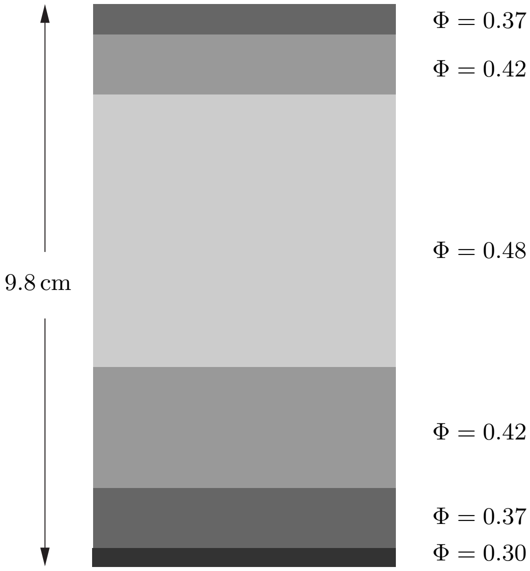

Figure 6.12: Model for the porosity distribution of the column sample of medium P250.

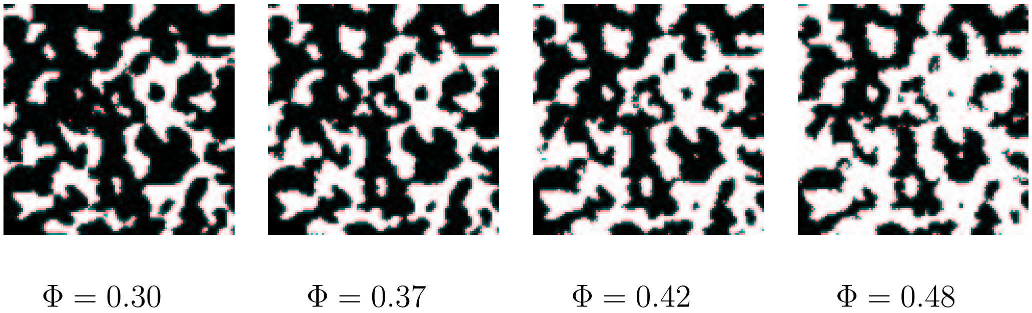

Figure 6.13: 2D slices of the binary image with different thresholds for the segmentation. This leads to porosities between 0.30 and 0.48.

Then the (simulated) hydraulic conductivity for the entire column is given by

$$k = h \frac{1}{\sum \frac{h_i}{k_i}} \tag{6.8}$$

where h is the height of the column. h_i and k_i are the height and hydraulic conductivity of the i-th region according to figure 6.12.

Comparing the results of the hydraulic conductivity as derived by the simulation and the measurements, we find that we overestimate the measured value by a factor of about 2 to 3 (figure 6.14). We see this as a good result since we used only a very rough method to model pore spaces with different porosities.

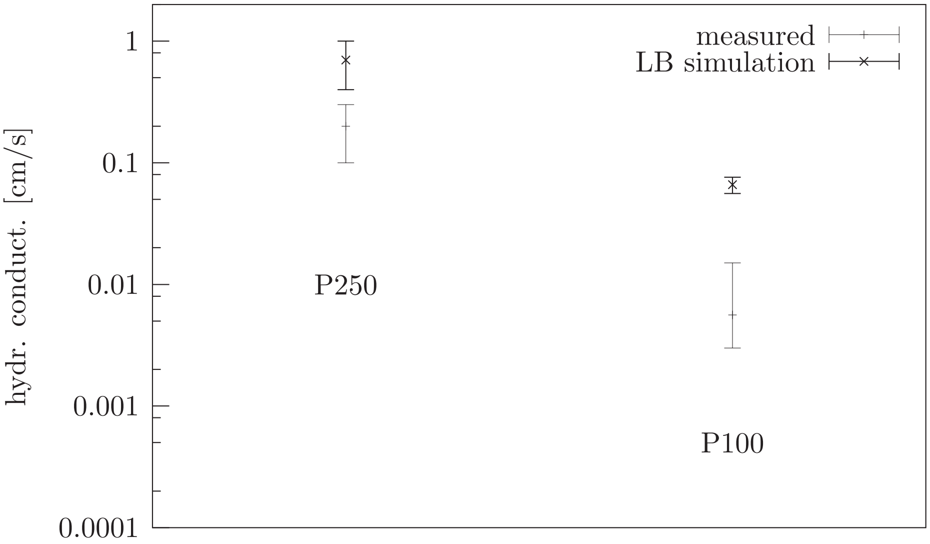

Figure 6.14: Measured and simulated hydraulic conductivities of the two investigated media.

6.7.3 Simulated and measured hydraulic conductivity of P100

In the case of the medium P100, we could directly compare the measured hydraulic conductivity with the simulated one. In addition to the values shown in 6.10, we determined k for a two times finer grid resolution which reduced the simulated values by about 30%. This is in agreement with the results for the flow simulations in capillary tubes discussed in chapter 5 and other studies (Manwart et al. 2002).

As one can see from figure 6.14 that the simulated hydraulic conductivity is about 6 times higher than measured. The error in the simulation is mainly due to the uncertainty of the porosity. For an estimate of the error we used porosities of 0.44 and 0.48 for the medium P100 and determined the respective values of k.

Since our simulations are based only on data of the pore geometry, the observed deviation from the measured value is still acceptable. On the experimental side, a not completely saturated sample would explain the “too small” measured hydraulic conductivity.

6.7.4 Comparison to related studies

Up to now, only few studies about flow simulations on a micro scale in comparison to measurements have been published. Manwart et al. (2002) performed flow simulations on the measured pore geometry of a Fontainebleau sandstone with both a LB and finite-difference scheme. Their results are very similar to our conclusions. Depending on the resolution of the microstructure, the boundary conditions, and the numerical method they achieved a rather good agreement between the simulations and the measured values while deviations up to 100 % could not be excluded. Therefore, we conclude that there is still room for improvements on both sides, the experiments and the simulations.

6.8 Pressure saturation relations

In this section we present results from the application of the pore morphology based (PMB) model as described in chapter 4 to the two investigated media. These results will then be compared to experimental data.

6.8.1 REV with respect to the pressure saturation curve

Since we want to derive the macroscopic pressure saturation relation (P^c-S^w) from simulations on a microscale, we run into the same problems as for the hydraulic conductivity. Again, the P^c-S^w curve is a well defined quantity only if there exists an appropriate REV. In a first step, we used the PMB model which has been introduced in chapter 4 in order to examine the dependence of the P^c-S^w curve on the image size.

In the PMB model, we determine the portion of the pore space that gets filled with air for a given capillary pressure by two criteria. The pore space has to be larger than a sphere according to the Laplace equation. Additionally, the water drains off the pore space only if there is a connection to the air reservoir.

The main pressure steps in the simulated drainage of P100 are shown in figure 6.15. From the pore size distribution which has been shown at the beginning of this chapter, we assumed that the drainage of the medium P100 takes place in relatively small pressure range. Therefore, we worked with the Shepard interpolated images in order to increase the resolution of the determined P^c-S^w curve. For the investigations about the existence of a REV, we had to calculate several pressure-saturation curves. Therefore, we used the fast algorithm based on the modified spheres.

According to figure 6.15, we expect a more and more rigid air entry pressure with increasing image size. The steps marked as (a) and (b) in figure 6.15 can be interpreted as boundary effects since the plotted pore space gets only air filled because - by chance - there is a connection to the air reservoir on the upper end of the sample. Only in the third step (c), when the (under)pressure is higher than 40 cm H_2O, a connected network of pores is drained. Since the influence of these boundary effects depend on the relation between volume and surface of the sample, we expect them to be reduced by increasing image size. The simulations shown in figures 6.16 and 6.17 justified these presumptions. Additionally, we found that the variations of the pressure-saturation curve become smaller and smaller with increasing image size. This allows us to define a REV with respect to the P^c-S^w curve for both media. The minimum image size for medium P250 is about 140^3 voxel and for the medium P100 about 100^3 voxel.

In the PMB model we distinguish between 6 different directions depending on which side connects to the air reservoir (the opposite side is then connected to the water reservoir). If the boundaries had a strong impact on the P^c-S^w curve or

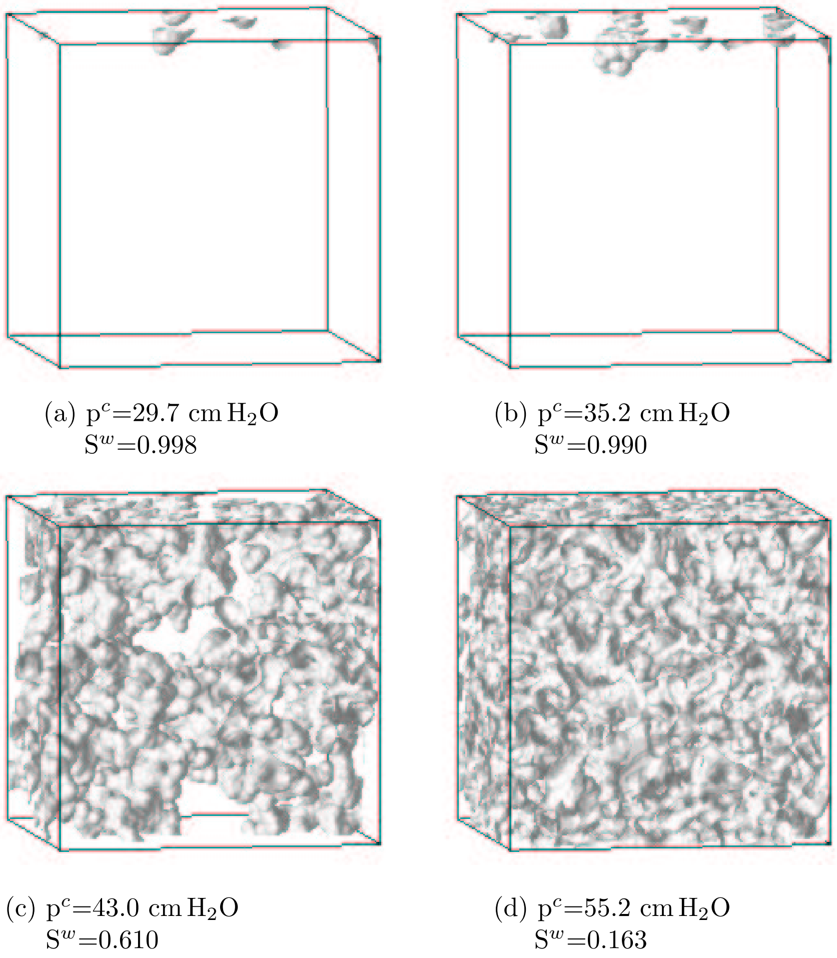
(a) p^c=29.7 cm H_2O
S^w=0.998

(b) p^c=35.2 cm H_2O
S^w=0.990

(c) p^c=43.0 cm H_2O
S^w=0.610

(d) p^c=55.2 cm H_2O
S^w=0.163

Figure 6.15: Simulated drainage of P100. Shown are only iso surfaces of the air distribution. The water drains through the plane on the bottom while the air enters the sample through the upper plane. All other sides can be seen as closed.

the medium were anisotropic, this would lead to "direction dependent" pressure-saturation curves. Fortunately, we could show that for image sizes larger than the determined REV, the simulated P^c-S^w curves were independent of the direction, i. e. the position of the air reservoir.

It is remarkable that the size of the REV with respect to the pressure-saturation is comparable to that for the hydraulic conductivity. Our explanation for that is their strong dependency on the underlying geometry and will be carried out in chapter 7.

6.8.2 Differences at low saturations for both media

The simulated pressure saturation curves of the two investigated media differ significantly at low saturations. While the medium P100 shows a smooth desaturation

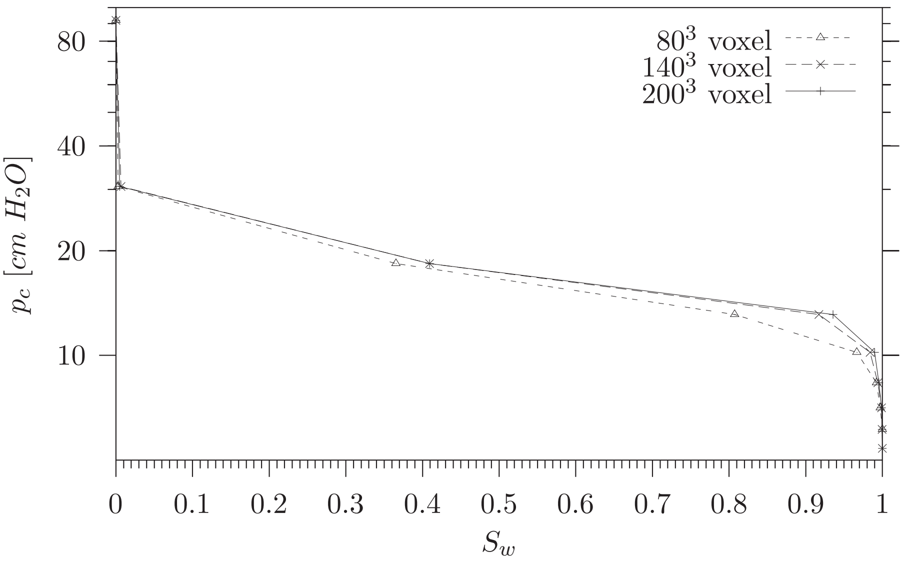

Figure 6.16: Pressure-saturation curves of the sample P250 with different image sizes as determined by the PMB model. The determined saturation are a mean values over the 6 simulated directions.

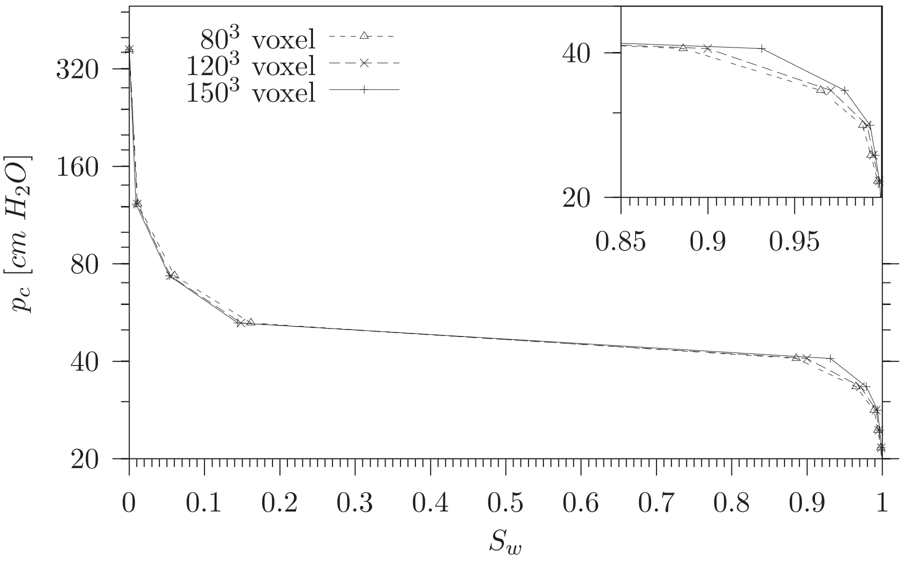

Figure 6.17: Pressure-saturation curves of the sample P100 with different image sizes as determined by the PMB model. The determined saturation are a mean values over the 6 simulated directions. The subplot shows in detail the decline of the boundary effects - details see text.

over several pressure steps between 50 and 330 cm H_2O, this region is more discontinuous for medium P250 (figure 6.16). This can be explained by looking at the cumulative pore size distribution of both samples (see figures 6.3 and 6.4). With the morphological opening, we determined almost no pores in the medium P250 with diameters smaller than 3 voxel[6]. Additionally, the pores are highly connected and the calculated points at low saturation reflect only the pore space with the according pore diameter. This can be seen more clearly in figures 6.18 and 6.19, where the results are compared to a model of a bundle of capillary tubes.

---

[6] 3 voxel was the diameter of the smallest digital sphere that was used as SE.

6.8.3 Simulated and measured pressure-saturation relations

In the previous section, we defined a REV for both investigated media with respect to the pressure-saturation relation. We are therefore allowed to compare simulation results from the pore scale with experimental data from the macro scale.

6.8.3.1 P250

For the calculation of the hydraulic conductivity of the medium P250, we used a discrete hierarchy to describe the medium. Consequently, we have to determine the pressure-saturation curves for all regions which differ in their porosities. Not surprisingly, the P^c-S^w curve strongly depends on the porosity of the image as shown in figure 6.18 since a larger porosity involves larger pores diameter and a higher connectivity.

Therefore, the portion of the pore space that drains at a given pressure increases with increasing porosity and the curve itself gets more and more “flat”. Figure 6.18 shows also results for a bundle of capillary tubes. In that case we decompose the pore space into a bundle of capillary tubes which lie straight between the water and the air reservoir. In other words, this is just a reinterpretation of the cumulative pore size distribution (see figure 6.3) where the radius of the pores is attributed to a capillary pressure using the Laplace law. In this context, the capillary bundle model can be seen as a lower limit for the capillary-pressure relation as long as the pore

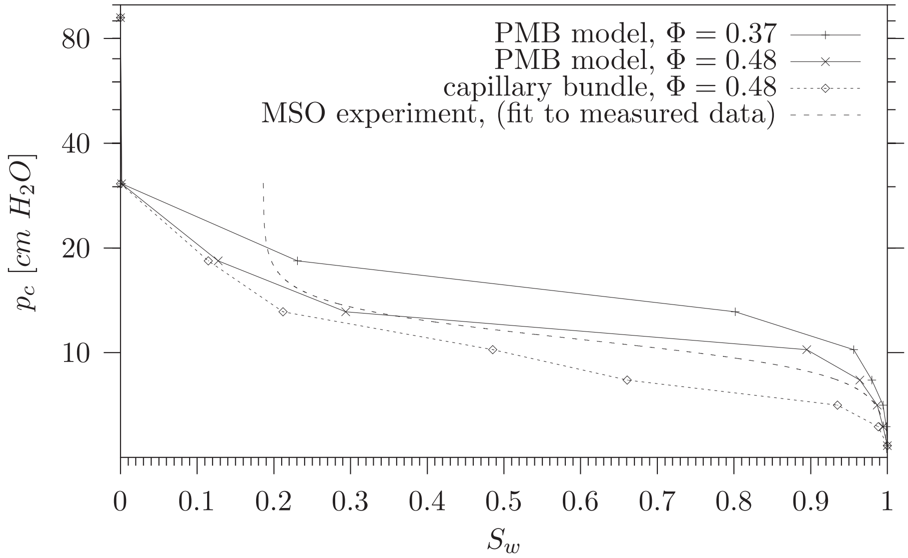

Figure 6.18: Pressure-saturation curve of P250 as determined by the PMB model with different porosities compared to a model of a capillary bundle and measured data.

space can be approximated by spheres.[7]

6.8.3.2 P100

The medium P100 shows only marginal changes in the pressure-saturation curve for different porosities. In figure 6.19, we plotted the results of the PMB simulation together with the model of capillary tubes. Both results are based on porosities of $\Phi = 0.48$ while a lower porosity down to 0.44 moves the curves slightly to higher capillary pressures. Figure 6.19 also shows measured data, i. e. a van Genuchten fit to outflow data as described in the next section. The deviation between the PMB simulation and the experimental data is obvious and will discussed later in this chapter. But first, we give a short description of the experimental setup which produced the results of figure 6.19.

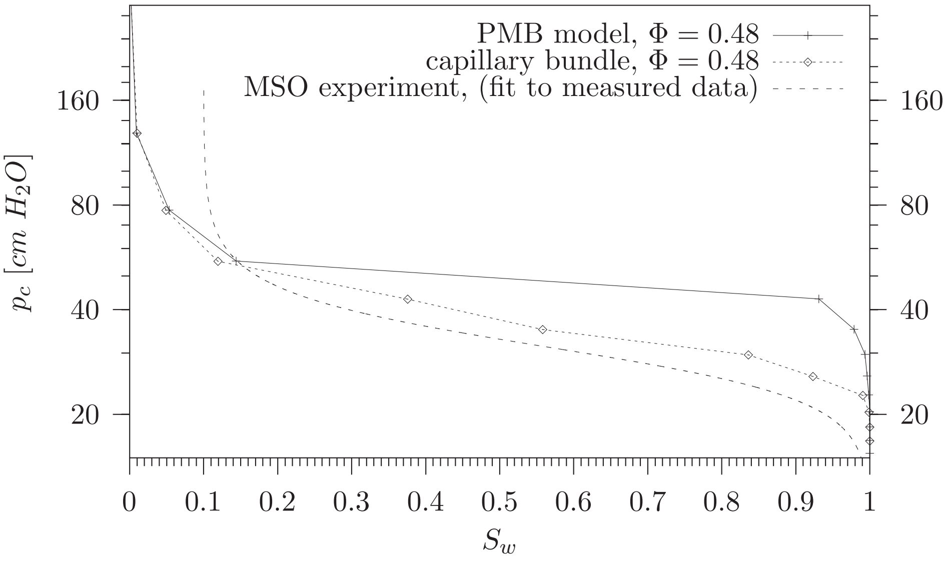

Figure 6.19: Pressure-saturation curve of P100 as determined by the PMB model compared to a model of a capillary bundle and measured data.

6.8.4 Measurement of the P^c-S^w curve

The measurement of the pressure-saturation curve was determined in a multi-step outflow (MSO) experiment by H. Graf (Graf et al. n.d.). The principle of the measurement is as follows. In the beginning, the sample is fully saturated with deionized water and placed on a filter plate which is also completely saturated. The plate is connected to a measurement device which allows a lowering of the pressure in the water phase in different steps and the measuring of the cumulative water outflow.

---

[7] This consideration is closely related to the limitations of the PMB model as discussed in chapter 4.

The determination of the pressure-saturation curve from the experimental data involves an inverse fitting procedure. A typical approach is a parameterization of the hydraulic material properties, especially the P^c-S^w curve and the relative hydraulic conductivity (van Genuchten 1980, Mualem 1976). Then, it is assumed that the outflow process can be described by the Richards equation (Richards 1931) and the parameters are determined by an inverse fit to the outflow data.

The Richards equation can only be seen as an approximation to the physical process since it assumes that the air in the system has no limitation in its mobility.

Nevertheless, for the sintered glass columns, that approach led to reliable fits to the outflow curves with the parameters given in table 6.2 and the van Genuchten parameterization

$$P^c(S) = \alpha^{-1}[S^{-n/(n-1)} - 1]^{1/n} \tag{6.9}$$

where the saturation S is given by

$$S = \frac{\theta - \theta_r}{\theta_s - \theta_r} \tag{6.10}$$

θ is the water content and the indices s and r stand for “saturated” and “residual”, respectively. Since, we are only interested in the so-called primary drainage curve, where the medium is completely saturated in the beginning, the saturated water content is equal to the porosity of the sample.

medium	α [cm H_2O^{-1}]	n	θ_s	θ_r
P250	0.0929	9.12	0.43	0.08
P100	0.0331	5.92	0.46	0.05

Table 6.2: Van Genuchten parameters of the two investigated samples according to MSO experiments.

6.8.5 Discussion of the simulated and the measured P^c-S^w curves

For both investigated samples, capillary pressure in the simulation is higher than determined by the experiments.

6.8.5.1 P250

In the case of P250, the deviation might be explained by the bias of the pore-morphology-based model. As described before, in the PMB model we assume that the interfaces between the water and air are always spherical. This leads to a bias in the P^c-S^w curve and we suppose that the overestimation of the capillary pressure might go up to 20 %. The exact quality of the PMB model could only be checked by comparing it to other methods like two-phase lattice-Boltzmann simulations.

6.8.5.2 P100

For the medium P100, the simulated values are about 30 % higher than the measured data but two major differences are obvious compared to the results for P250. First, due to the narrower pore size distribution, the simulation shows a pronounced air entry pressure of about 38 cm H_2O. This cannot be reproduced by the experiment since the van Genuchten parameterization was used to fit the experimental outflow data.

Secondly, the measured pressure-saturation curve is below the results from the bundle of capillary tubes. This can only happen for structures where spheres are a poor approximation to the pore space. As pointed out earlier in this work (see chapter 3), the granulometry leads to results with a bias in those cases. This is not the case for the medium P100 as we have shown by the comparison of the granulometry with the interception length distribution. Additionally, a shift to larger pores - which would lead to a shift of the P^c-S^w curve towards smaller pressures - would give even higher values for the hydraulic conductivity. Since the simulated hydraulic conductivity was already higher than the measured values, we excluded that explanation for the overestimation of the pressure-saturation relation.

But one possible explanation remains. In all simulations, we assumed a zero contact angle, due to the material property given by the manufacturer of the sintered glass media. Assuming a non-zero contact angle θ we can make a simple correction that scales the corresponding capillary pressure by a factor $\cos(\theta)$.[8] Since both media, P250 and P100, consist of the same material it is very likely that they have a similar (non-zero) contact angle. To address this issue, we conducted an independent experiment in order to measure the contact angle.

6.8.5.3 Measurement of the contact angle

We used a tensiometry method were the sample is brought into contact with the water and the force of the surface tension is measured over a balance. At the largest possible elevation, before water and the sample loose contact, the balance of forces is given by

$$\gamma L \cos\theta = mg \tag{6.11}$$

---

[8] A non-zero contact angle changes also the shape of pressure-saturation curve since it influences the entire flow regime and not only the quasi static state. But its full impact can only be estimated by two-phase flow simulations

where γ is the surface tension of water, m the mass of the elevated water, g the acceleration due to gravity, and L the effective perimeter. Equation 6.11 allows a direct determination of the contact angle θ if L of the sample is known. Therefore, we made the assumption that $L = 2\pi r\phi$ where r is the sample radius and ϕ the average porosity. Under these assumptions, all measurements at the medium P100 were consistent with a contact angle $\theta < 30^o$.

These result should not be overestimated due to the principal problem of the tensiometer method for porous media (unknown effective perimeter) and further, more sophisticated measurements are needed.

Additionally, it is not clear that a parameter such as the contact angle is constant over the entire sample. It might variate with changes of the surface properties which could be caused for example by a contamination during the experiment.

6.8.5.4 Possible sources of error

Summarizing, there are still three sources of error which might explain the deviation between the measurement and the simulated data:

- inhomogeneities in the porosity on the macroscale (more severe for P250)
- bias of the PMB model
- insufficient information about the contact angle.

7 Concept for the reconstruction of porous media

In this chapter, we give the motivation and the basic ideas behind the reconstruction of porous media which will be presented in the next chapter. Since the underlying concept is of fundamental use, we reserved an entire chapter for that topic.

7.1 REV and geometry information

In the previous chapter, we compared hydraulic parameters determined on the pore scale with measured values on a larger scale. For that comparison, the concept of a REV was fundamental.

In that sense, the hydraulic conductivity and the pressure-saturation relation are handy parameters since they are attributed to a “relatively” small sized REV- at least for random heterogenous media. The REV of other physical properties of the medium, e. g. solute transport, can easily be much larger. In the worst case, the necessary REV is larger than the entire pore volume that can be determined by tomography or other image forming techniques.

A way to overcome that problem is to investigate the “geometry” of the pore structure. Since our physical parameters of interest are directly related to the pore and solid geometry, we can base all simulations on the geometry of the pore space only. As we will show below, the representative volume that contains all information about the geometry of the structure is in general smaller than the REV of the physical properties. Figure 7.1 illustrates how the different REVs can be organized.

7.2 Characterization of the geometry of a structure

So far we did not specify what we exactly mean by “geometry” of the pore space. If we want to give a full description of the pore geometry, we need an index function which tells us if the space at a given position is attributed to pore or solid region (see 2.6). Obviously this description is high dimensional. For example, a binary image can have 2^n different configurations where n is the number of voxel. Therefore, it is necessary to use more compact methods in order to describe the complicated pore

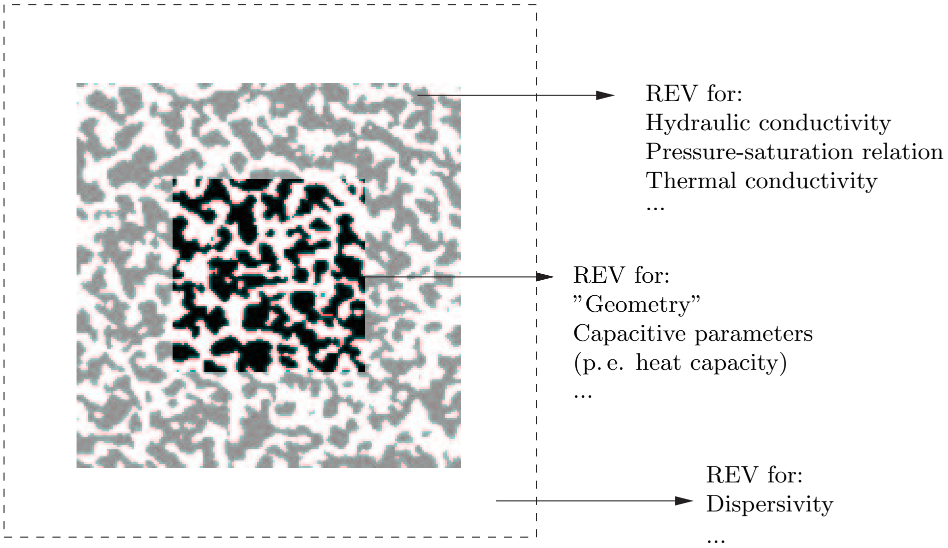

Figure 7.1: Sketch of hierarchically ordered REVs in a complicated structure. The REV for physical properties like the dispersivity may require image sizes larger than measurable. This is illustrated by the dashed box.

space which we will call "geometry" of the structure.

7.2.1 Two-point correlation functions

A classical approach in this field is a statistical analysis like a n-point correlation functions coming from statistical mechanics (Torquato 2002). The n-point correlation function describes the probability of finding n particles in a distance r from a given point. A problem in this context is that the calculation of higher order correlations is very time consuming and one needs a large amount of experimental data. Therefore, in practice the analysis is often limited to two-point correlation functions. For a digitized image, the two-point correlation function gives the probability that two voxel with a distance $|\vec{R}|$ both belong to the solid space

$$g(\vec{r}) = \alpha \langle n(\vec{R}) n(\vec{R} + \vec{r}) \rangle \tag{7.1}$$

where α is used for normalization. We chose $\alpha = 1/\Phi$ so that $g(0)$ is the porosity of the medium.

For illustration purpose, we calculated the two-point correlation of the investigated medium P100 for different image sizes as shown in figure 7.2. As one can see from figure 7.2, the two-point correlation function gives only limited information about the pore geometry. In agreement with the pore size distribution presented in figure 6.4, the two-point correlation varies only for distances smaller than 0.1 mm. At larger distances there is a constant probability of finding a solid voxel at the distance R. Additionally, variations with increasing image size are rather small.

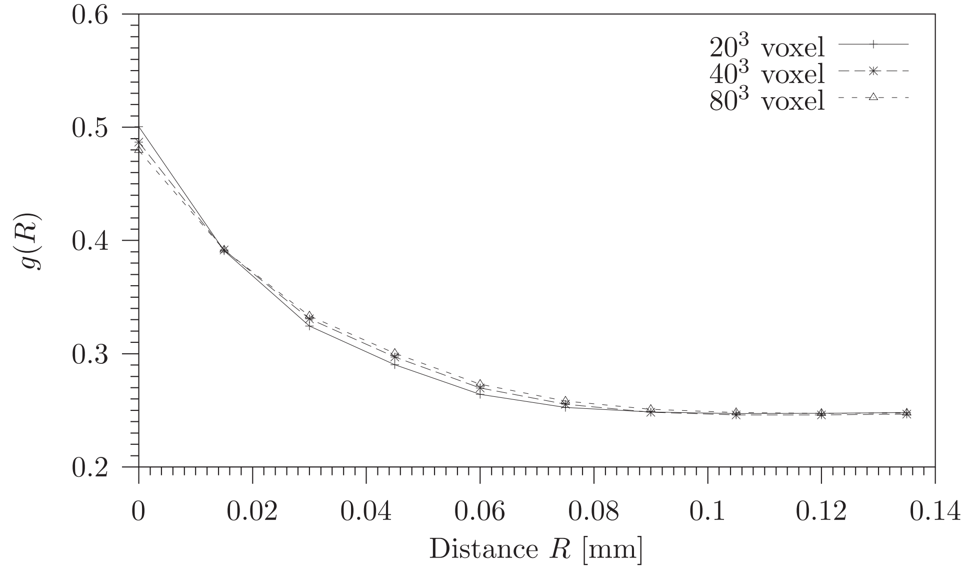

Figure 7.2: Two-point correlation function for different image sizes of medium P100.

7.2.2 Minkowski functionals

Another approach in order to describe the pore geometry with a small set of parameters has been developed recently and is based on the Minkowski functionals (Mecke 2000). As pointed out in chapter 2, the MF are *integrated* parameters for geometric objects. Therefore, one may assume that in general the variations of the geometry are also reflected in the MF.[1] Consequently, we determined the MF for different image sizes. The results are plotted in the figures 7.3 and 7.4. From the figures, we see that both samples reach stable values for the volume density, the surface density, the integral mean curvature, and the Euler number with increasing image size.

In other words, we can use the MF in order to define a so-called geometric REV. For both media, the characteristics of the MF versus image size is in excellent agreement with the development of the hydraulic conductivity (see 6.9 and 6.10). This result can be interpreted as follows: if the sample size is representative with respect to the MF it is automatically representative with respect to physical parameters which depend on exclusively on the geometry of the pore geometry.

In other words, for the kind of structure which is represented by the sintered glass, the MF can be used as proxy in order to determine the REV of a macroscopic property e. g. the hydraulic conductivity. At least for the investigated structure, figure 7.1 has to modified such as the black and gray areas are of the same size.

---

[1] Unfortunately, this is not always the case and in the next chapter we will present some counter-examples.

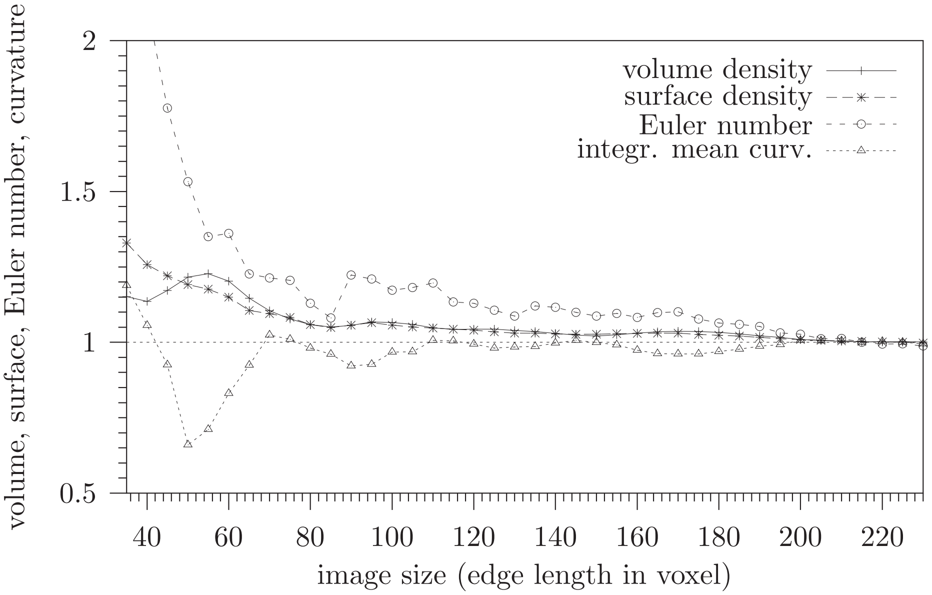

Figure 7.3: Minkowski functionals for medium P250 with increasing image size. The MF were normalized since we are only interested in their variations versus the sampled volume.

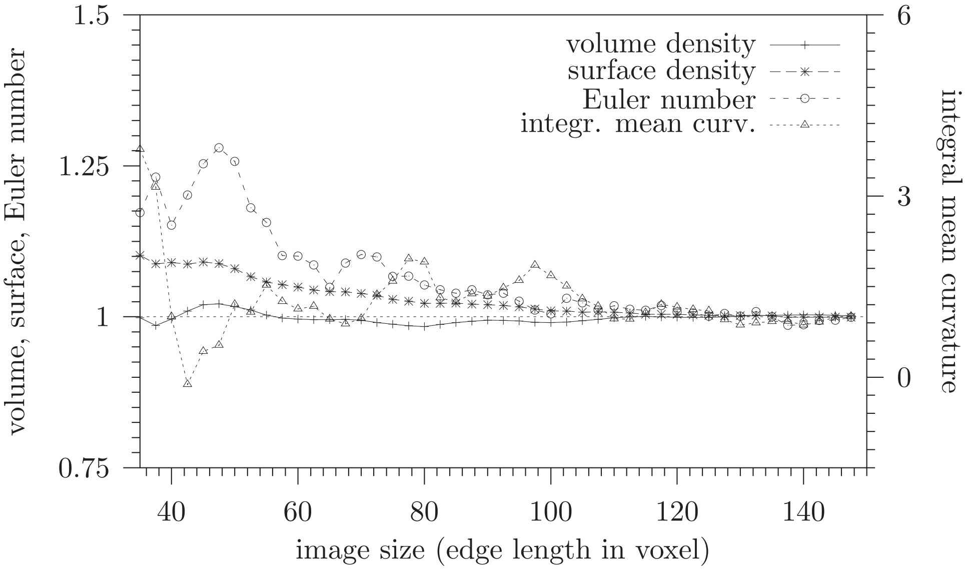

Figure 7.4: Minkowski functionals for medium P100 with increasing image size. As in figure 7.3, the values are normalized. Here, the integral mean curvature shows a significantly larger variation and is therefore plotted on the right hand axis.

7.2.3 Variations of the integral mean curvature

The larger variations of the integral mean curvature of medium P100 need a separate discussion. Our explanation for that phenomena is a surface roughness in the investigated images. This might be a material property or an artefact of the tomography. How a surface roughness influences the integral mean curvature can be explained as follows.

Let us assume we have a given image with the MF V_0, V_1, V_2, and V_3 where the total image volume is 1 and the resolution is given by r ($r < 1$). We now switch a voxel just above a flat surface from pore to solid phase and calculate the impact to the four MF. Obviously, the volume density changes by $\Delta V_0 = r^3$ and the surface density by $\Delta V_1 = 5r^2$. The integral mean curvature changes by $\Delta V_2 = 3\pi r$ and the Euler number stays constant.[2] Therefore, the integral mean curvature is the most sensitive of the MF to changes in the voxel configuration on the surface of the object, i. e. the solid space. The behavior of the integral mean curvature in figure 7.4 shows small variations on the surface of the solid space which are no homogeneously distributed.

7.2.4 Residual water content

An evidence that the observed variation of the integral mean curvature reflects a rough surface and not only an artefact could be the residual water content. As one can see from table 6.2 and also from figures 6.18 and 6.19, the two samples deviate with respect to the residual water content. Interestingly, the medium P250 has a residual water content of almost 20 % while the same value for P100 is only about 11 % at comparable pressure conditions. A surface roughness would be responsible for the hydraulic continuity even at very low saturations. This has been shown by Dullien et al. (1989) for etched glass bead packs.

The medium P250 has a more or less plane surface and parts of the pore space might lose the hydraulic contact easier which would explain the higher residual water content.

7.3 Conclusion

In this chapter, we have successfully applied the MF in order to characterize a complicated structure. For binary images, the MF can be determined in a very efficient way and give reasonable results even for small image sizes which is a main advantage over statistical methods like the two-point correlation function. Additionally, we found that the MF might serve as a proxy in order to determine the size of a REV.

---

[2] For convenience, we calculated the exact values for cubes on a cubic lattice. But this has no influence on our argumentation (see section 2.3).

To be more precise: for the investigated structure the size of the geometric REV is in the same range as the REV for a physical parameters that are strongly related to the underlying geometry like the hydraulic conductivity or the pressure-saturation relation.
On the basis of these promising results, we will use the MF as the basis for the reconstruction of complicated structured media in the next chapter.

8 Reconstruction of the porous media

In this chapter, we present different methods for the reconstruction of porous media. All methods have in common that they are based on a description of the complicated structure by a manageable amount of data.
This chapter is structured as follows. The amount of information that is used for the reconstruction increases successively: beginning with a reconstruction based on the MF (which are only 4 numbers) up to the one that uses a density distribution function.

8.1 Reconstruction based on Minkowski functionals

In the previous chapter, we have shown that we could characterize the investigated structure in a very efficient way using the MF. As one result, we could determine a minimum size of the sample so that the MF are independent of the image size. The minimum size, which can be regarded as a REV with respect to the geometry of the pore structure, was about the same as the REV for the hydraulic conductivity and the pressure-saturation relation.
As a consequence of the Hadwiger theorem, all physical properties, which satisfy the same axioms as the MF (additivity, motion invariance, etc., see chapter 2) can be expressed as a linear combination of the MF.
Now we want to ask the question, if a relationship exists between the MF and other physical quantities which do not satisfy (all) the axioms mentioned above.[1] This would lead to a dramatic reduction in information that is needed to describe the complicated structure since there are only $d+1$ MF for d-dimensional objects.

8.1.1 Dimensionality of the MF compared to a binary structure

For a digitized image consisting of 2^n voxel, we can write this hypothesis in the form

$$k(2^n) \rightarrow k(V_0, V_1, V_2, V_3) \tag{8.1}$$

In other words, the property k, e. g. the hydraulic conductivity, which in general depend on 2^n different voxel configuration might depend only on the MF of the structure.

---

[1] One example is the hydraulic conductivity which is e.ġ. not additive in the sense of the MF.

8.1.2 Reconstruction results

Figure 8.1 shows four different structures in 2D which have exactly the same MF. For the discussion it is sufficient to work in 2 dimensions since the arguments in 3D are identical. Structure a in figure 8.1 is a 2D slice through the pore geometry of the medium P100. The lattice size is 300 x 300 pixel as the image size was scaled to 1 mm^2 the resolution of 1/300 mm. All four images have a porosity of .437 and a boundary length density of 30.28 mm^{-1}. The Euler number is $\chi_4 = 16\,\mathrm{mm}^{-2}$ ($\chi_8 = 11\,\mathrm{mm}^{-2}$). In order to minimize effects of the boundaries, periodic boundary conditions were used.

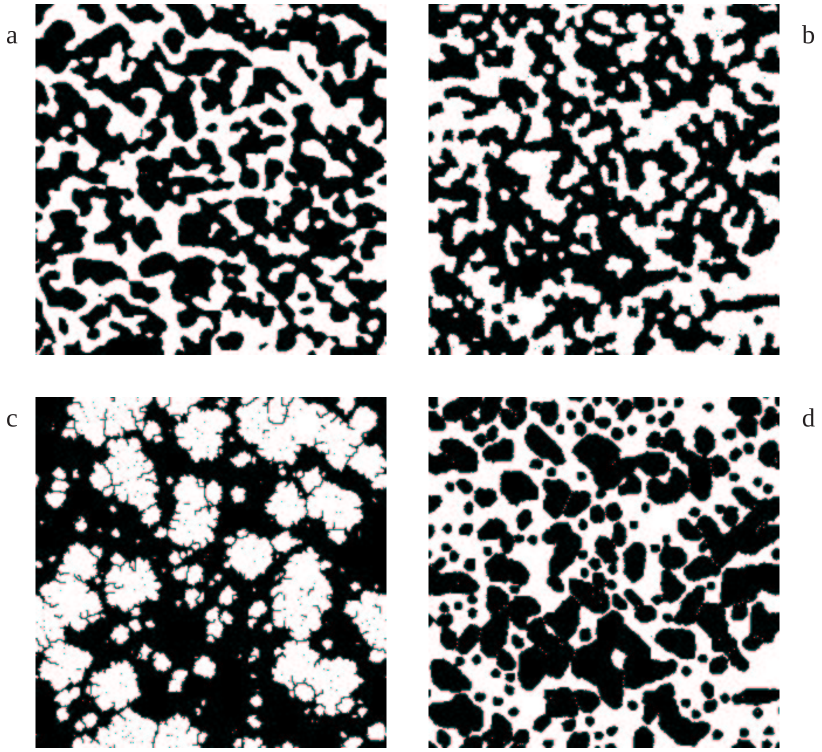

Figure 8.1: Four different structures in 2D (300^3 pixel) which have exactly the same Minkowski functionals. Periodic boundaries where used for the calculation of the MF.

The reason why the four images appear to be so different although they posses the same MF is that the MF are only integrated values over the entire structure. In 2 dimensions, the Euler number χ is given by the number of isolated objects minus the number of redundant connections. Therefore, there is a freedom in the number of isolated objects which will be then compensated by more or less connections. For example, the structure c in figure 8.1, consists of many isolated objects but contains also a lot of redundant connections which are realized by single pixel within the larger objects. Additionally, the single isolated pixel are needed to obtain the same boundary length.

Even without performing any simulation, we can see from figure 8.1 that structures which agree in their MF need not have similar physical properties like the hydraulic conductivity. For example, only two of the four structures (a and d) have continuous flow paths within the white phase that connect opposite sides.

This result is very similar to investigations about the reconstruction of porous media by using the two-point correlation function. Roberts (1997) found that "materials with practically identical two-point correlation functions can have very different morphology and macroscopic properties" (p. 3211).

8.2 Boolean model of spheres

As we have seen in the previous section, the MF do not contain enough information about a given structure. Thus a reconstruction algorithm based on the MF need not lead to “comparable” structures. Therefore, a larger amount of information about the structure is needed in the reconstruction process.

A possible extension in this context are Boolean models which are based on a homogenous Poisson process which generates completely random distributions of points in space (Stoyan 2000). Mathematically spoken, the Poisson distributed is defined as

$$P(\Phi(A) = i) = \frac{\rho^i e^{-\rho}}{i!}, \quad i = 0, 1, \ldots \tag{8.2}$$

where $P(\Phi(A) = i)$ is the probability to find i points within the volume A and ρ is the intensity, i. e. the mean number of points per volume unit.

In the next step of the Boolean model, each point is taken as the seed point of a sphere with a given radius. In the simplest form, all spheres have the same radius as shown in figure 8.2. A major advantage of the Boolean model is that in many cases the mean MF can be given analytically (Mecke and Wagner 1991). The mean MF for a realization of a Boolean model depend on the MF of the generating objects and the point density of the Poisson process. An example where the generating objects are spheres with a diameter of $D = 9$ lattice nodes is shown in figure 8.3.

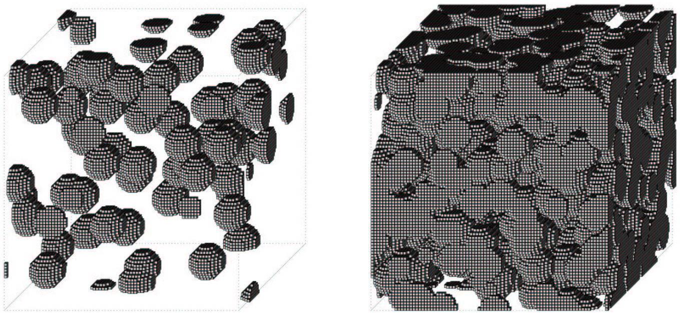

Figure 8.2: Two realizations of a Boolean model with spheres of constant radius. With increasing point density, the spheres will more and more overlap.

8.2.1 Reconstruction of P100 with a Boolean model

With regard to the fabrication of the sintered glass media, we used a Boolean model of spheres for its reconstruction. Instead of the simple Boolean model, where the solid space consist of overlapping spheres with the same diameter, we used spheres of different size. Therefore we determined the grain size distribution in the scanned image by the method of morphological granulometry as shown in figure 8.4. This was

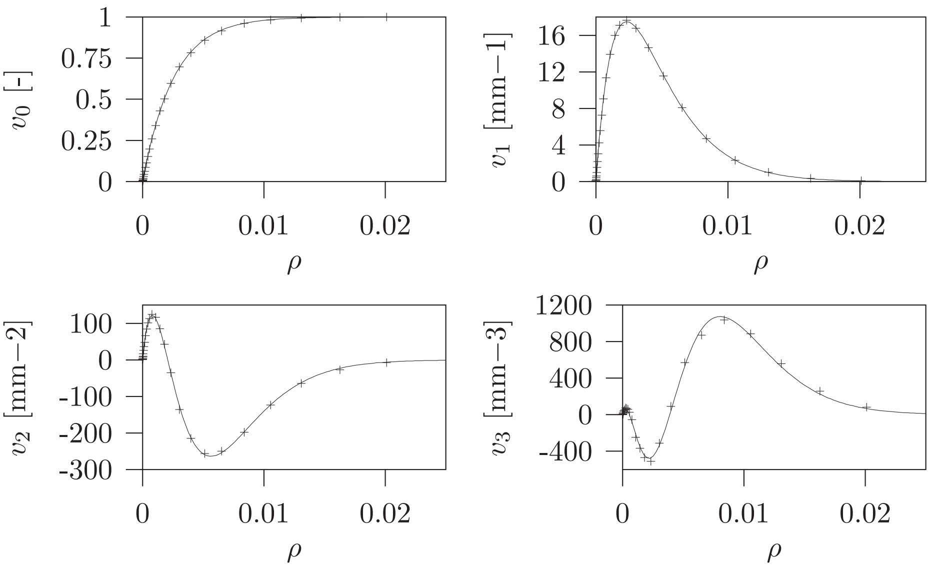

Figure 8.3: Mean MF for realizations of the Boolean model. The image size was 80^3 voxel and the lattice spacing 0.015 mm (isotropic).

done after a Shepard interpolation which increased the image resolution by a factor 2. The cumulative grain size distribution can now be interpreted as the probability that a sphere in the Boolean model has a radius r. This leads to a solid space as shown in figure 8.5 (right image). For the point density a value was chosen which yields the same porosity for both the original and the reconstructed image.

8.2.2 Hydraulic conductivity of the Boolean reconstruction

We used the Boolean model in order to generate 16 different realizations and calculated their MF together with the hydraulic conductivity. The results are shown in table 8.1. The agreement between the hydraulic conductivity from the original image and the Boolean realizations is excellent. This agreement might be at first surprising, since the void space of the compared structures looks very different (fig-

	Φ [-]	Surface [mm^{-1}]	Curvature [mm^{-2}]	χ_6 [mm^{-3}]	χ_{26} [mm^{-3}]	K 10^{-2} cm/s
P100	0.476	18.99	8.23	-687	-668	8.0±1.0
Boolean	0.476	18.84 – 19.78	-63.08 – -75.45	-505 – -673	-432 – -547	7.8 – 11.2

Table 8.1: MF and hydraulic conductivity of the original image (P100) and the Boolean reconstruction. The interval gives the maximum and minimum values that have been found from 16 different realizations.

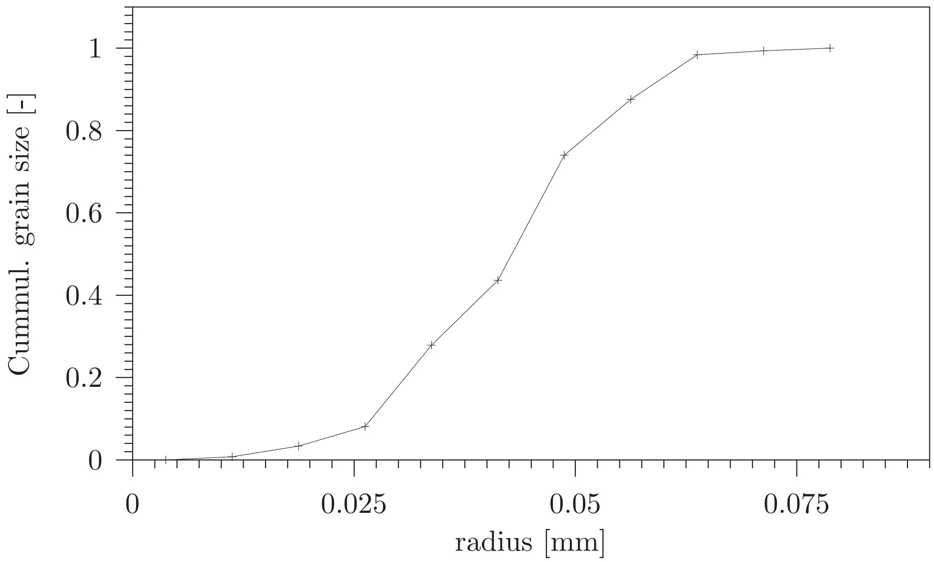

Figure 8.4: Cumulative grain size distribution of P100 as determined by the morphological granulometry.

ure 8.5). But the geometry of the pore space is more similar and velocities in the flow simulations are comparable. As we can see from table 8.1, there is very good agreement concerning the surface density and a rather good agreement for the Euler number. The original structure and the Boolean realizations are highly connected (large negative Euler number) with similar pore dimensions.

Obviously the reconstructed images have more curved surfaces (the concave curvature of the void phase is counted negatively) than the original image. But from the agreement in the hydraulic conductivity we conclude that the impact of the curvature on that parameter is rather small.

8.2.3 P^c-S^w curve of the Boolean reconstruction

We also investigated the pressure-saturation curve of the structures originating from the Boolean model as shown in figure 8.6. From complete saturation down to a saturation of 0.5 both curves are almost identical. This is not surprising since the investigations on the hydraulic conductivity indicated a similar pore spectrum and a similar pore connectivity. But at lower water contents both curves differ significantly. This difference is caused by the higher curvature in the Boolean reconstruction. In other words, the water has a higher tendency to form pendular rings and its drainage affords a higher pressure (Hilpert and Miller 2001).

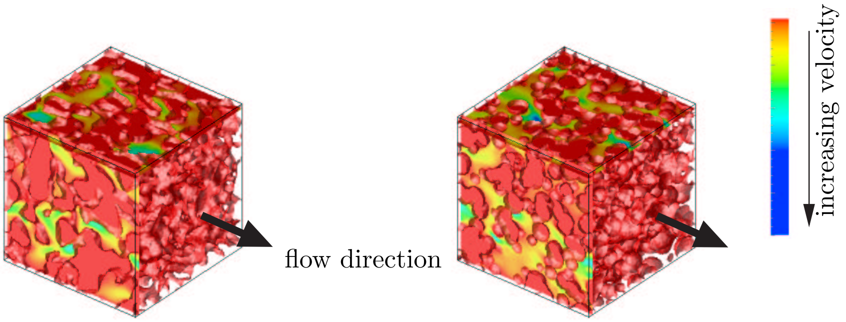

Figure 8.5: 3D visualizations of the original pore geometry (P100, on the left) and the reconstruction with a Boolean model. Beside the structure, the figure shows the absolute value of the velocity field in two cross sections.

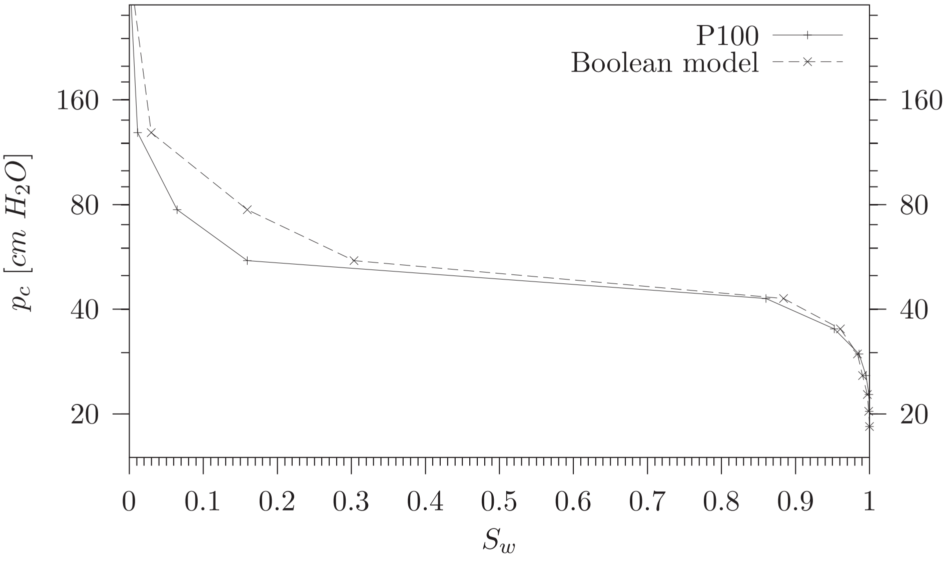

Figure 8.6: Pressure-saturation curve for the medium P100 (120^3 voxel) and its Boolean reconstruction.

8.2.4 Extensions of the Boolean model

In the application of the Boolean model, we limited the input parameters to the porosity and the grain size distribution. These parameters can be determined very efficient with the tools presented in this work. The reduction from a complete description of a complicated structure to a grain size distribution is enormous. But we have to keep in mind that the reconstruction with the Boolean model was based on the assumption that the solid space of the given structure can be mimicked by overlapping spheres. In the case of the sintered glass medium, this assumption worked quite well. For other porous media, like soil, it might be a too strong restriction. Arns (2002) applied the Boolean model in order to reconstruct the pore space of a Fontainebleau sandstone. In that study it was necessary to work with a mix of different spheroidal grains to get a good match between all MF of the measured image and the Boolean ensemble. That approach led towards complicated reconstruction models where information about the formation of the pore geometry was involved. Depending on the investigated structure, this might be an interesting extension of Boolean models. But this lies not within the concept of our image reconstruction. As pointed out before, we want to limit the reconstruction algorithm to (few) geometric "measurements" only.

In our Boolean model we used the grain size distribution as input parameter. The grain size distribution was determined by measuring the volume density (i. e. the first order MF) on successively openings of the image. Therefore, it is straightforward to use the information of the opened images in the reconstruction process. For practical reasons, we worked with the eroded and dilated images instead of the opened images. Additionally, we force the reconstructed structure to have the same Minkowski functions (Mfs) as the original image.

8.3 Reconstruction on the basis of the Minkowski functions

As described in chapter 2, the Mfs are given by the Minkowski functionals for the parallel bodies of a given structure. In the following, we want to generate structures with identical Mfs. This can be done with the help of a simulated annealing algorithm.

8.3.1 Simulated annealing

Simulated annealing (SA) is a long known Monte Carlo concept in order to solve optimization problems while it reached a broad circulation only after a publication by Kirkpatrick et al. (1983). The term simulated annealing derives from the roughly analogous physical process of heating and then slowly cooling a substance to obtain a strong crystalline structure. In the simulation, a minimum of the objective function corresponds to this ground state of the substance. During the simulation the state of the system is changed randomly in small steps. The changes are accepted if the deviation to the objective function f is reduced but also in some cases where f is increased. Those cases have the probability of

$$p = e^{-\frac{\delta f}{T}} \tag{8.3}$$

where δf is the increase in f and T the so-called system temperature.
The choice of T is not trivial, since it must be avoided that the system is trapped in a local minimum.

8.3.2 Objective function

In our simulation, the objective function is the sum over the deviations to the Mfs

$$f = \sum_{\nu,\epsilon} \alpha_\nu |M_\nu(\epsilon) - M'_\nu(\epsilon)| \tag{8.4}$$

where ϵ gives the number of erosion or dilation steps that are investigated.
The value α_ν can be seen as a weighting for the contribution of the νth Mfs to the objective function.
In the case of ϵ=0, the objective function is the deviation sum over only to the sum of deviations to the MF of the original image, i. e. the results discussed in section 8.1.2. The differences in the three structures shown in figure 8.1 (b – d) were mainly caused by different weightings α. Initially, the image consisted only of pore phase ($\phi = 1.0$). Then white (and later also black) pixel were set randomly. A large weighting α of the Euler number led to the situation that isolated white holes were created till the wanted Euler number was reached. Then, these holes served as the seed point of larger objects so that the overall structure had the required length density and porosity (see figure 8.1, c).

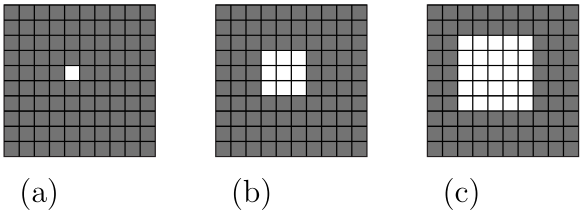

Figure 8.7: *On an entirely "black" image, a single voxel is switched into "white" phase. This has an impact on the the eroded images (b) and (c). Image (b) and (c) are erosions of the black phase with a squares of 3 and 5 lattice nodes edge length.*

As we found out by the simulation, different values of α_ν produce extremely different structures, which all yield the same MF.

8.3.3 Simulation results

The generation of structures which match in all Mfs is very time consuming. This is due to the fact the calculation of the objective function is costly. As illustrated in figure 8.7, the switch of a voxel from one phase to the other leads to a change in the eroded (and dilated) images. Subsequently, the MF are calculated for all eroded and dilated images. Because of the additivity of the MF, it is not necessary to perform the calculation for the entire image but only for a segment of the image around the changed voxel. For several erosion/dilation steps, this still affords large computing time. Therefore, we limited our reconstruction to 2D and small images with periodic boundary conditions.

Similar to the reconstruction results based on the MF, we can see again that obviously different structures possess the same Mfs. As we can see from figure 8.8, the reconstructed image has completely different length scales, since it consists of one large element and a number of small spots.

From the "failed" reconstruction based on the Mfs we conclude that they are not sufficient in order to create (visually) comparable structures. The problem is similar to the discussion of the reconstruction based on the MF. Like the MF, the Mfs are only integrated parameters over the entire structure.

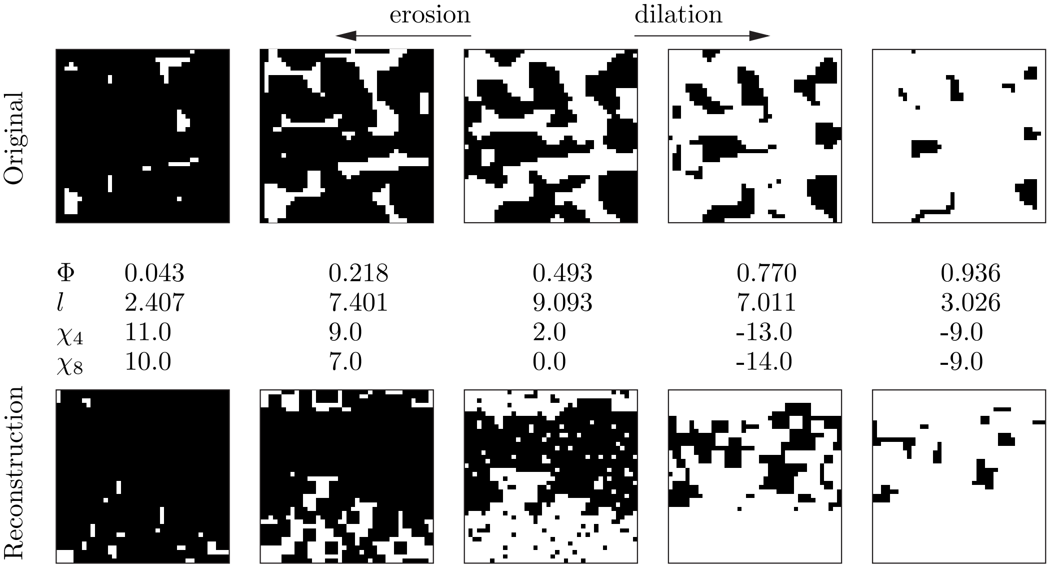

Original:

Φ	0.043	0.218	0.493	0.770	0.936
l	2.407	7.401	9.093	7.011	3.026
χ_4	11.0	9.0	2.0	-13.0	-9.0
χ_8	10.0	7.0	0.0	-14.0	-9.0

Reconstruction:

Φ	0.033	0.191	0.486	0.781	0.942
l	2.278	7.401	9.158	7.011	3.009
χ_4	13.0	8.0	2.0	-7.0	-8.0
χ_8	13.0	4.0	-3.0	-10.0	-8.0

Figure 8.8: Original image and reconstruction based on the Mfs (porosity, boundary length, and Euler number over 2 erosion/dilation steps with squares). The images have a size of 40^2 pixel and a resolution of 1/40=0.025 mm. Therefore, the boundary l is given in 1/mm and the Euler number as 1/mm^2.

8.4 MF and interception length

As a consequence of the previous results it seemed necessary to included statistical parameters in the reconstruction algorithm. From the different statistical parameters, we chose the interception length density function (ILDF) as presented in chapter 3. The choice was based on two reasons. First, the ILDF is of general importance for the fluid flow through a given structure. Secondly, Torquato (2002) and Roberts and Torquato (1999) already successfully included the ILDF in reconstructions based on Gaussian random fields.

The calculation of the ILDF in the simulated annealing model is very efficient. In the beginning, we determine the ILDF once over the entire image. During the optimization process, a swap of a single voxel changes the interception length only locally along three lines parallel to the main axes as illustrated in figure 8.9.

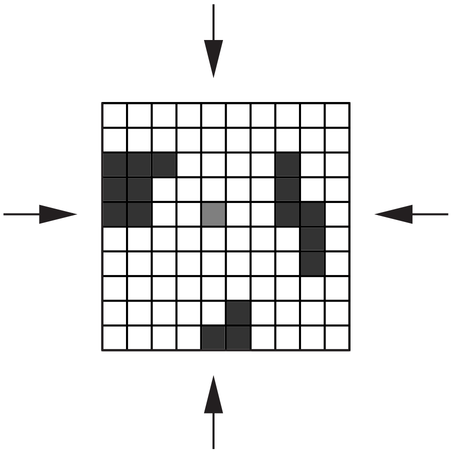

Figure 8.9: Illustration of the impact of a single pixel flip to the interception length in 2D. Since we are only interested in the interception length of lines parallel to the main axis, the swapped pixel in the middle of the image (in gray), changes the interception length from 5 pixel to two times 2 pixel in the horizontal line. This can be calculated in a very efficient way.

The objective function is now given by

$$f = \sum_{\nu} \alpha_{\nu} |V_{\nu} - V'_{\nu}| + \beta \sum_{l} |I_l - I'_l| \tag{8.5}$$

where the V_ν are the MF and I_l is the number of interception with length l. Again, with the weightings α_ν and β we determine the impact of the different parameters on the objective function.

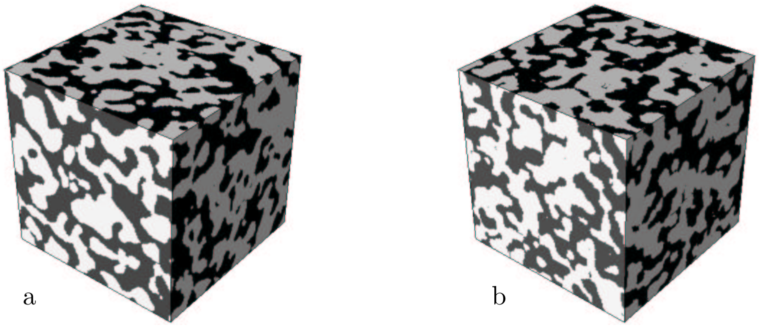

Figure 8.10: Original image (P100, a) and one example of its reconstruction (b) where both images have the same MF and approximately the same ILDF. The image size is 150^3 voxel with a resolution of $7.5\,\mu$m.

8.4.1 Simulation results

The reconstruction based on the MF together with the ILDF gave visually good results compared to the original structure. As shown in figure 8.10, it is hard to distinguish between the original and the reconstructed image. Nevertheless, the ILDF shows some deviation (figure 8.11) while the MF of both structures are identical. This is due to the fact that the weighting of the MF was higher than for the ILDF ($\alpha_\nu > \beta, \forall \nu$ in equation 8.5). Thus, the simulated annealing first optimized the MF and secondly the IDLF.

Figure 8.11: ILDF for the original image and one example of its reconstruction.

8.4.1.1 Hydraulic conductivity

In order to get some information about the statistical variances, we generated 24 different structures and calculated the hydraulic conductivity. We found an excellent match between the original image and its reconstruction (table 8.2).

	K [10^{-2} cm/s]
P100	10.6±0.5
Reconstruction	9.2 – 12.6

Table 8.2: Hydraulic conductivity of the original image (P100, 80^3 voxel) and the reconstructions. The interval gives the maximum and minimum values from 24 different realizations.

8.4.1.2 Pressure-saturation relation

For one realization, we derived the pressure-saturation curve and compared it the original image (figure 8.12). In contrast to the Boolean model, we found a very good agreement between the two curves over the entire saturation range. Small deviations occur close to saturation which are likely caused by boundary effects.

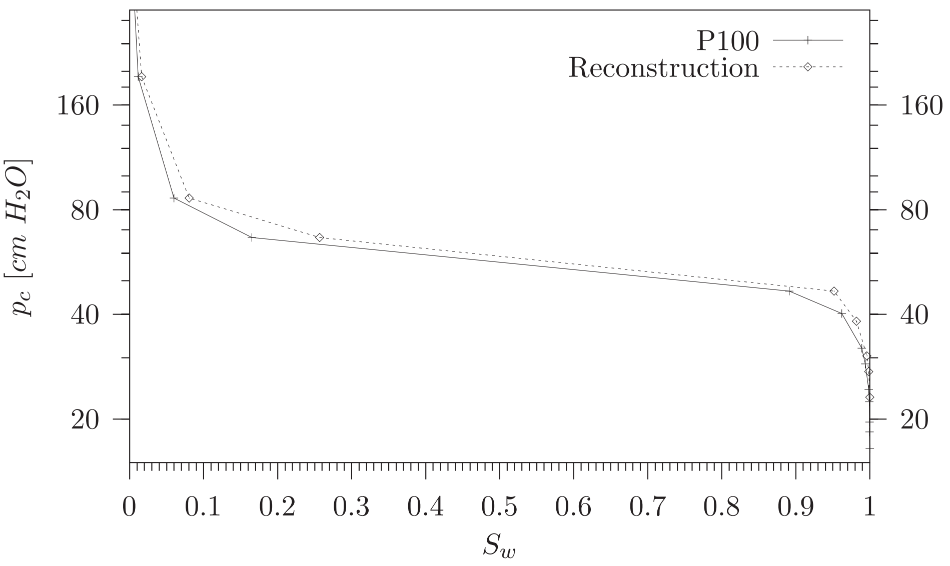

Figure 8.12: Pressure-saturation relations of the original image and one example of its reconstruction.

9 Summary and outlook

9.1 Structure analysis and hydraulic functions

In the framework of this thesis, we investigated two different samples of a sintered boron silicate glass. Based on x-ray tomography, we applied methods from morphological image analysis in order to derive geometric informations about the structure such as the pore size distribution function. Here, we found a good agreement with values given by the manufacturer and the resolution proved to be high enough in order to derive a reliable pore geometry.

For the complicated structure, the Navier-Stokes equation[1] was solved using a LB method. From the flow field, the diagonal terms of the hydraulic conductivity tensor were calculated with increasing image size. The results showed that the dependency on the flow direction decreased with increasing image size and it was concluded that the average hydraulic conductivity could be described by a scalar value k. The determined values of k were compared to falling head measurements and for both samples, the measured values were overestimated. A larger number of different structures would be needed in order to decide if either the flow simulations or the measurements have a bias.

Subsequently, we made a similar analysis for the capillary pressure-saturation relation of the two investigated media. This was done using a pore-morphology-based model where the desaturation of the medium is simulated by calculating discrete quasi-static distributions. In the model, it is assumed that the interface between the water and the air phase is spherical which leads to an overestimation of the required pressure. The computing times for the PMB model are moderate, especially when using the modified digital spheres which has been done in this thesis for the first time. The fast computation was necessary in order to study the dependency of the pressure-saturation relation with increasing image size. As for the hydraulic conductivity, we could define a REV with respect to the pressure-saturation relation for both media. But the comparison to the measured data showed significant deviations which could not be explained by a bias of the PMB model. These deviations could not be explained conclusively. It is most likely that there are different aspects involved. Beside the experimental difficulties, the contact angle might have an influence as well as larger variations of the pore geometry.

---

[1] In the Stokes limit.

Using the Minkowski functionals for the characterization of the complicated structure, we found that the size of the geometric REV corresponds to the size of the REV for the hydraulic conductivity and also to the size of the REV for the pressure-saturation relation.

9.2 Reconstruction algorithms

In chapter 8, we applied four different approaches in order to reconstruct the pore space of the investigated structures. The task of the reconstruction was to come up with a structure that is similar with respect to the hydraulic conductivity and the capillary pressure-saturation relation.

In that sense, the reconstruction algorithm based on the MF and on the Mfs were unsuccessful. In retrospect, the result is not surprising for the MF since they are only integrated values over the entire geometry. More astonishing was the failure of the Mfs which can be explained by the fact that they contain less information as one might think intuitively.

Good results were found using a Boolean model with spheres of different diameter. Here, the agreement in the hydraulic conductivity was very good and the pressure-saturation curve deviated only at low saturations. These deviations were caused by the higher curvature of the overlapping spheres compared to the investigated structure.

Finally, a simulated annealing algorithm based on the MF and the ILDF generated structures which were similar compared to the original structure. Beside the excellent agreement in the hydraulic conductivity, the $P^c - S^w$ curves also showed a good agreement. These results are very promising since the reconstruction included only four numbers (the MF) together with one distribution function. Since the upper limit of the interception length is given by the edge length l (assuming that the image has the dimension l^3), we could write k as a function of $l + 4$ parameters only:

$$k \equiv k(V_0, V_1, V_2, V_3, P_1, P_2, P_3, \ldots, P_l) \tag{9.1}$$

where V_n is the nth Minkowski functional and P_i is the probability of finding a chord with length i voxel. Surely, our results are no proof that such a reduction of dimensionality is always possible, even if the investigated structure is isotropic.

Nevertheless, the combination of integrated values with statistical parameters is a new approach which might lead to a compact description of random heterogenous media.

9.3 Outlook

Over the last years, several studies showed that the hydraulic conductivity of a complicated structure can be derived by flow simulations, e. g. by LB methods. In the context of other studies, the deviations between the measured and the simulated conductivity which were found in this study do not reflect a fundamental problem. This is in contrast to the two-phase flow processes. Simulations of large sample sizes are limited to simplified models such as the pore-morphology-based model which has been used in this work. While this problem might be solved over the years by larger and faster computers, we believe that fundamental difficulties still remain. Up to now, and also in the context of this work, it is assumed that the two-phase flow depends only on the pore geometry. Therefore, the surface properties were not taken into account. In principal, the surface properties can be measured, e. g. by scanning electron microscopy, but it is not clear how to include the information into simulations. This is an upscaling problem since the typical size of the pores lies in the μm range while variations of the surface are linked to the nanoscale. In our understanding, it is a must to also include measurements of the surface properties of the material in further studies.

Obviously, the Minkowski functionals will be as useful in the characterization of complicated surfaces as they are in the description of complicated structures.

The reconstruction algorithms which had been developed in this work, can be seen as a very promising basis of further studies. One question could be, if the reconstructed images are similar also with respect to other physical properties? As an example, we calculated the flow field of the inverse structure, i. e. the fluid flows through the solid phase only. In the case of the reconstruction based on the MF and the ILDF, the agreement was not as good as for the hydraulic conductivity but still comparable. Therefore, it can be assumed that the original and the reconstructed images are similar also concerning the heat transport since this parameter depends on “flow” processes in both the solid matrix and the pore space. A better agreement could be achieved if one includes not only the interception length of the pores but also the interception length of the solid phase into the reconstruction algorithm.

Finally, another extension of the proposed reconstruction method is its application to anisotropic structures. In that case, the interception length density function has to be calculated separately for each direction. It is straightforward to include this calculation into the objective function of the simulated annealing algorithm.

Bibliography

Arns, C. H., 2002. The influence of morphology on physical properties of reservoir rocks. Ph.D. Diss. The Universiy of New South Wales.

Batchelor, G. K., 1999. An introduction to fluid dyamics. 2nd edn. Cambrige University Press, Cambrige.

Bear, J., 1972. Dynamics of Fluids in Porous Media. Dover Publications, New York.

Bernsdorf, J., Brenner, G. and Durst, F., 2000. Numerical analysis of the pressure drop in porous media flow with lattice boltzmann (bgk) automata. Computer Physics Communications, 129: 247–255.

Buick, J. M., 1997. Lattice Boltzmann Methods in Interfacial Wave Modelling. Ph.D. Diss. The University of Edinburgh.

Cushman, J. H., 1990. An introduction to hierarchical porous media. In: J. H. Cushman (Editor), Dynamics of Fluids in Hierarchical Porous Media. Academic Press, London, pp. 1–6.

Dullien, F., Zarcone, C., MacDonald, I., Collins, A. and Bochard, R., 1989. The effect of surface roughness on the capillary pressure curves and the heights of capillary rise in glass bead packs. J. Colloid. Interface Sci., 127: 363–372.

Frisch, U., Hassacher, B. and Pomeau, Y., 1986. Lattice-gas automata for navier-stokes equations. Phys. Rev. Lett., 56: 1505–1508.

Gagvani, N. and Silver, D., 1999. Parameter-controlled volume thinning. Graphical Models and Image Processing, 61: 149–164.

Graf, H., Vogel, H. and Roth, K., n.d. Averaging of hydraulic properties. in prep.

Hadwiger, H., 1957. Vorlesungen über Inhalt, Oberfläche und Isoperimetrie. Springer-Verlag, Berlin Heidelberg.

Hazlett, R. D., 1995. Simulation of capillary-dominated displacements in microtomographic images of reservoir rocks. Transp. Porous Media, 20: 21–35.

Hilpert, M. and Miller, C. T., 2001. Pore-morphology-based simulation of drainage in totally wetting porous media. Adv. Water Resour., 24: 243–255.

Hug, D. and Schneider, R., 2002. Kinematic and crofton formulae of integral geometry: recent variants and extensions. In: C. B. i Vidal (Editor), Homenatge al professor Lluís Santaló i Sors. Universitat de Girona, Girona, pp. 51–80.

Kirkpatrick, S., Gelatt, C. D. and Vecchi, M. P., 1983. Optimization by simulated annealing. Science, 220: 671–680.

Klute, A. and Dirksen, C., 1986. Hydraulic conductivity and diffusivity: Laboratory methods. In: A. Klute (Editor), Methods of soil analysis. Part 1. Physical and Mineralogical Methods. 2nd edn. American Society of Agronomy, Madison, Wisconsin, pp. 687–734.

Maier, R. S., Bernard, R. S. and Grunau, D. W., 1996. Boundary conditions for the lattice boltzmann method. Phys. Fluids, 8: 1788–1801.

Manwart, C., Aaltosalmi, U., Koponen, A., Hilfer, R. and Timonen, J., 2002. Lattice-boltzmann and finite-difference simulations for the permeability for three-dimensional porous media. Phys. Rev. E, 66: 16702–1–16702–11.

Mecke, K. and Wagner, H., 1991. Euler characteristic and related measures for random geometric sets. Journal of Statistical Physics, 64: 843–850.

Mecke, K. R., 2000. Additivity, convexity, and beyond: Application of minkowki functionals in statistical physics. In: K. R. Mecke and D. Stoyan (Editors), Statistical Physics and Spatial Statistics. Springer-Verlag, Berlin Heidelberg, pp. 111–184.

Mei, R., Shyy, W., Yu, D. and Luo, L.-S., 2000. Lattice boltzmann method for 3-d flows with curved boundary. Journal of Computational Physics, 161: 680–699.

Mualem, Y., 1976. A new model for predicting the hydraulic conductivity of unsaturated porous media. Water Resour. Res., 12: 593–622.

Nagel, W., Ohser, J. and Pischang, K., 2000. An integral-geometric approach for the euler-poincaré charactaristic of spatial images. Journal of Microscopy, 198: 54–62.

Ohser, J. and Mücklich, F., 2000. Statistical analysis of microstructures in materials science. John Wiley & Sons, Ltd, Chichester, England.

Pan, C., Hilpert, M. and Miller, C., 2001. Pore-scale modeling and saturated permeabilities in random sphere packings. Phys. Rev. E, 64: 066702–1–066702–9.

Pang, A. and Furman, J., 1994. Data quality issures in visualization. SPIE proceedings on Visual Data Exploration and Analysis, 2178: 12–23.

Richards, L. A., 1931. Capillary conduction of liquids through porous mediums. Physics (NY), 1: 318–333.

Roberts, A. and Torquato, S., 1999. Chord-distribution fuctions of threee-dimensional random media: Approximate first-passage times of gaussian processes. Phys. Rev. E, 59: 4953–4963.

Roberts, A. P., 1997. Statistical reconstruction of three-dimensional porous media from two-dimensional images. Phys. Rev. E, 56: 3203–3212.

Roth, K., Vogel, H.-J. and Kasteel, R., 1999. The scaleway: a conceptual framework for upscaling soil properties. In: J. Feyen and K. Wiyo (Editors), Modelling of Transport Processe in Soils. Wageningen Pers, Wageningen, NL, pp. 477–490.

Soille, P., 1999. Morphological image analysis: principles and applications. Springer-Verlag, Berlin Heidelberg.

Stoyan, D., 2000. Basic ideas of spatial statistics. In: K. R. Mecke and D. Stoyan (Editors), Statistical Physics and Spatial Statistics. Springer-Verlag, Berlin Heidelberg, pp. 3–21.

Stoyan, D., 2002. Simulation and characterization of random system of hard particles. Image Anal Stereol, 21: 41–48.

Tölke, J., 2001. Gitter-Boltzmann-Verfahren zur Simulation von Zweiphasenströmungen. Ph.D. Diss. Technische Universität München.

Torquato, S., 2002. Random heterogeneous materials: microstructure and macroscopic properties. Springer-Verlag, New York.

van Genuchten, M. T., 1980. A closed-form equation for predicting the hydraulic conductivity of unsaturated soils. Soil Sci. Soc. Am. J., 44: 892–898.

Vogel, H. J., 1997. Digital unbiased estimation of the euler-poincaré characteristic in different dimensions. Acta stereologica, 16: 97–104.

Vogel, H. J. and Kretzschmar, A., 1996. Topological characterization of pore space in soil – sample preparation and digital image-processing. Geoderma, 73: 23–38.

Vogel, H.-J. and Roth, K., 2003. Moving through scales of flow and transport in soil. J. Hydrol. (Amsterdam), 272: 95–106.

Vogel, H. J., Cousin, I. and Roth, K., 2002. Quantification of pore structure and gas diffusion as a function of scale. Eur. J. Soil Sci., 53: 465–473.

Weibel, E. R., 1980. Stereological methods. Vol. 2; Theoretical foundations. Academic Press Inc., London.

Wolf-Gladrow, D. A., 2000. Lattice gas cellular automata and lattice Boltzmann models: an introduction. Lecture notes in mathematics, 1725, Springer-Verlag, Berlin.

Zou, Q. and He, X., 1997. On pressure and velocity boundary conditions for the lattice Boltzmann BGK model. Phys. Fluids, 9: 1591–1598.